

PL-TR-94-2266

# **A MODEL OF THE DIURNAL VARIATION IN MAGNESIUM ION DENSITY AND RADIANCE IN THE THERMOSPHERE**

W. J. McNeil

Radex, Inc.  
Three Preston Court  
Bedford, MA 01730

October 6, 1994

Scientific Report No. 6

Approved for public release; distribution unlimited

**DTIC**  
**ELECTE**  
**JAN 18 1995**  
**S G D**

19950117 049

DTIC QUALITY INSPECTED 'A'



**PHILLIPS LABORATORY**  
**Directorate of Geophysics**  
**AIR FORCE MATERIEL COMMAND**  
**HANSCOM AIR FORCE BASE, MA 01731-3010**

"This technical report has been reviewed and is approved for publication"



EDWARD C. ROBINSON  
Contract Manager  
Data Analysis Division



ROBERT E. MCINERNEY, Director  
Data Analysis Division

This report has been reviewed by the ESD Public Affairs Office (PA) and is releasable to the National Technical Information Service (NTIS).

Qualified requestors may obtain additional copies from the Defense Technical Information Center. All others should apply to the National Technical Information Service.

If your address has changed, or if you wish to be removed from the mailing list, or if the addressee is no longer employed by your organization, please notify PL/IM, 29 Randolph Road, Hanscom AFB, MA 01731-3010. This will assist us in maintaining a current mailing list.

Do not return copies of this report unless contractual obligations or notices on a specific document requires that it be returned.

REPORT DOCUMENTATION PAGE			Form Approved OMB No. 0704-0188	
Public reporting burden for this collection of information is estimated to average 1 hour per response, including the time for reviewing instructions, searching existing data sources, gathering and maintaining the data needed, and completing and reviewing the collection of information. Send comments regarding this burden estimate or any other aspect of this collection of information, including suggestions for reducing this burden, to Washington Headquarters Services, Directorate for Information Operations and Reports, 1215 Jefferson Davis Highway, Suite 1204, Arlington, VA 22202-4302, and to the Office of Management and Budget, Paperwork Reduction Project (0704-0188), Washington, DC 20503.				
1. AGENCY USE ONLY (Leave blank)		2. REPORT DATE 6 October 1994		3. REPORT TYPE AND DATES COVERED Scientific Report No. 6
4. TITLE AND SUBTITLE A Model of the Diurnal Variation in Magnesium Ion Density and Radiance in the Thermosphere			5. FUNDING NUMBERS PE 62101F  PR 7659 TA GY WU AA  Contract F19628-93-C-0023	
6. AUTHOR(S) W. J. McNeil				
7. PERFORMING ORGANIZATION NAME(S) AND ADDRESS(ES) RADEX, Inc. Three Preston Court Bedford, MA 01730			8. PERFORMING ORGANIZATION REPORT NUMBER  RXR-94101	
9. SPONSORING / MONITORING AGENCY NAME(S) AND ADDRESS(ES) Phillips Laboratory 29 Randolph Road Hanscom AFB, MA 01731-3010  Contract Manager: Edward C. Robinson/GPD			10. SPONSORING / MONITORING AGENCY REPORT NUMBER  PL-TR-94-2266	
11. SUPPLEMENTARY NOTES				
12a. DISTRIBUTION / AVAILABILITY STATEMENT Approved for Public Release Distribution Unlimited			12b. DISTRIBUTION CODE	
13. ABSTRACT (Maximum 200 words)  A model has been developed to investigate the behavior of magnesium ions in the thermosphere. The model includes deposition of the atomic metal, diffusion, kinetic creation and destruction of ions, and ultimate removal of the atomic Mg. Transport of the $Mg^+$ by electric fields is also included. A strong diurnal variation in the $Mg^+$ profiles is observed. These profiles are transformed to radiance for conditions mimicking the GLO experiment, to which the results are compared. Key features of the GLO observations are reproduced well by the model.				
14. SUBJECT TERMS Magnesium ions, Atmospheric chemistry, ionospheric magnesium, Magnesium chemistry			15. NUMBER OF PAGES 86	
			16. PRICE CODE	
17. SECURITY CLASSIFICATION OF REPORT Unclassified	18. SECURITY CLASSIFICATION OF THIS PAGE Unclassified	19. SECURITY CLASSIFICATION OF ABSTRACT Unclassified	20. LIMITATION OF ABSTRACT Unlimited	

## TABLE OF CONTENTS

1. INTRODUCTION .....	1
2. THE DEPOSITION RATE .....	2
3. STEADY STATE MODELS .....	6
3.1 THE STEADY STATE PROFILE .....	6
3.2 NEUTRAL CHEMISTRY .....	20
3.3 ION CHEMISTRY .....	28
4. TIME DEPENDENT MODELS .....	40
4.1 THE ONE COMPONENT MODEL .....	40
4.2 THE TWO COMPONENT MODEL .....	45
4.3 ELECTRIC FIELDS .....	56
5. COMPARISON WITH MEASUREMENTS .....	61
5.1 GLO MEASUREMENTS .....	61
5.2 RADIANCE CALCULATIONS .....	61
5.3 MODEL RESULTS .....	65
6. CONCLUSION .....	69
7. REFERENCES .....	74
APPENDIX A. KINETIC MODELS .....	77

Accession For	
NTIS CRA&I	<input checked="" type="checkbox"/>
DTIC TAB	<input type="checkbox"/>
Unannounced	<input type="checkbox"/>
Justification .....	
By .....	
Distribution / .....	
Availability Codes	
Dist	Avail and / or Special
A-1	

## LIST OF FIGURES

<u>Figure</u>	<u>Page</u>
1. The calculated rate of deposition of Mg in atoms per cc per second . . . . .	5
2. Model Atmospheric Temperature Profile . . . . .	8
3. Scale Heights of the Atmosphere and of Magnesium Atom . . . . .	9
4. Model Molecular Diffusion Coefficient . . . . .	10
5. Model Eddy Diffusion Coefficient . . . . .	11
6. The integrated downward flux of MgX . . . . .	13
7. The steady state solution for MgX at full-strength $q(h)$ . . . . .	14
8. MgX profile for various values of $q(h)$ . . . . .	16
9. Same as Figure 8 but with low value of [MgX] . . . . .	17
10. The variation of [MgX] with Eddy Diffusion Coefficient . . . . .	18
11. The variation of [MgX] with Deposition Maximum $q_{\max}$ . . . . .	19
12. Model oxygen and nitrogen density . . . . .	23
13. Model ozone and atomic oxygen density . . . . .	24
14. Model carbon dioxide density . . . . .	25
15. Steady state results for Mg compounds . . . . .	26
16. Same as Figure 15 but with reduced rate of $MgCO_3$ closure . . . . .	27
17. IRI ionosphere for local noon & geomagnetic equator . . . . .	30
18. IRI ionosphere for local midnight & geomagnetic equator . . . . .	31
19. Daytime results for $Mg^+$ ion model 2a . . . . .	32
20. Nighttime results for $Mg^+$ ion model 2a . . . . .	33
21. Daytime results for $Mg^+$ ion model 2b . . . . .	34
22. Daytime results for $Mg^+$ ion model 2c . . . . .	36
23. Daytime results for $Mg^+$ ion model 2d . . . . .	37
24. Nighttime results for $Mg^+$ ion model 2d . . . . .	38
25. Daytime one-component model Mg destruction rates . . . . .	42
26. Day and night Mg destruction rates . . . . .	43
27. Day and night solutions for Mg atom in the one-component model . . . . .	46
28. Test of sensitivity of Mg to ablation cutoff altitude . . . . .	47
29. Daytime rates for the Two Component Model . . . . .	49
30. Nighttime rates for the Two Component Model . . . . .	50
31. $Mg^+$ Profiles from the Time Dependent Model . . . . .	52
32. Profile of the ratio of $Mg^+/Mg$ . . . . .	53
33. The $Mg^+$ Column Density Diurnal Variation . . . . .	54
34. The $Mg^+$ Density Diurnal Variation . . . . .	55
35. Model eastward electric field at Jicamarca . . . . .	57
36. The influence of eastward electric fields on ion motion . . . . .	59
37. Calculated upward ion drift velocities . . . . .	60
38. Calculated density of $Mg^+$ with diurnal dependence . . . . .	62
39. Geometry of the $Mg^+$ Radiance Calculation . . . . .	64

## LIST OF FIGURES (cont'd)

<u>Figure</u>	<u>Page</u>
40. Radiance computed from the $Mg^+$ model with full deposition . . . . .	66
41. Calculated $Mg^+$ density with 25% Mg deposition . . . . .	67
42. Radiance computed from the $Mg^+$ model with 25% deposition . . . . .	68
43. Computed 25% deposition profile with Model 2b . . . . .	70
44. Radiance computed from 25% deposition and kinetic model 2b . . . . .	71
45. Ratio of $Mg^+$ to Mg as predicted by Model 2b. . . . .	72
46. Concentration of neutral Mg from Model 2b . . . . .	73

## LIST OF TABLES

<u>Table</u>	<u>Page</u>
1. NEUTRAL MG KINETIC MODEL . . . . .	21
2. CHARACTERISTICS OF THE ION MODELS . . . . .	39
3. MG ION KINETIC MODEL . . . . .	40

## **ACKNOWLEDGEMENTS**

Ed Murad and Shu Lai, PL/WSSI, were instrumental in all phases of this work from conception to completion. We are indebted to them for their technical guidance and critical evaluation. James Gardner, of PhotoMetrics, Inc., and Rodney Viereck, PL/WSSI, were most helpful in supplying results from GLO.

## 1. INTRODUCTION

It has long been known that metal ions are present in Earth's ionosphere. Metals including  $\text{Fe}^+$ ,  $\text{Mg}^+$ ,  $\text{Na}^+$ ,  $\text{Ca}^+$ , and  $\text{Si}^+$ , and have been observed optically [e.g., Vallance-Jones, 1958] and by rocket-borne mass spectrometers [e.g., Istomin, 1963]. The origin of these ions is presumably the ablation of cosmic dust particles. These extra-terrestrial materials are perhaps the remains of comets or asteroids and are distributed more or less uniformly throughout the solar system. Each year, the Earth captures some twenty thousand tons of this material as it ablates into the atmosphere below about 80 km altitude. The particles are composed of various minerals and, upon ablation, release the metals in atomic form. These metal atoms are then ionized by the sun or undergo charge exchange with the ionosphere. According to Plane [1991] magnesium and iron are the most abundant metals, making up about 12% by weight each of the average cosmic dust particle. Sodium, aluminum, nickel and calcium are also relatively abundant at about 1% to 2% by weight.

It is reasonable to assume that these metals enter the atmosphere as neutrals, because ions cannot persist at altitudes where ablation takes place. This is because recombination through three-body processes is too fast. If an ion were released at 80 km, it would rapidly become an ion complex which in turn would be rapidly neutralized. In order to maintain an ion density at high altitudes, neutrals must first be transported upward, then ionized. Modeling of thermospheric ions, then, must include deposition of the neutrals, transport of the neutrals upward and chemistry between the neutrals and the ambient ionosphere. Transport of ions and neutrals is by diffusion and by thermospheric winds. Being charged, however, ions are also subject to transport by electric fields. Earth has a permanent diurnally varying east/west electric field caused by the separation of the solar wind plasma as it impacts Earth's magnetic field. This field causes an upward or downward drift of the ions at high altitudes, where their mean free paths are long compared to the gyro-radius. Comprehensive models of thermospheric metal ions should also include these fields.

Recently, observations of metal ions were made aboard STS-53 [Murad, et al., 1994]. This experiment, called GLO, measured radiance from magnesium and calcium ions and from sodium and magnesium neutrals from various vantage points at both the dawn and dusk terminators. The experiment allowed for measurements to be taken at various geomagnetic latitudes as well. The experiment observed radiance of  $\text{Mg}^+$  and  $\text{Ca}^+$  at high tangent height altitudes on the evening side. This indicated the presence of metal ions in substantial number at high altitudes. These high radiances at high tangent altitudes were not found on the morning terminator. This behavior was prevalent near the geomagnetic equator but not so at middle latitudes, where radiances were low and confined to low altitudes at both terminators.

We have undertaken a comprehensive modeling effort in an attempt to understand these results. The model focuses on magnesium, which is representative also of calcium, in that the two have similar chemistry. The diurnal dependence of ion and neutral species is included, both through the chemistry and through the variations of the east-to-west electric field. Deposition of neutral



Mg is included with an altitude dependent deposition rate which is calculated from assumed aerodynamics and cosmic dust particle distributions. The model, which builds upon an earlier steady state model for sodium [McNeil, 1993], also includes molecular and eddy diffusion, creation of magnesium ions through charge exchange and photoionization, destruction of ions through recombination and ultimate removal of the neutrals through the creation of complex species which, forming crystals, ultimately fall to Earth or are rained out in the troposphere.

The modeling is actually comprised of several models, each building upon the previous one. First, equations of motion and of heat transfer are used to calculate an altitude profile of neutral deposition. Next, this deposition profile is used to calculate a steady state profile of the concentration of metal containing species. This intermediate step is needed in order to explore the neutral and ionic chemistry, which involves many species. From this profile, a steady state kinetic model is developed for neutrals and ions. These models are used to derive reasonably equivalent two-component models, involving only atomic Mg and  $\text{Mg}^+$ . It is necessary to obtain two-component models since the solution of the full time-dependant problem would be unnecessarily burdensome with several components; burdensome because of the computation time required and unnecessarily so because intermediates serve as transients which are not subject to diffusion. This statement is not precisely true for the species occupying the altitude range directly below neutral Mg, but more on that point later. The time-dependent problem is solved and transport by electric fields is introduced. Finally, when a diurnal profile of  $\text{Mg}^+$  has been obtained, a separate model is used to calculate radiance levels that approximate the conditions and configurations of the GLO experiment.

The next section describes briefly the calculation of the deposition function and how that function is used to arrive at a steady state profile from which the kinetics can be investigated. Following this, we investigate the kinetics of the ions and neutrals in the steady state. Next, we turn to the development of two-component models from the multi-component kinetic solutions and apply these to the time-dependent problem. The electric fields are then introduced and the daily variation of  $\text{Mg}^+$  is achieved. These results are then converted to radiance as a function of tangent height for a situation resembling the actual experiment.

## 2. THE DEPOSITION RATE

The natural first step in modeling atmospheric metals is to ask at what rate these metals are introduced into the atmosphere. To investigate this, we have performed a Monte Carlo computation in order to arrive at a deposition profile, which gives the rate per unit volume at which metal atoms are introduced as a function of altitude. This calculation is similar to one used for Na in previous work [McNeil, 1993] and will be summarized here. Details can be found in the previous reference.

The calculation begins by assuming a distribution for the mass of meteoric particles. Empirical functions have been proposed in the literature and we have adopted one based on Hughes [1975].

Spherical particles are assumed to enter Earth's atmosphere and undergo an entirely downward trajectory at an initial velocity of 14 km/second. The actual velocity of cosmic dust particles is variable, but we have found little variation of the final deposition function with initial velocity between reasonable limits of perhaps 13 km/second and 16 km/second.

After entering the atmosphere, the particle is followed downward, its velocity being governed by atmospheric drag and gravitational acceleration. At each timestep, energy balance is used to determine the ablation rate of the particle and the appropriate mass released is accumulated in bins of one kilometer altitude. The rate of ablation can be approximated by considering the rate at which energy is transferred from the air molecules to the particle and the energy needed to ablate the material in the particle itself. *Hughes* [1975] gives an equation for this ablation rate as follows.

$$\frac{dm}{dt} = - \frac{\Lambda A m^{3/2} \rho_a V^3}{2 \xi \rho_m^{3/2}} \quad (1)$$

In Eq(1)  $\Lambda$  is the fraction of energy which is absorbed from the air and used to ablate the material. This, again according to *Hughes* [1975] is somewhere between 0.1 and 0.6 and we set it at 0.2.  $A$  is a shape factor which is equal to 1.2 for a sphere.  $\rho_a$  is the density of the atmosphere.  $V$  is the particle velocity.  $\xi$  is the heat of ablation or sublimation of the material. This is typically around 5.0 ergs/gram. However, since the MgO bond is especially stable relative to the counterpart for, say, sodium, we increase this to 7.5 ergs/gram in this model.  $\rho_m$  is the density of the particle, which we take at 3.2 grams/cc.

We can see that there is substantial room for variation of parameters, even in the first equation of the model. This is a general characteristic of much of this work, that there are many parameters which can be set only quite approximately. However, in the case of Eq(1) and its resulting deposition curve, the fact is that variations effect the overall deposition rate most of all and not the actual altitude of deposition. In what follows, we will re-normalize the total deposition rate to give an ion density peak within reasonable bounds. Thus, the actual magnitude of the deposition is irrelevant here. Even so, we should keep in mind that there are many unknown parameters in this modeling, from start to finish.

To perform the calculation of deposition, we divide the altitude range into a series of bins, each 1 km in height. Beginning at some high altitude, we select representative particles uniformly distributed in  $\log_{10} m$ , where  $m$  is the mass. We follow each of these particles on its trip to Earth and, at each timestep, we accumulate in the appropriate altitude bin a fraction of the mass

$$\delta m = \frac{dm}{dt} \delta t W(m) \quad (2)$$

where  $dm/dt$  is given by Eq(1) and  $W(m)$  is a weight function giving the relative number of

cosmic dust particles between  $m$  and  $m + \delta m$ . Once this is completed for all particles, we sum up all the accumulated mass in all the altitude bins, which is in grams per second, but which is also relative since the values of  $W(m)$  are relative. We can get an absolute value if we know the total rate of deposition of material in the atmosphere. The total deposition rate is a subject of some disagreement among experts in the field. However, several authors [Hughes, 1975, Dohnanyi, 1971, Whipple, 1967] give the total influx at around 500 grams/second. We adopt this value for these calculations.

There is one more complication at this point. In reality, the deposition rate is not given by Eq(1) at high altitudes. This is because where the atmosphere is sparse, the heat absorbed can be immediately re-radiated as infrared energy. Here, there is no temperature increase and so no ablation. However, since the calculated ablation rate is essentially zero above 140 km anyway, we deal with this situation by simply setting the rate to zero above 140 km. The deposition rate curve resulting from this computation for magnesium is shown in Figure 1. The peak of the deposition is around 0.4 atoms per cc per second and comes at about 75 km altitude. The altitude of maximum deposition arises from a combination of increasing atmospheric density and the rapid decrease in particle velocity once ablation begins in earnest. According to Eq(1) the mass loss rate depends on  $V^3$ . Even for very large meteoric particles, the terminal velocity is quite small. For example, a 50 kg meteor entering the Earth at 10 km per second would slow to about 70 meters per second at an altitude of 10 km. Smaller particles, which are far more important to the total deposition due to their abundance, slow to a small terminal velocity at higher altitude, effectively ceasing to ablate. The altitude at which ablation ceases depends strongly on the initial mass of the particle, which is why we have taken pains to arrive at a solution representative of measured, if somewhat speculative, initial mass distributions.

There are several reasons why care must be taken in using this result. First, the value of the total deposition is a matter of some controversy. The actual number may be less or greater by a substantial amount. Second, we have already mentioned the uncertainty of the parameters in Eq(1). Third, it may not be that all the material that is ablated is in the form of neutral Mg. If it were ablated instead as  $Mg^+$ , it would be rapidly converted to Mg through three-body recombination. However, if it were to come off as MgO or some other polyatomic molecule, a substantial fraction might well settle to Earth before it could be dissociated chemically or by the sun. In what follows, we will allow ourselves the liberty of varying the absolute rate of deposition, multiplying the curve in Figure 1 by some factor. We will rely on the resulting total ion density to determine this factor.

Meteor Deposition Model with  $V_0 = 14.0$   
Composition 12.5 % M.W. 24.3

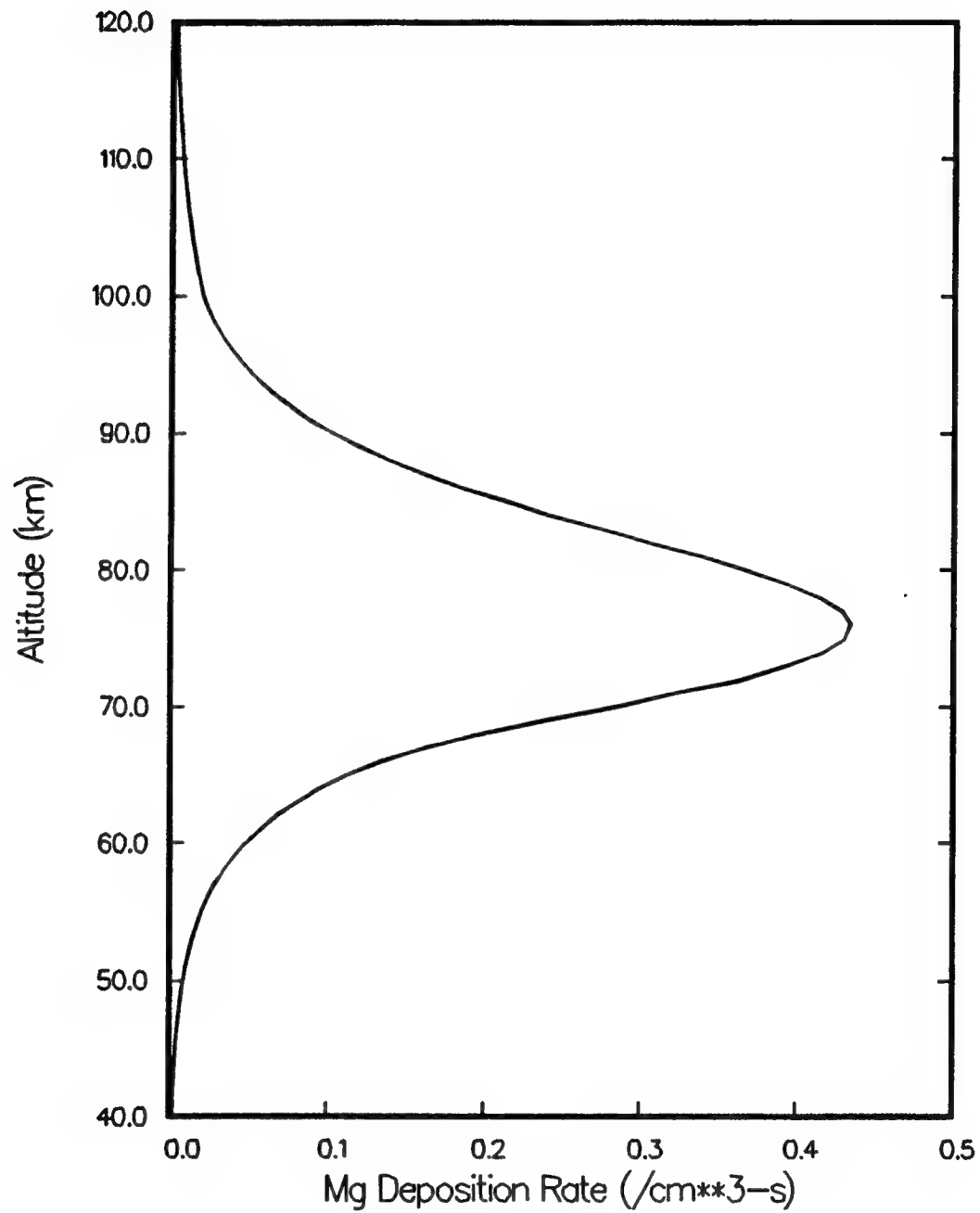


**Figure 1.** The calculated rate of deposition of Mg in atoms per cc per second.

### 3. THE STEADY STATE MODELS

It would be possible to create a fully time-dependant model simply from the deposition rate and assumed diffusion profiles and chemical reactions. However, it is prudent for several reasons to go instead through an intermediate steady state model. In the first place, the time dependant solution is computationally time consuming and one would like to include as few species as possible in it. The kinetics, on the other hand, necessarily involve several intermediate species between neutral atoms and ions. We can simplify things considerably, then, by reducing the multicomponent kinetic problem to a two component one. In order to investigate the chemistry, we will begin with a steady state model which assumes that there is a constant altitude dependent concentration of the sum of all species containing one Mg atom, called MgX. In the next section, this profile will be calculated.

#### 3.1 THE STEADY STATE PROFILE

In order to calculate the profile of MgX we need the previously computed deposition curve and the diffusion equations. These equations describe the transport of the MgX from where it is deposited to where it ends up, on the surface of Earth. Since MgX is continuously generated above the ground, in the steady state, the net flux of MgX must be downward up to the point at which MgX creation ceases and zero above this. The flux of MgX due to diffusion can be represented by [Banks and Kockarts, 1973]

$$n_1 w = -D_{12} \left[ \frac{dn_1}{dh} + \frac{n_1}{H_1} \right] - K \left[ \frac{dn_1}{dh} + \frac{n_1}{H} \right] \quad (3)$$

where  $n_1$  is the MgX density,  $D_{12}$  is the molecular diffusion coefficient,  $K$  is the eddy diffusion coefficient,  $H$  is the scale height of the atmosphere and  $H_1$  is the scale height of MgX. We have neglected thermal diffusion in Eq(3) for simplicity. Assuming that the mass of MgX is close enough to that of Mg,  $H_1$  is given by

$$H_1 = \frac{kT}{m_{MgX}g} \quad (4)$$

where  $g$  is the gravitational constant. We can solve Eq(3) by noting that above the cutoff altitude for ablation  $H_c$ ,  $nw$  is zero. Since above this altitude,  $D_{12} \gg K$ , we have immediately

$$n_{MgX}(h > H_c) = n_{MgX}(H_c) e^{-\frac{h-H_c}{H_1}} \quad (5)$$

or, that the density follows its scale height above  $H_c$ .  $h$  in Eq(5) is the height above the ground.

Below  $H_c$ , we note that the downward flux must be equal to the rate of creation of MgX at all points *above* a chosen altitude  $h$ . Equating this to  $nw$  gives us a differential equation in  $h$  as follows.

$$\frac{dn_1}{dh} = -\frac{D_{12}}{(D_{12}+K)} \frac{n_1}{H_1} - \frac{K}{(D_{12}+K)} \frac{n_1}{H} + \int_h^{H_c} \frac{q(\hat{h}) d\hat{h}}{(D_{12}+K)} \quad (6)$$

To better understand Eq(6) we note that, in the absence of deposition, the gradient of the density would be  $H_1$  well above the turbopause, where  $D_{12}$  equals  $K$ , and  $H$  well below. Above the turbopause, the distribution follows its own scale height and, below, it follows the scale height of the general atmosphere. Turbulent mixing at low altitudes causes all species to have the same scale height, regardless of mass. Measurements of turbulence and theoretical estimates of thermal balance indicate that the eddy diffusion coefficient becomes equal to the molecular diffusion coefficient between 100 and 120 km [Banks and Kockarts, 1973]. When deposition takes place, the scale height of MgX must decrease in order to accommodate for downward diffusion of the MgX complex. We also note that, since Eq(6) is a differential equation, we will need to specify the MgX density at some point in order to solve it.

Before solving Eq(6) we will introduce the parameters we need. Eq(4) gives us the MgX scale height providing we have an atmospheric temperature. The temperature was modeled by linear interpolation from data tabulated by Kelley [1989], which itself was taken from Johnson [1961]. The temperature profile is shown in Figure 2. We show the altitude range from 50 to 350 km because, ultimately, this will be the range of interest and because this same temperature profile will be used again as this work progresses. This temperature profile was used to generate the magnesium scale height  $H_1$ . The atmospheric scale height was taken from data tabulated by Kelley [1989]. These two quantities are shown in Figure 3. Next, we need the molecular diffusion coefficient  $D_{12}$ . This is represented in functional form by

$$D_{12} = AT^s/n \quad \text{cm}^2 \text{ sec}^{-1} \quad (7)$$

with  $T$  in  $^{\circ}\text{K}$  and  $n$  the atmospheric density in  $\text{cm}^{-3}$ . Typical values for  $A$  and  $s$  can be found in Banks and Kockarts [1973]. We use those for Argon in  $\text{N}_2$ ,  $A=6.64(16)$  and  $s=0.752$ . The atmospheric number density for use in Eq(7) is derived again from the tables given by Kelley [1989]. The resulting  $D_{12}$  is shown in Figure 4. We also need the eddy diffusion coefficient  $K$ . The eddy diffusion coefficient is a poorly known quantity. It is, however, quite important to the final result, as we shall see. We use a  $K$  profile that was determined by Johnson and Gottlieb [1970] from analysis of global average energy balance. The profile is shown in Figure 5.

As mentioned, the eddy diffusion coefficient is not well known and is probably quite variable. Banks and Kockarts [1973] present two possibilities for  $K$ . Both peak at approximately  $1(7) \text{ cm}^3 \text{ sec}^{-1}$ . However, one has a peak at 110 km altitude while the other peaks at about 100 km. We

## Atmospheric Temperature after Johnson [1961]

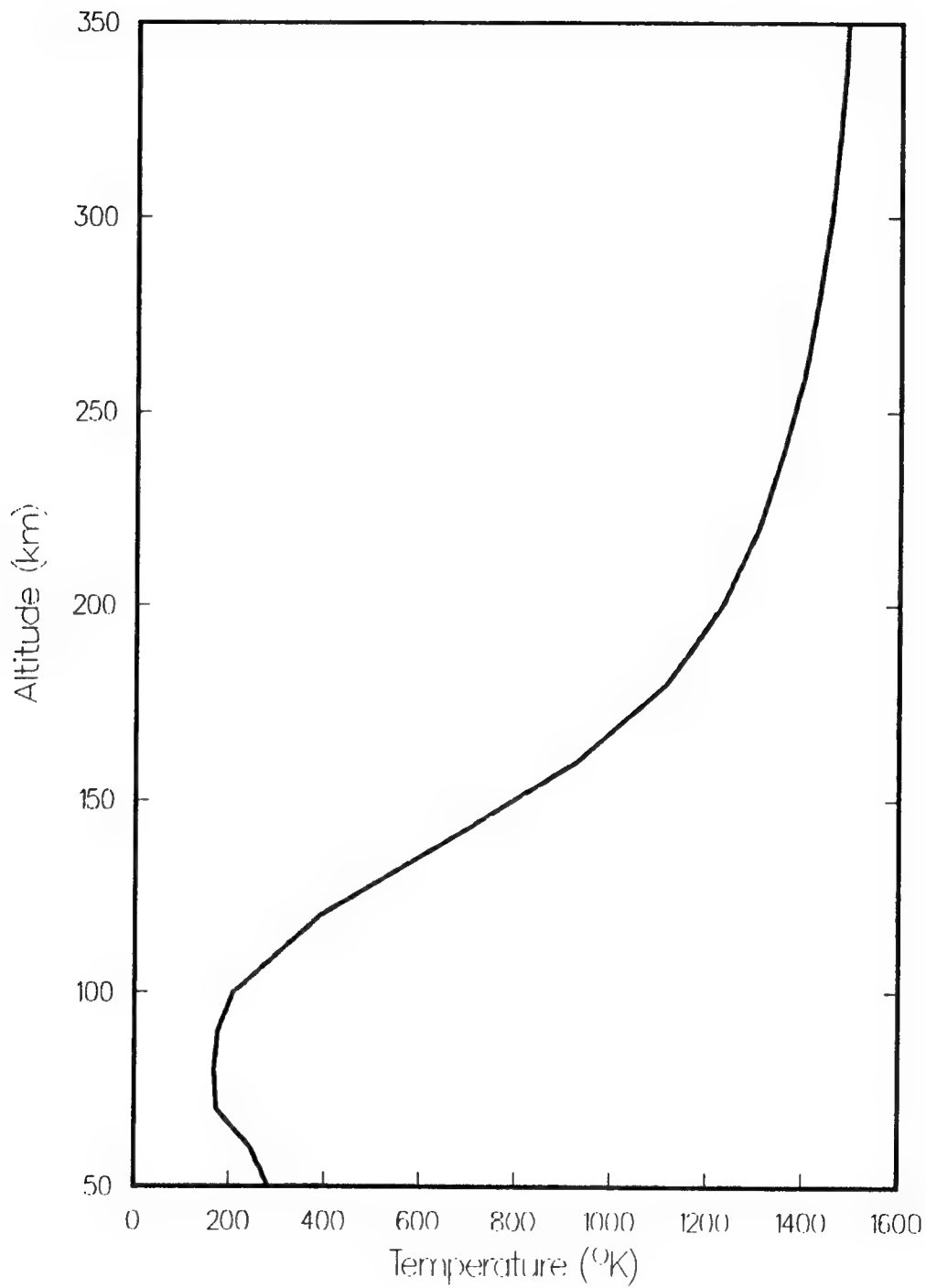


**Figure 2. Model Atmospheric Temperature Profile.**

## Atmospheric and Mg Scale Heights

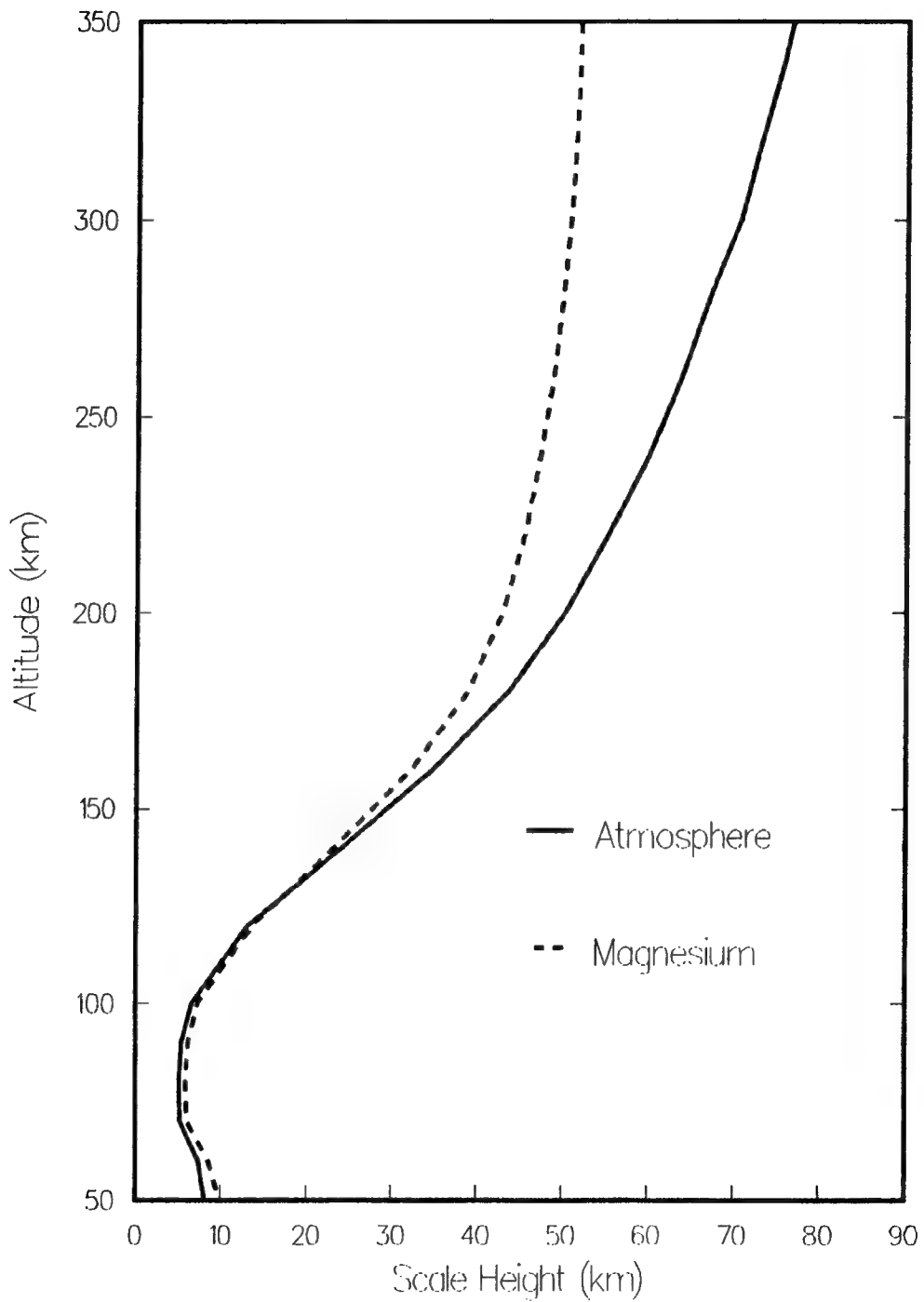


**Figure 3. Scale Heights of the Atmosphere and of Magnesium Atom.**



# Molecular Diffusion Coefficient (Ar/N<sub>2</sub>)

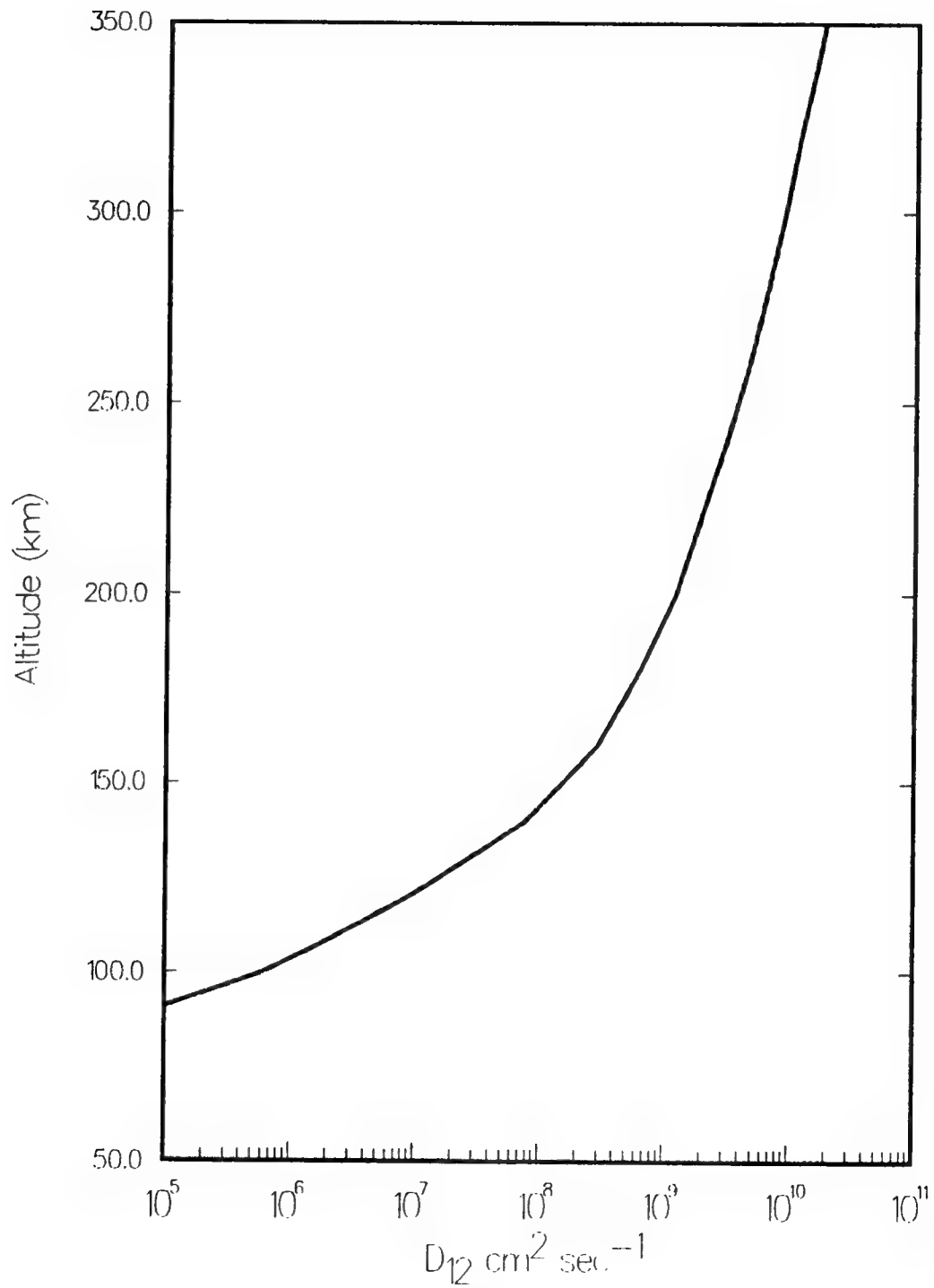


**Figure 4. Model Molecular Diffusion Coefficient.**

## Model Eddy Diffusion Coefficient

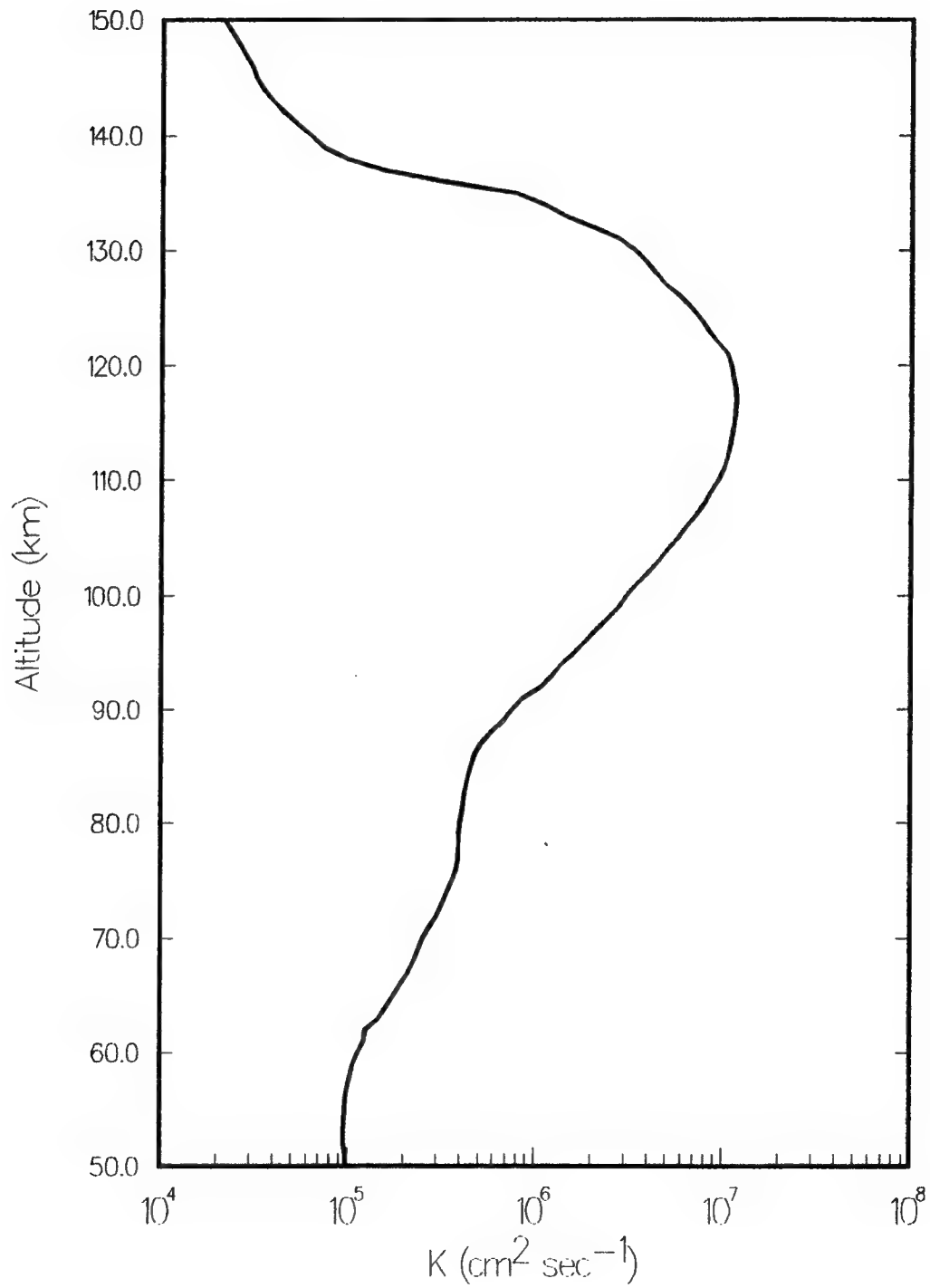


**Figure 5. Model Eddy Diffusion Coefficient.**

will investigate the relationship between altitude of the peak in K and resulting MgX concentrations in what follows.

To simplify the solution of Eq(6) we evaluate the integral on the left-hand side before integrating the equation. This evaluation is done by a simple summation of  $q(h)$  up to the maximum ablation altitude, which is taken to be 140 km. This gives the steady-state downward flux of MgX at each altitude and is shown in Figure 6. At altitudes below the region of ablation, the peak downward flux comes out to about  $8(5) \text{ cm}^{-2} \text{ sec}^{-1}$ . For comparison, *Plane* [1991] uses a value of about  $2(4) \text{ cm}^{-2} \text{ sec}^{-1}$  for sodium, which by virtue of its relative composition in meteoric material should be a factor of ten or so lower. *Carter and Forbes* [1993] use a value for iron atoms of  $5(5) \text{ cm}^{-2} \text{ sec}^{-1}$ . Iron is near in relative composition to magnesium and thus this value agrees well with our result. We should point out, however, that these authors go on to make the assumption that only about 10% of this material is actually ablated in the form of atomic neutral or ion, an issue we will return to shortly.

With these results in hand, we are ready to obtain the MgX profile from Eq(6). All that remains is to select a starting point for the calculation and an initial value for the density. Since almost all of the ablation takes place above 50 km, it seems reasonable to begin here. Figure 7 shows profiles resulting from various selections of the value of  $[\text{MgX}]$  at 50 km. We note that the curves in Figure 7 are plotted only up to 150 km. This is sufficient since above the assumed cutoff for ablation at 140 km, the density is given entirely by  $H_1$  since at that altitude, the molecular diffusion coefficient is much larger than the eddy diffusion coefficient.

There are several features present in the profiles which deserve attention. First, we see that at low values of  $[\text{MgX}]_{50}$  the behavior above about 80 km is identical. This arises because, according to Eq(6), if  $n_1$  is small enough,  $n_1$  becomes an *increasing* function of  $h$ . In a certain regime, the density of MgX at 80 km is independent of the density at 50 km, so long as the density at 50 km is low enough. Although difficult to model precisely, heterogeneous removal at low altitudes might well lead to corresponding low density of MgX. In this process, crystals would form and fall directly to Earth removing Mg containing species. Thus, it seems a reasonable solution to assume a low density at low altitudes. At higher values of  $[\text{MgX}]_{50}$  the deposition becomes less important relative to the scale height so that the peak in MgX is not observed. We can understand these results as follows. First, assume that there is no deposition and the MgX profile follows a simple exponential altitude dependence. If we then deposit some Mg above an altitude  $h$  the density gradient must shift so that there is less MgX immediately below  $h$  in order to transport that Mg deposited above. If we push this far enough, the only possibility is that the density below  $h$  becomes less than that above, leading to a peak in the MgX profile.

A second thing to note from Figure 7 is that the scale height of MgX above approximately 80 km altitude is not dependent on the choice for  $[\text{MgX}]_{50}$ . This is simply because the deposition term in Eq(6) becomes small above 80 km. The result is important, though, because we will see that atomic Mg and  $\text{Mg}^+$  exist only above 80 km. This means that the choice for  $[\text{MgX}]_{50}$  is not especially important except in that it may change the absolute amount of Mg or  $\text{Mg}^+$  at

# Calculated MgX Downward Flux

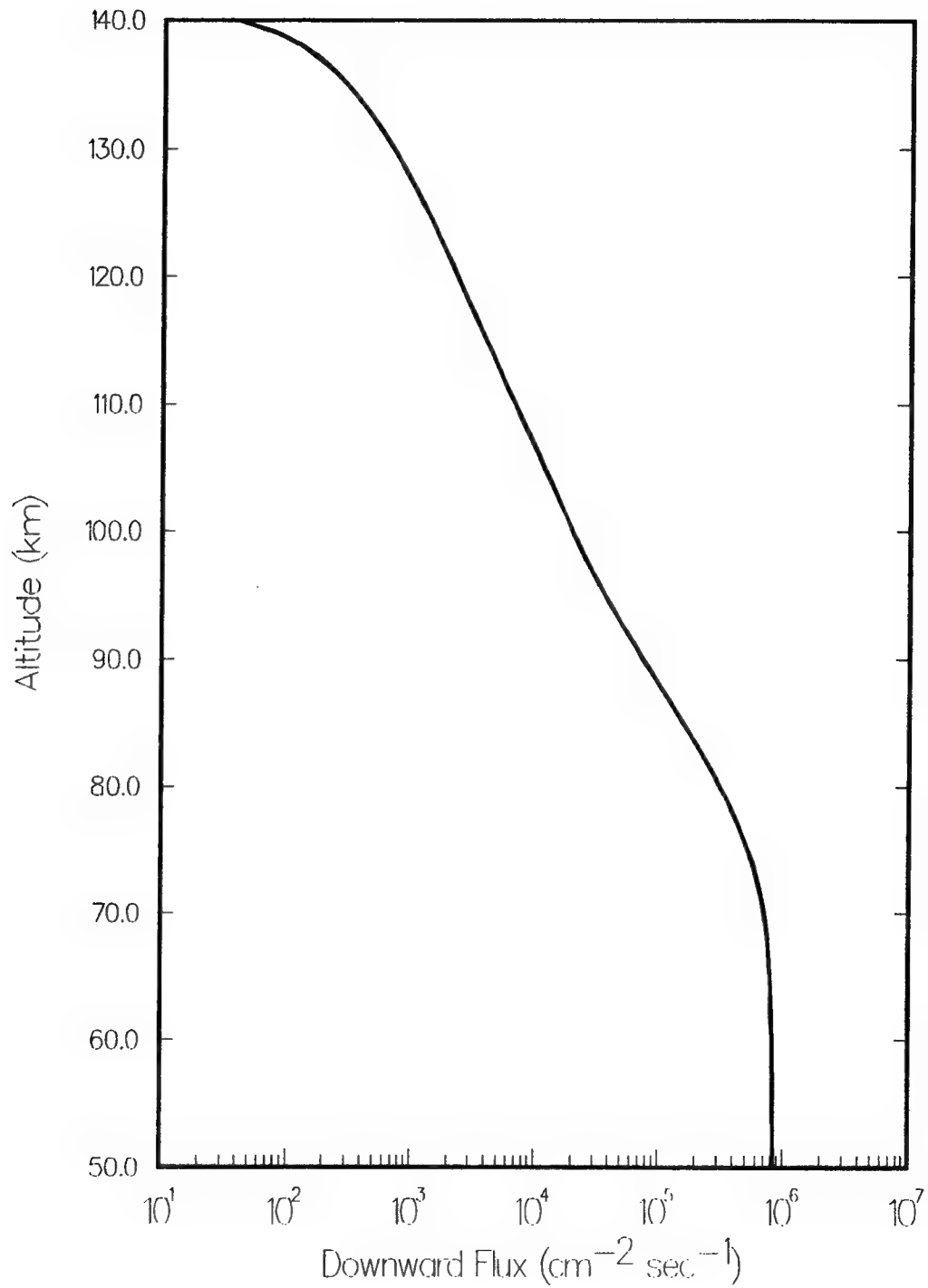


**Figure 6.** The integrated downward flux of MgX.

Total Mg Species Concentrations  
for  $V_0 = 14$

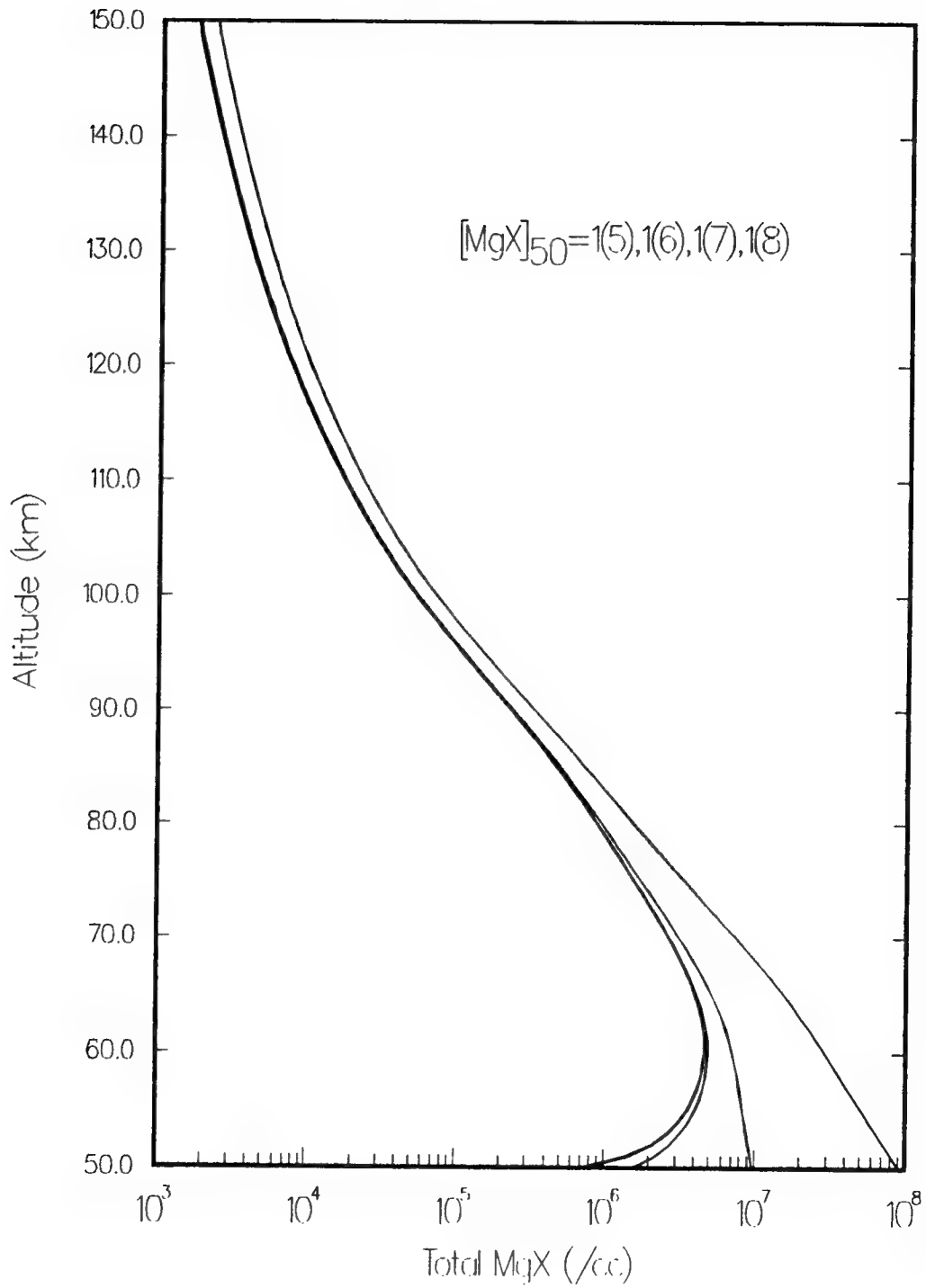


**Figure 7.** The steady state solution for MgX at full-strength  $q(h)$ .

all altitudes above 80 km. We will also see that the results in Figure 7 predict far too much atomic Mg and  $\text{Mg}^+$ , so that we will need to scale the results of Figure 7 anyway. The end result is that the choice for  $[\text{MgX}]_{50}$  is not important to the result, up to a constant that scales the density of all species at all altitudes. For comparison, this same computation for Na gives quite reasonable peak values of atomic Na at 85 km. It is remarkable, then, that the model predicts so much MgX. Heterogeneous removal must be especially important for Mg or it must be that a large fraction of the meteoric metal never reaches atomic form.

We can investigate the dependence of density on deposition by repeating the computation with some factor  $\alpha$  multiplying the deposition function. In Figure 8 we show the results for three choices of  $\alpha$ . Clearly, the profiles scale linearly, as they should from examination of Eq(6). Here, we have chosen to scale the value of  $[\text{MgX}]_{50}$  along with  $q(h)$ . If we start with a very low value for  $[\text{MgX}]_{50}$  the results are quite different. Figure 9 shows the same three values of  $\alpha$  as in Figure 8 but with starting point at  $1(3)\alpha / \text{cm}^3$ . Although there is still about one decade of difference between the curves at low altitude, the difference becomes larger at high altitude, especially for the lowest  $q(h)$  value.

All this would be quite troublesome except for the fact that these profiles will serve only as vehicles for the investigation of the chemistry. They will ultimately be discarded in favor of a time dependant solution, which does not depend strongly on the boundary conditions. However, it is instructive to investigate the dependence of these curves on the other parameters because the time dependant calculation will be time consuming and variation of parameters there is less appealing. First, we examine the dependence of the profile on the eddy diffusion coefficient. To do this, we shift the coefficient downward by 5 to 10 km. Figure 10 shows the results. With a lower peak height of the eddy diffusion coefficient, we find a reduction in the peak height of MgX. This can be understood by noting that the eddy diffusion coefficient profile used for these models decreases with decreasing altitude. When the peak height is lowered, the rate of diffusion in the area of maximum deposition is increased. This in turn allows for more downward transport and a lower steady state density. Alternately, we can look at Eq(6) to find that increasing  $K$  at low altitudes effectively decreases the deposition rate inversely. Quantitatively, the change in the eddy diffusion coefficient between its supposed extremes gives rise to a change in MgX density by about a factor of three.

Another parameter which might be varied is the height of the maximum of the deposition curve. Figure 11 shows the results for a five kilometer change in the peak height, centered around the calculated peak height of about 75 km. Oddly, the higher deposition peak gives less MgX at higher latitudes. We believe this has to do again with the height variation of the eddy diffusion coefficient. When the deposition curve is at higher altitudes, eddy diffusion is more effective in removing the MgX so that less is necessary around 90 km to maintain the downward flux. Overall, the variation is on the order of a factor of three with a 10 km variation in peak height.

In summary, we have found that the steady state MgX solution is quite sensitive to the choice of low altitude initial value when the initial value is large. At smaller initial values, however, the solution becomes rather insensitive to the choice. We have seen that the solution scales

# Total Mg Species Concentrations for Various Deposition Rates

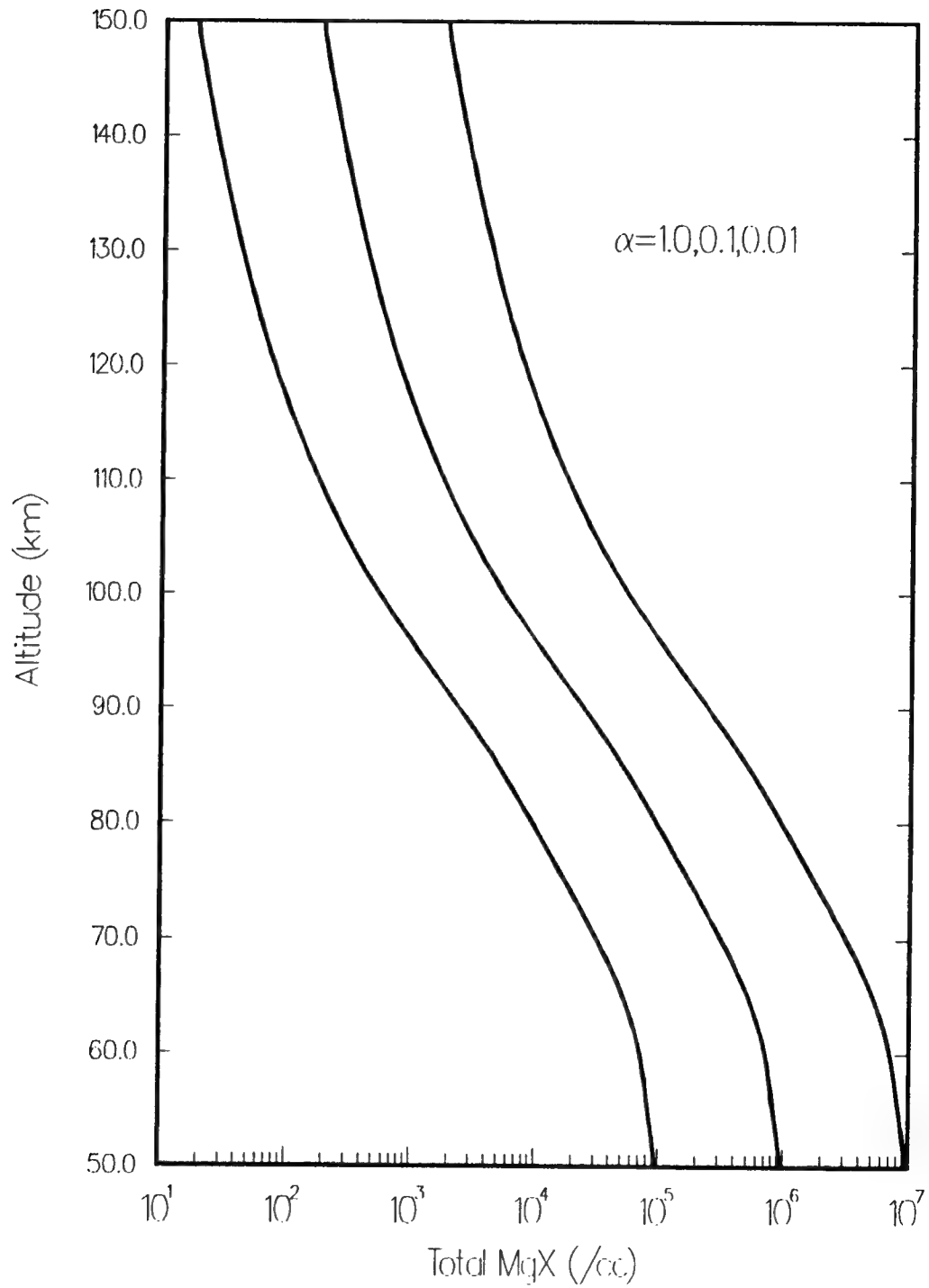


**Figure 8.** MgX profile for various values of  $q(h)$ .

# Total Mg Species Concentrations with Various Deposition Rates

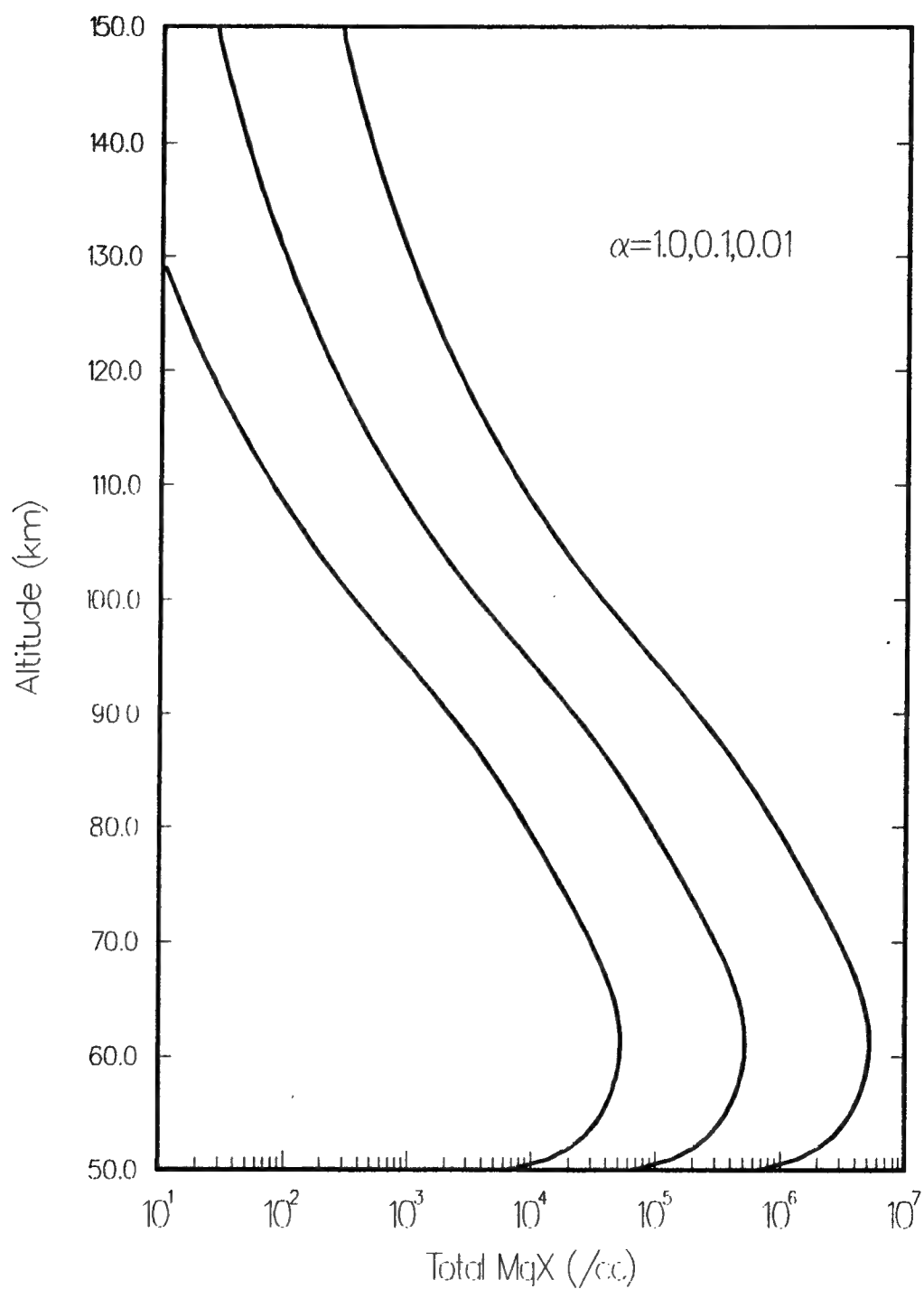


**Figure 9.** Same as Figure 8 but with low value of [MgX].



# Total Mg Species Concentrations with Various Eddy Diffusion Profiles

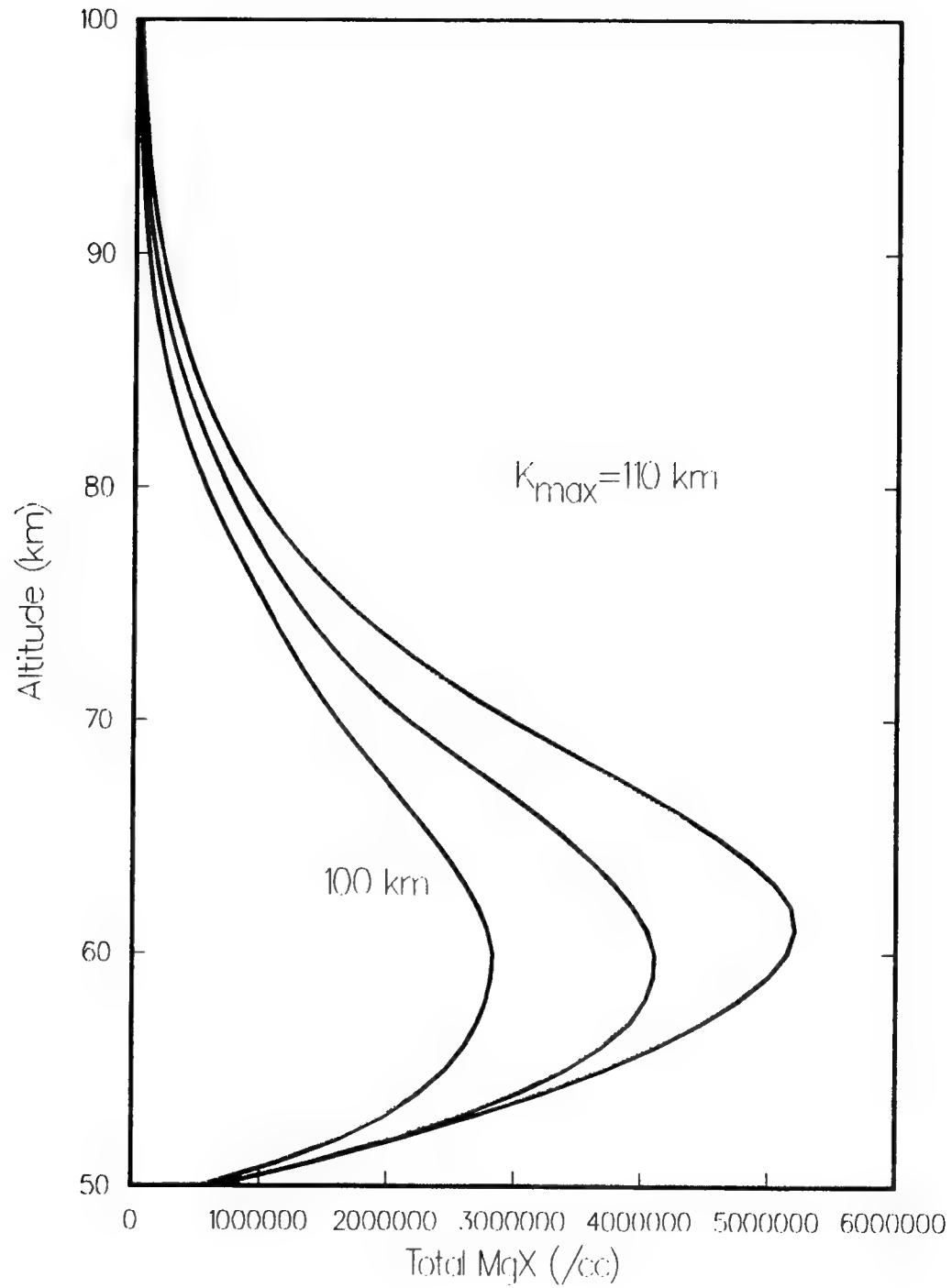


**Figure 10.** The variation of [MgX] with Eddy Diffusion Coefficient.

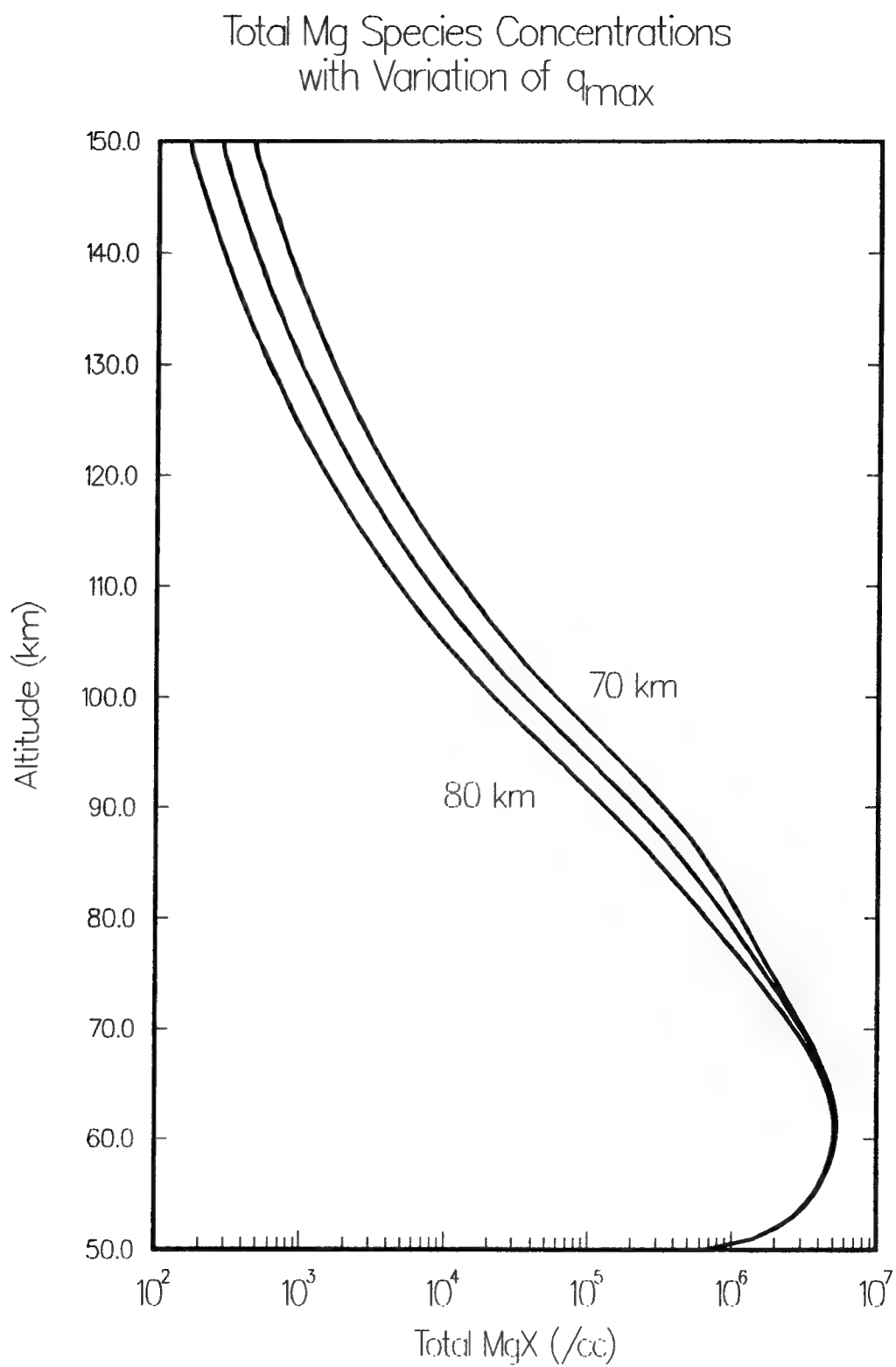


**Figure 11.** The variation of [MgX] with Deposition Maximum  $q_{\max}$ .

approximately linearly with the deposition rate  $q(h)$ . We have seen that variation of the eddy diffusion coefficient and of the height of  $q(h)$  gives rise to noticeable but not too large variations in the calculated rate. In the next section, these profiles will be used to investigate the neutral and ion chemistry of magnesium.

### 3.2 NEUTRAL CHEMISTRY

The neutral chemistry used in this model is kept relatively simple. We wish to arrive ultimately at a rate with which atomic Mg is removed from the atmosphere. Atomic Mg is assumed to undergo a three-body reaction with  $N_2$  and  $O_2$  to form  $MgO_2$



This reaction has been studied by *Nien, et al.* [1993]. These authors provide a functional form for the temperature dependence of the reaction. To simplify matters, since the reaction is important only below about 90 km or so, we will use a single value evaluated at 200° K. This comes out to  $4.3(-36) \text{ cm}^6\text{-sec}^{-1}$ .

In the steady state model to be used here, all intermediate molecules must be allowed to re-cycle. If this were not true, the steady state result would contain only the intermediate compound at all altitudes. To allow for the re-cycling of  $MgO_2$  we include the reaction



The rate of this reaction has not been measured, but has been estimated by *Plane* [1991] for  $NaO_2$  to be  $2(-14)$  at 200°K. We will use this value in our model. From  $MgO$ , the magnesium can be converted back to atomic neutral through the reaction



*Plane and Husain* [1986] give a value of  $2.2(-10)$  to this reaction rate for  $NaO$ . We will use a value of  $1.0(-10)$  here, in that the  $MgO$  bond is somewhat more stable than that of  $NaO$ . In the case of sodium, this is the reaction that gives rise to the nightglow, since some of the atomic Na is left in the excited  $^2P$  state.

**TABLE 1. Neutral Mg Kinetic Model**

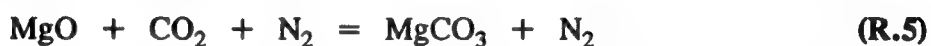
#	Reaction	Rate	Source
1	$\text{Mg} + \text{O}_2 + \text{N}_2 = \text{MgO}_2 + \text{N}_2$	4.3(-36)	<i>Nien, et al. [1993]</i>
2	$\text{MgO}_2 + \text{O} = \text{MgO} + \text{O}_2$	2.0(-14)	<i>Plane [1991]</i>
3	$\text{MgO} + \text{O} = \text{Mg} + \text{O}_2$	1.0(-10)	<i>Plane and Husain [1986]</i>
4	$\text{Mg} + \text{O}_3 = \text{MgO} + \text{O}_2$	2.0(-10)	<i>Helmer, et al. [1993]</i>
5	$\text{MgO} + \text{CO}_2 + \text{N}_2 = \text{MgCO}_3 + \text{N}_2$	2.0(-27)	<i>Ager and Howard [1986]</i>
6	$\text{MgCO}_3 + \text{O} = \text{MgO}_2 + \text{CO}_2$	1.0(-13)	<i>Plane [1991]</i>

This sequence amounts to a complete cycle for Mg. However, it suffers in that the step involving the tri-molecular reaction is quite slow at stratospheric temperatures. A reaction that is probably more important is that between atomic Mg and ozone,



This reaction is the main path to NaO for sodium, at least where the reaction is of greatest importance. The same can be expected for Mg. The reaction rate has not to our knowledge been measured, but the corresponding rate for the Ca and O<sub>3</sub> reaction [*Helmer, et al., 1993*] is around 3(-10) at 200° K. For sodium, [*Plane, 1991*] the adopted rate is 1(-10) at 200° K. We will use the value of 2.0(-10) since the bond strength of MgO is between that of CaO and NaO.

Reaction 3 re-cycles MgO to atomic Mg. However, another possibility is the reaction of MgO with CO<sub>2</sub> to form magnesium carbonate MgCO<sub>3</sub>.



where we have used N<sub>2</sub>, the most abundant neutral in the region of interest, to represent any third body. For the case of sodium, which has been most extensively studied, *Ager and Howard [1986]* give a value of 1.3(-27) for this reaction at 200° K. We will adopt this value for the MgO reaction as well. Finally, we need a closure reaction to re-cycle MgCO<sub>3</sub>. For this, we choose the reaction with atomic oxygen



and follow *Plane [1991]* in assigning an estimated rate constant of 1.0(-13) to the reaction. This model, although somewhat simplistic, should be sufficient for our purposes. Being interested primarily in the ion chemistry, the purpose of the neutral model is to provide a background upon which to superimpose the ionic reactions and to serve as a bridge between deposition and

transport in the neutral model. Eventually, we will replace even this simple kinetic model with an even simpler one which represents just a removal rate for the deposited neutral magnesium. Now, though, we will take a look at the predictions of this steady state system.

In order to evaluate the model, given the previously calculated MgX profiles, we need models of the neutral species  $O_2$ ,  $N_2$ ,  $O$ ,  $CO_2$  and  $O_3$ . For the major atmospheric constituents  $N_2$  and  $O_2$  we have assumed perfect mixing below 83 km and have applied the U.S. Standard Atmosphere mixing ratios of 78.06% and 20.94% respectively [NOAA, 1976]. These have been applied to the total atmospheric density curve given in Kelley [1989]. Above 83 km, we have used the densities tabulated in the U.S. Standard Atmosphere directly. The density of atomic oxygen and ozone were represented as functional fits to the modeling results of Allen, *et al.* [1984]. The  $CO_2$  profile was generated from another functional fit to data presented by Keneshea, *et al.* [1979]. These profiles are shown in Figures 12 through 14.

The steady state model is solved as described in McNeil [1993] and results in the profiles shown in Figure 15. The peak in the atomic Mg comes at about 84 km and has a maximum value of about  $2(5) / \text{cm}^3$ . There is a corresponding peak in the intermediate MgO density at about the same altitude. Below about 80 km, the Mg is entirely in the form of  $MgO_2$  or  $MgCO_3$  with  $MgO_2$  dominating. We should make note of the fact that the low altitude behavior is somewhat speculative, due to the uncertainty in the rate coefficients for the "closure" reactions, and also to the fact that the kinetic model is not entirely comprehensive. The behavior of the atomic Mg peak is, however, quite insensitive to the complications of the low altitude chemistry. To demonstrate this, we show in Figure 16 the comparable result for a reduction in the rate coefficient for Reaction 6 by a factor of ten. There, we see that the predominant species is now  $MgCO_3$ . However, the profile of neutral Mg is little changed, peaking at about  $2.2(5) / \text{cm}^3$  as opposed to  $2.5(5) / \text{cm}^3$  in the previous case. Since it is the atomic Mg profile that will ultimately determine the  $Mg^+$  behavior, this model appears to suffice in either form.

Since this model will be used to examine the diurnal dependence of magnesium and magnesium ion, the day-to-night variation in atmospheric constituents is of importance. Above about 80 km, the density of atomic oxygen varies little from night to day [Thomas, *et al.*, 1983]. However, below 80 km, three-body recombination quickly reduces the density after sunset. The effect of greatly reducing the atomic oxygen below 80 km is to deplete almost entirely the atomic Mg density at the same altitudes. Of course, since this is a steady state model, this does not effect the atomic Mg density above 80 km. This complication will be discussed in relation to the time-dependent model to come. At this point, we simply note in passing that the curve in Figure 13 represents a nighttime atomic oxygen density. A daytime profile would be more or less flat below 80 km or so. This would, in effect, increase the atomic Mg below 80 km in the steady state model. This would not, however, effect the peak height of the Mg or  $Mg^+$  layers and would change the Mg column density only by a few percent.

# Model Atmosphere

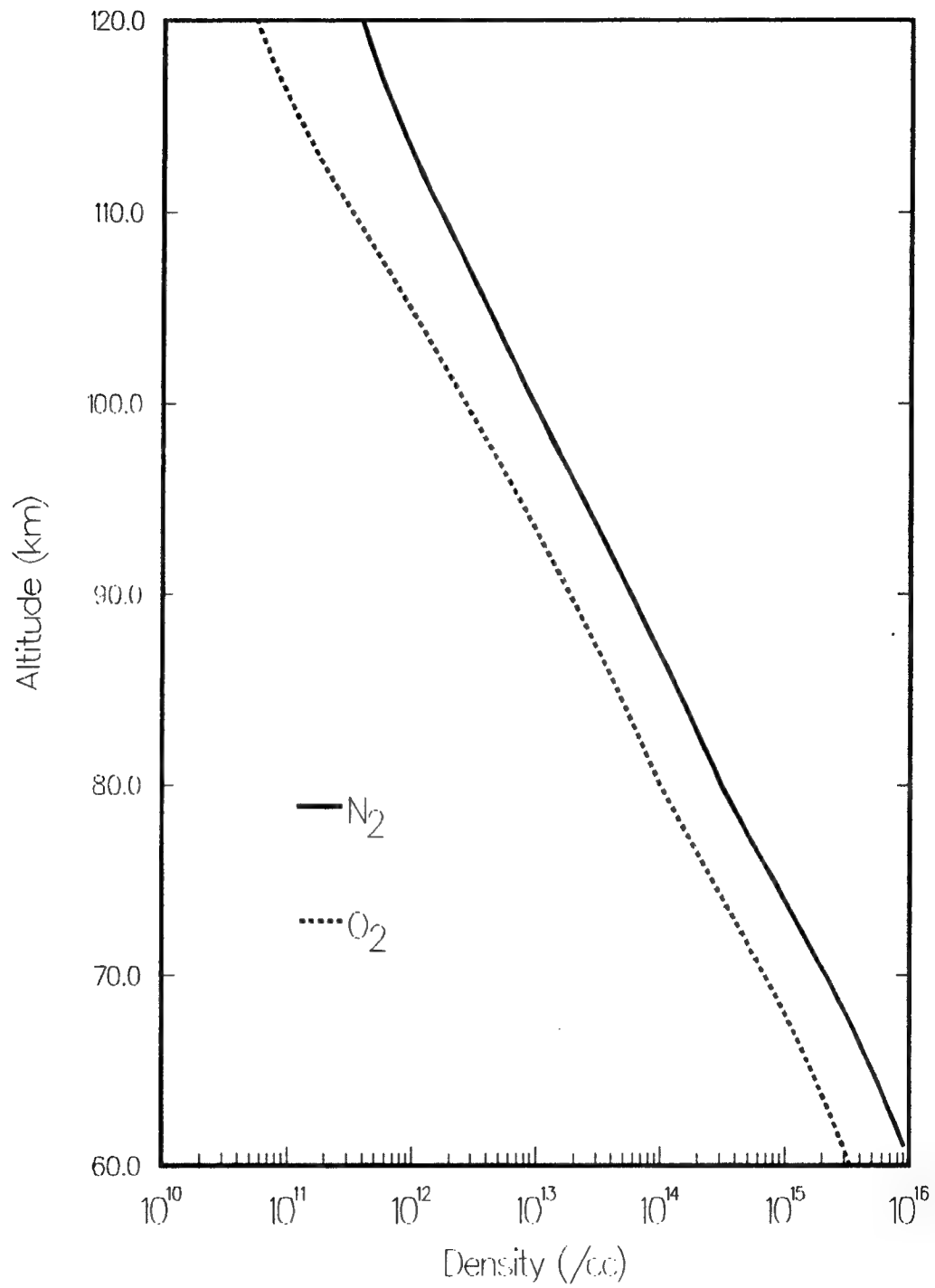


**Figure 12.** Model oxygen and nitrogen density.

# Model Atmosphere

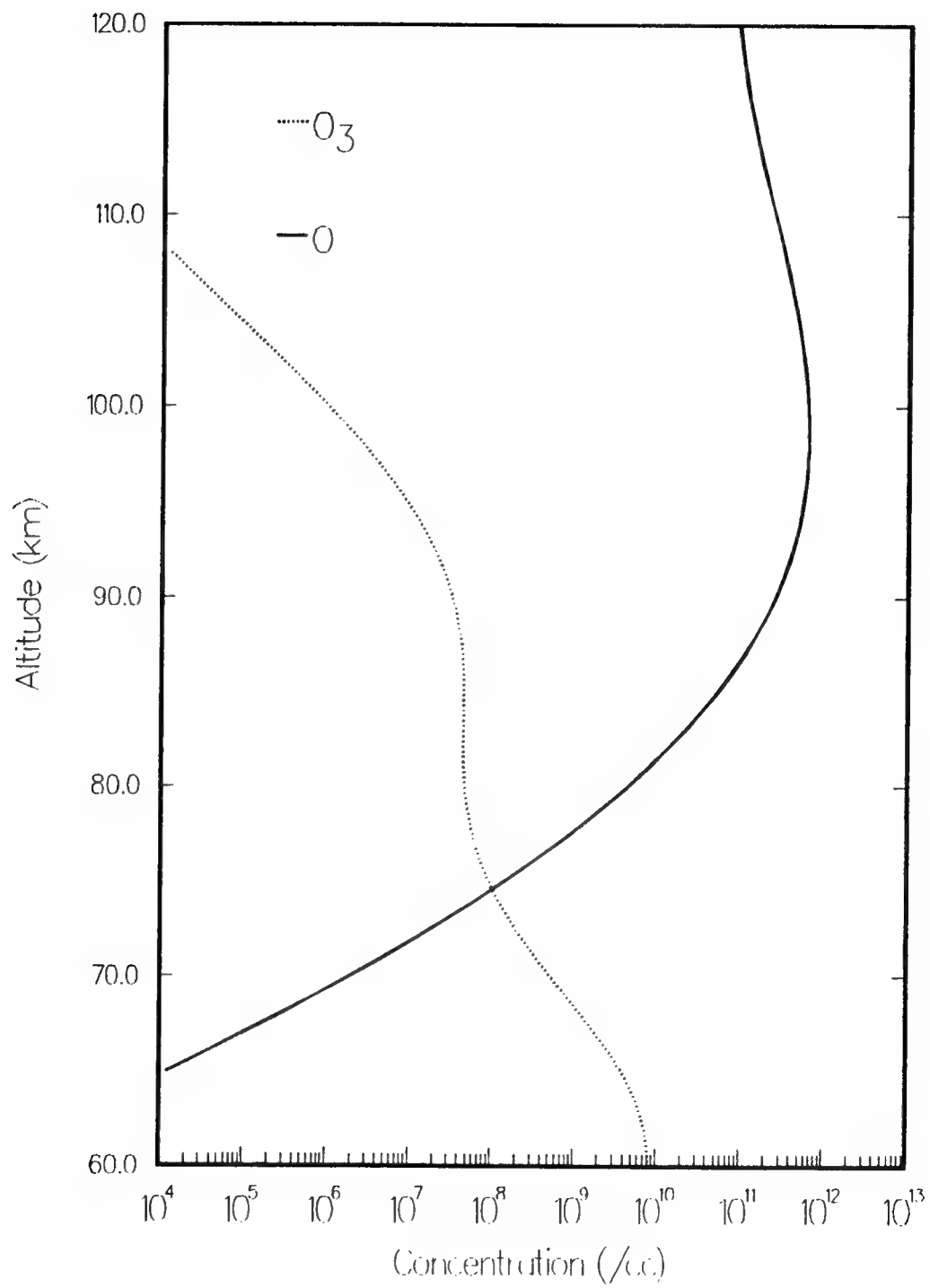


**Figure 13. Model ozone and atomic oxygen density.**

# Model Atmosphere

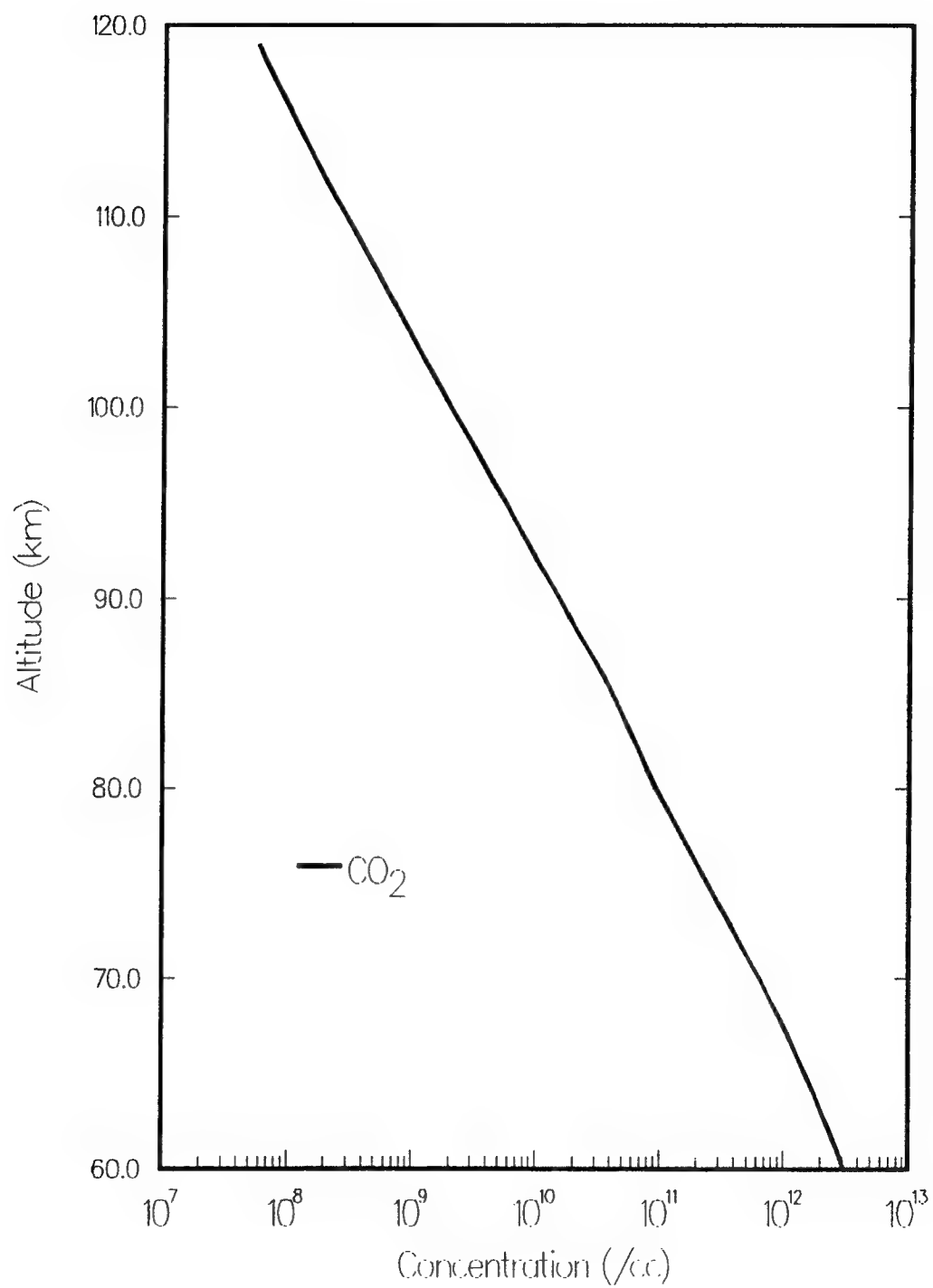


**Figure 14.** Model carbon dioxide density.



Steady State Neutral Mg Model  
Full Strength Deposition —  $K_{\max}=100$

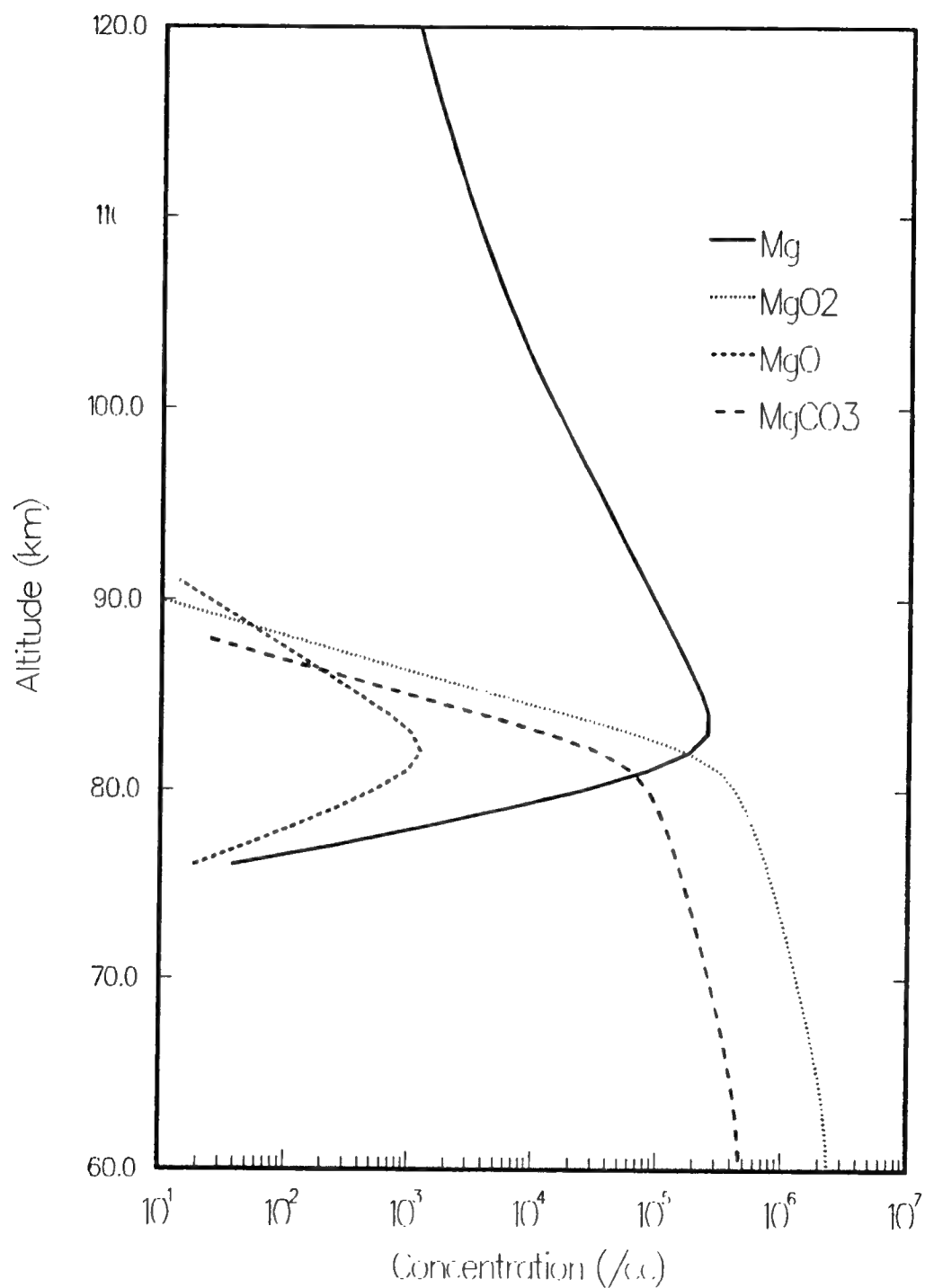


**Figure 15.** Steady state results for Mg compounds.

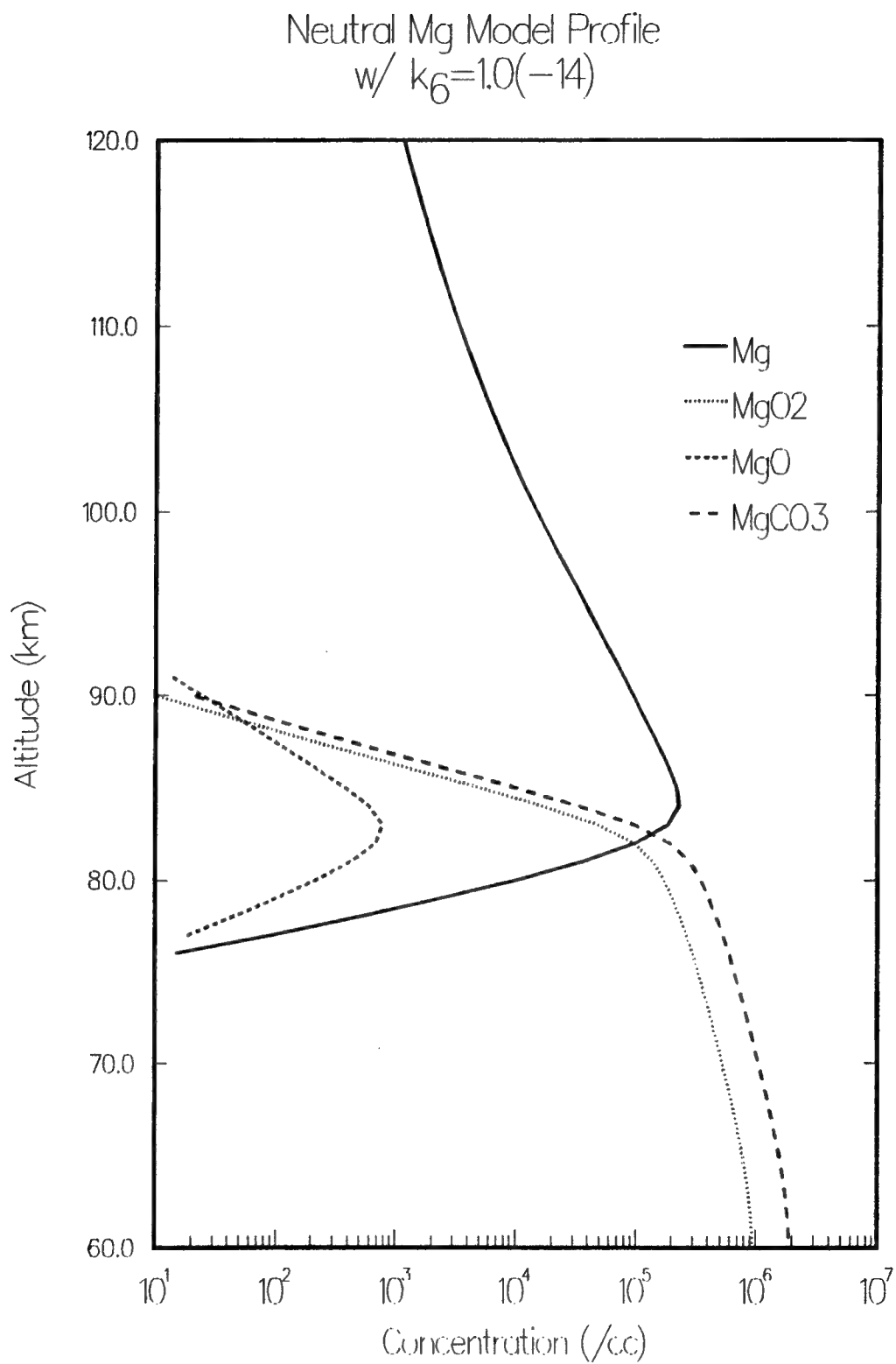
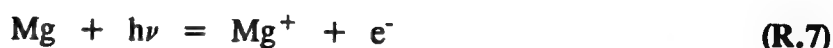


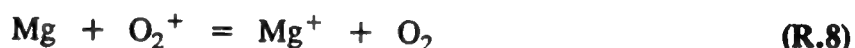
**Figure 16.** Same as Figure 15 but with reduced rate of MgCO<sub>3</sub> closure.

### 3.3 ION CHEMISTRY

The model for the  $\text{Mg}^+$  ion chemistry will be explored here in some detail. The creation of  $\text{Mg}^+$  is through photoionization in the daytime and through charge exchange with the ambient ionosphere both in the day and at night. Photoionization



takes place at a rate of  $4.0(-7) \text{ sec}^{-1}$  according to *Swider* [1969]. Rates for the charge exchange reactions



and



have been taken at  $1(-10) / \text{cm}^3\text{-sec}$  by *Aiken and Goldberg* [1973]. We have added charge exchange with atomic oxygen ion

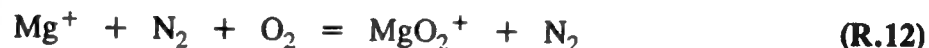


with an estimated rate coefficient of  $1(-10) / \text{cm}^3\text{-sec}$  as well, in consideration that our model will extend to higher altitudes where  $\text{O}^+$  becomes prevalent. None of the rate coefficients for charge exchange with neutral Mg is very well known. The values for the first two were based on extrapolations of high energy cross section measurements performed by *Rutherford, et al.* [1971]. These measurements indicate a rate for atomic oxygen ion that is at least equal to that of the other two and perhaps greater. The precise rates for the charge exchange reactions are not critical to these studies, as we will see later.

$\text{Mg}^+$  can be destroyed through radiative recombination



with a rate coefficient of  $1(-12) / \text{cm}^3\text{-sec}$  [*Bates and Dalgarno*, 1962].  $\text{Mg}^+$  can also form molecular ions. A three body reaction



takes place at a rate of  $2.5(-30) / \text{cm}^6\text{-sec}$  [*Ferguson and Fehnsenfeld*, 1968]. The  $\text{MgO}_2^+$  complex can then undergo molecular dissociative recombination



which is a fast process with thermal electrons. The rate of this is estimated by *Swider* [1969] to be  $3(-7) / \text{cm}^3\text{-sec}$ . There are several more reactions to consider, but this set makes one

complete cycle. We will begin the evaluation using this set, then add or modify the reactions to examine the effects. By beginning simply, we can better grasp the importance of specific reactions and rates on the overall result. The kinetic models are tabulated in Appendix A, with this model denoted as Model 2A.

In order to evaluate these models, we will require a model of the ionosphere. This has been generated from the International Reference Ionosphere (IRI) evaluated for default conditions at the geomagnetic equator. We use two models, one evaluated at noon and a second at midnight. These are shown in Figures 17 and 18 respectively. The apparent noise whenever one or the other of the densities is small relative to another arises from the fact that the IRI program used decimates at integral 1% relative concentrations. It is of no concern since charge exchange occurs in the model with all three species at the same rate.

The six-component steady state model was solved for both noon and midnight conditions and profiles are shown in Figures 19 and 20 respectively. The peak ion density is about 4,000 /cm<sup>3</sup> at noon and 1,000 /cm<sup>3</sup> at night. The day-to-night variability is most pronounced in the Mg ion. At night, the decrease in the plasma density between 100 and 150 km results in a decrease in Mg ion. This comes about because of the decrease in the production rate relative to the creation rate of MgO<sub>2</sub><sup>+</sup>, which appears to be the slow step in the process of Mg<sup>+</sup> destruction. This indicates that, in this model, the major route to destruction of Mg<sup>+</sup> is through MgO<sub>2</sub><sup>+</sup>. This fact will become more significant when we investigate a second possible reaction for MgO<sub>2</sub><sup>+</sup> which has been proposed but never definitively demonstrated.

Another possible path to the destruction of Mg<sup>+</sup> is through reaction with ozone



*Ferguson and Fehnsenfeld* [1968] give a rate constant of 2.3(-10) cm<sup>3</sup> sec<sup>-1</sup> for this reaction. The intermediate MgO<sup>+</sup> can then undergo molecular dissociative recombination



with an estimated rate [Swider, 1969] of 1(-7) cm<sup>3</sup> sec<sup>-1</sup>. We will examine the effect of these two reactions in Model 2B, for which the daytime profiles of Mg and Mg<sup>+</sup> are shown in Figure 21. The profile of the Mg<sup>+</sup> ions has changed little from the addition of this reaction. The destruction has depleted the ions below about 105 km somewhat and the peak density has fallen from about 4,000 cm<sup>-3</sup> to 3,000 cm<sup>-3</sup>.

There are other possibilities for both intermediate molecular ions. MgO<sub>2</sub><sup>+</sup> can react with atomic oxygen to form MgO<sup>+</sup>



and MgO<sup>+</sup> itself can be recycled back to magnesium ion by a similar reaction

IRI Ionosphere on 1 January  
Noon L.T. at Magnetic Equator

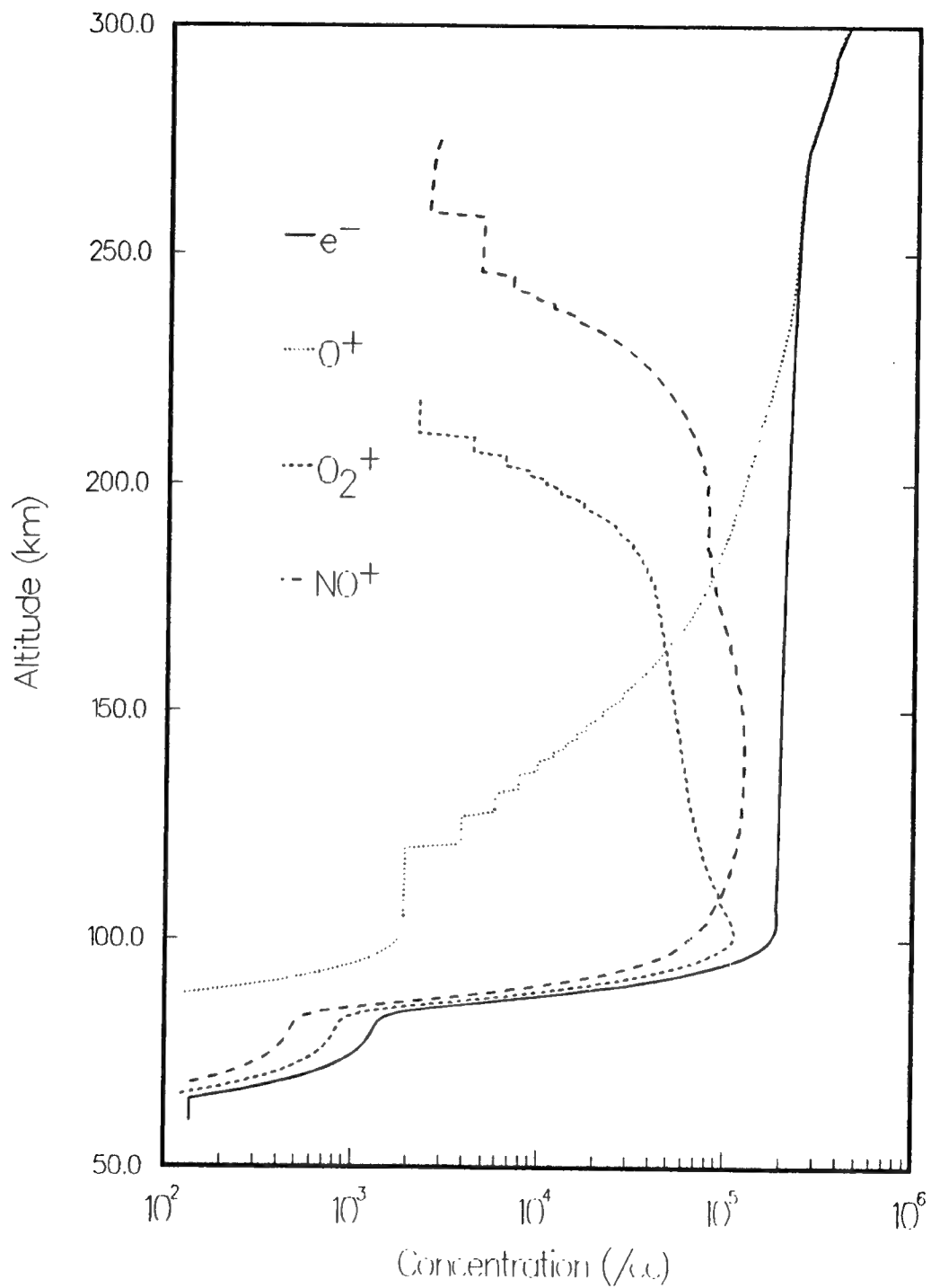


**Figure 17.** IRI ionosphere for local noon & geomagnetic equator.

IRI Ionosphere on 1 January  
Midnight L.T. at Magnetic Equator

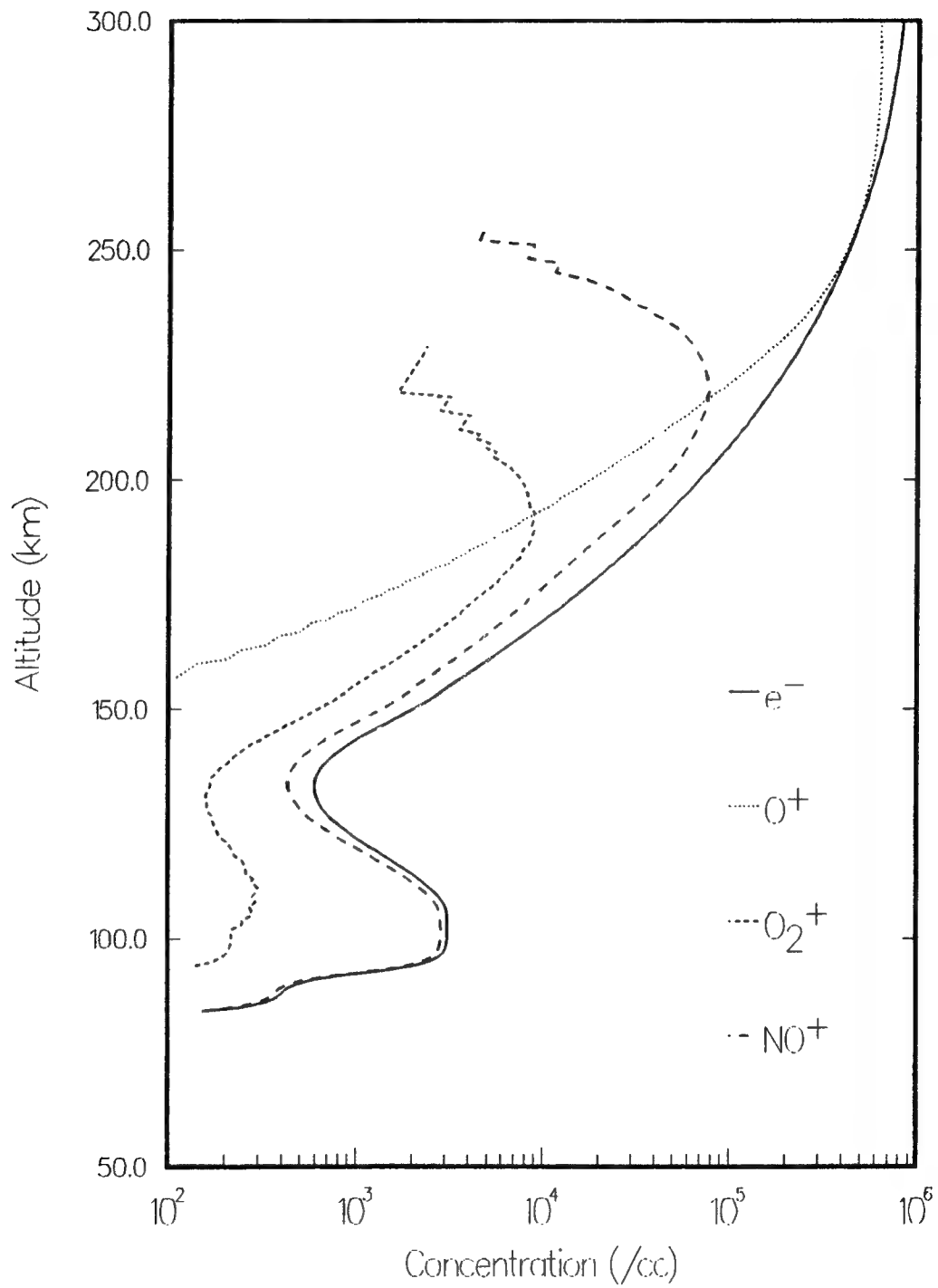


**Figure 18.** IRI ionosphere for local midnight & geomagnetic equator.

## Magnesium Model 2A

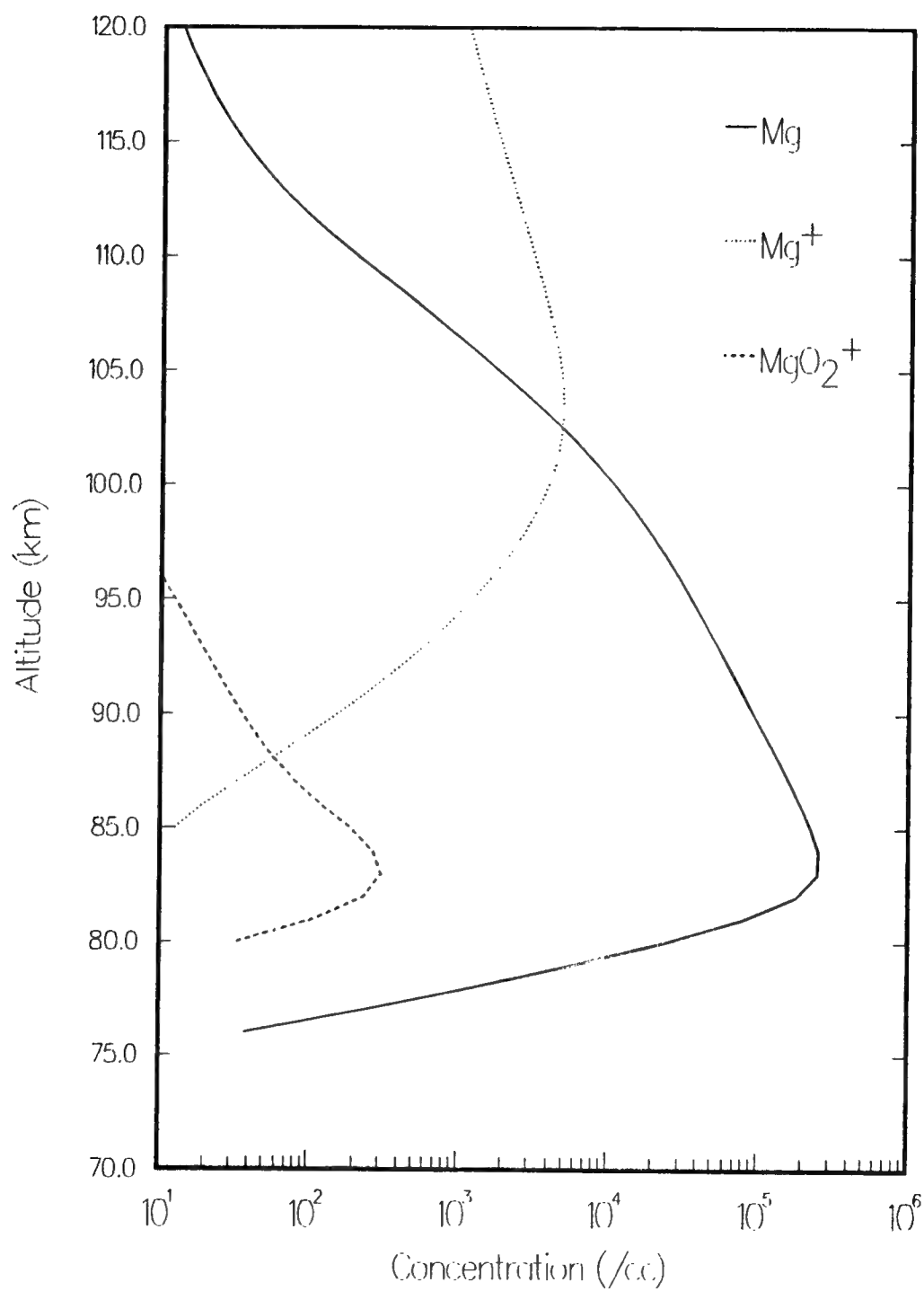


**Figure 19.** Daytime results for Mg<sup>+</sup> ion model 2a.

## Magnesium Model 2A

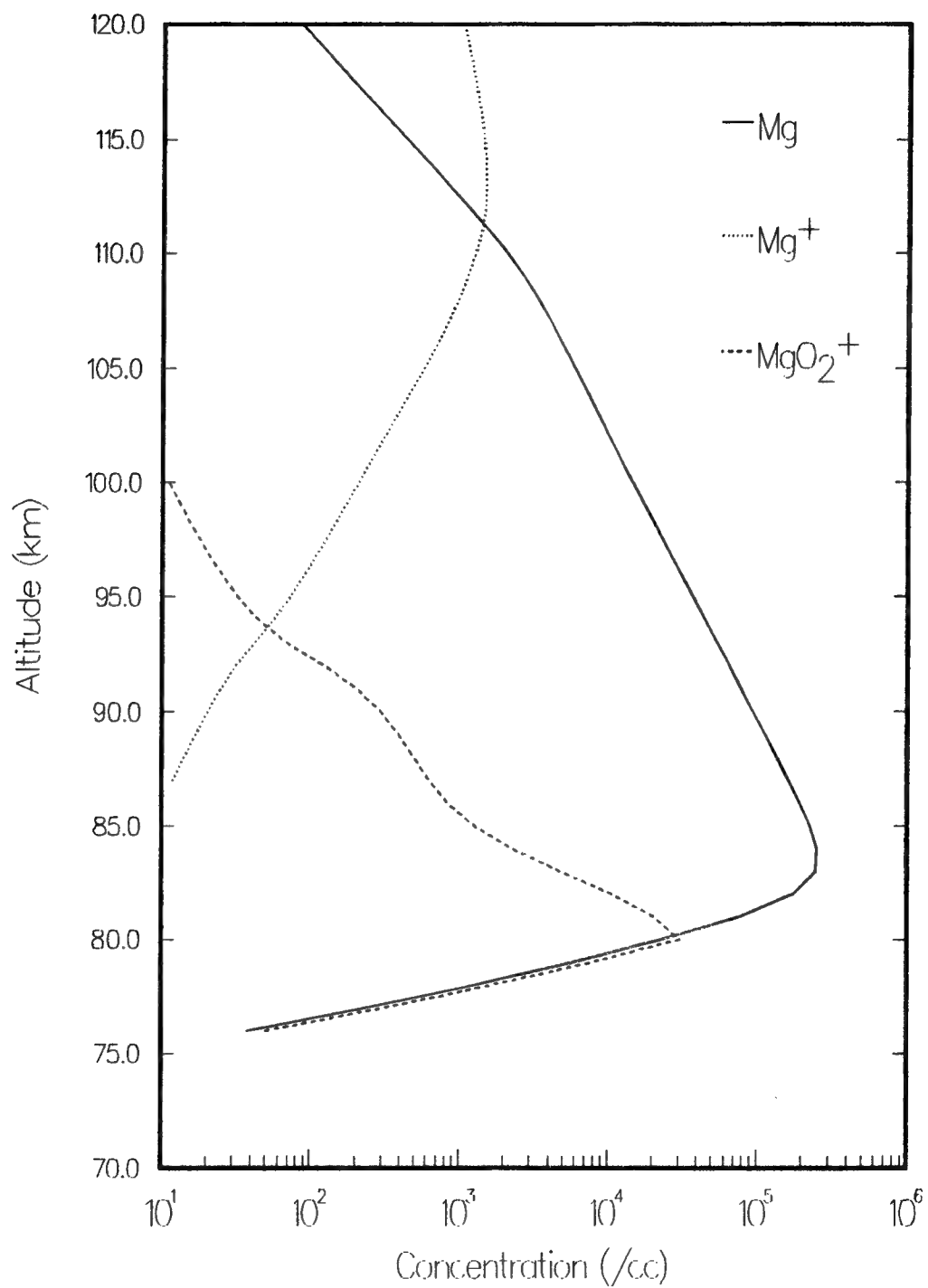


**Figure 20.** Nighttime results for  $Mg^+$  ion model 2a.



## Magnesium Model 2B

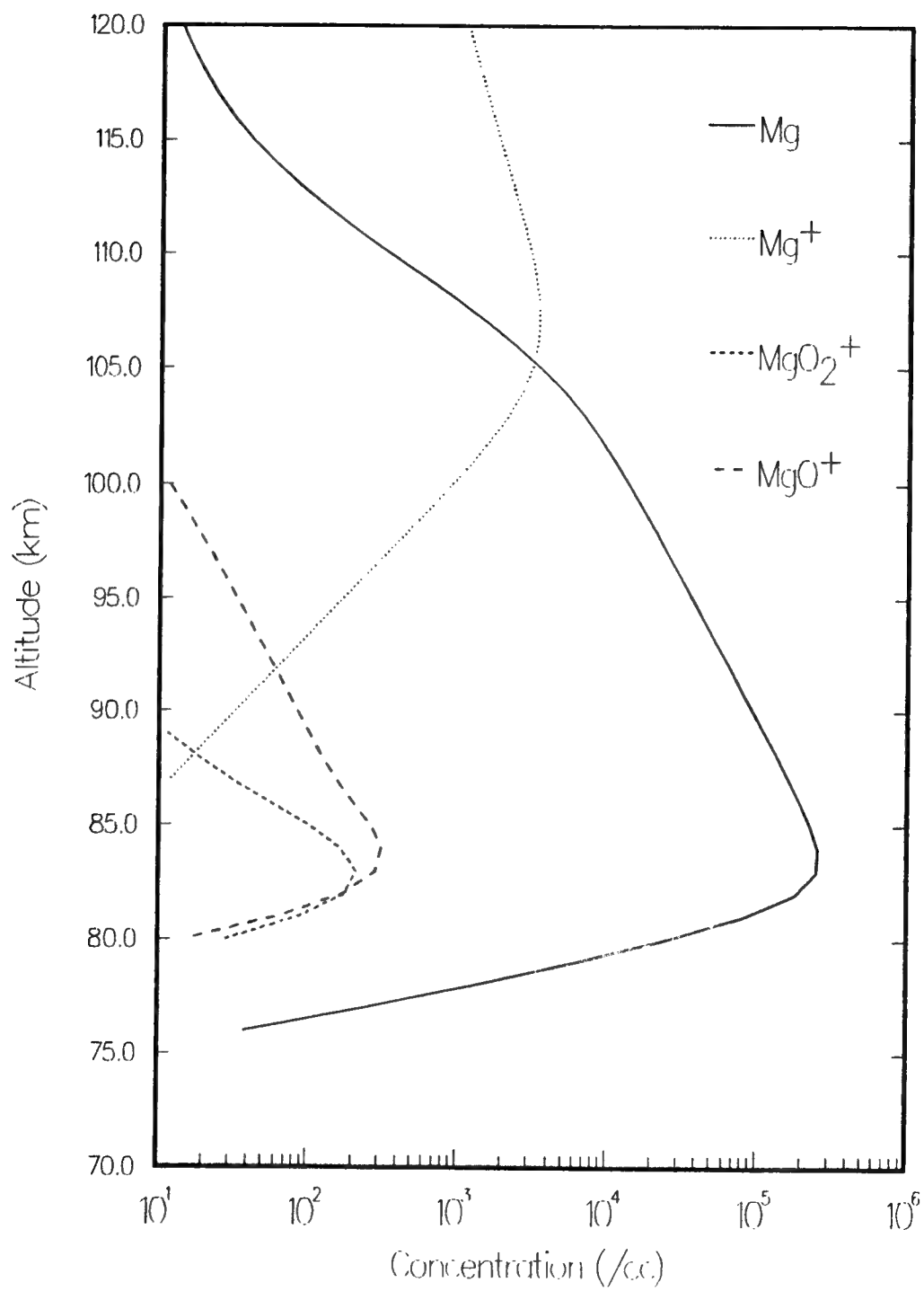
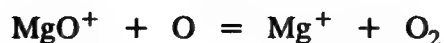


**Figure 21.** Daytime results for  $Mg^+$  ion model 2b.



*Swider* [1969] has estimated a rate constant of  $1(-10) \text{ cm}^3 \text{ sec}^{-1}$  for the first of these reactions. *Ferguson and Fehnsfeld* [1968] measured the same rate for the second. The reaction of  $\text{MgO}^+$  with atomic oxygen has recently been confirmed by *Rowe, et al.* [1981] and has been demonstrated with several other atmospheric species as well, including ozone, nitric oxide and carbon dioxide. From considerations of relative concentrations and rates, the reaction with atomic oxygen should be the most important of these. On the other hand, the reaction of  $\text{MgO}_2^+$  to form  $\text{MgO}^+$  is completely unconfirmed experimentally. These reactions are examined in Model 2C, the daytime profiles for which are shown in Figure 22. The change in the  $\text{Mg}^+$  with the addition of these two re-cycling reactions is dramatic. The peak density has risen by a factor of ten and the peak altitude has decreased to about 90 km.

It is instructive at this point to compare these results with measurements. Daytime ion mass spectrometer measurements [*e.g.* *Kopp and Herrmann*, 1983] show the metal ions in a rather broad layer from about 90 to 100 km. At this point, the absolute number of  $\text{Mg}^+$  ions is not essential, since we intend to normalize the profiles in the end. However, we note that measured peak values appear to vary greatly, from several hundred to a few thousand per  $\text{cm}^3$ . The column density of  $\text{Mg}^+$  has been reported to be from  $2(9) \text{ cm}^{-2}$  [*Aikin and Goldberg*, 1973] to as much as  $8(9) \text{ cm}^{-2}$  [*Gérard and Monfils*, 1978]. Unfortunately, corresponding measurements of the magnesium neutral layer have not been made due to the insusceptibility of neutral Mg to lidar.

Returning to Figure 22, we note that the  $\text{Mg}^+$  layer extends to altitudes of about 80 km, which is about 10 km lower than measurements would indicate. On the other hand, turning to Figure 21, we see that the  $\text{Mg}^+$  layer there is too high, again by about 10 km. The bottomside of the layer is also not sharp enough when compared to measured profiles. The biggest problem with Model 2C is that there is no efficient way to remove  $\text{Mg}^+$ . Therefore, there is a great deal of  $\text{Mg}^+$  at low altitudes. We propose that the re-cycling reaction of  $\text{MgO}_2^+$  with O does not take place. This has also been suggested by *Anderson and Barth* [1971]. Without this process, the reaction forming  $\text{MgO}_2^+$  becomes entirely a sink and the better part of the low altitude  $\text{Mg}^+$  is removed. Still, however, the peak is somewhat high. If we re-examine our choice for charge exchange rate coefficients, it is found that an in-depth evaluation [*Ferguson*, 1972] of the cross section measurements of *Rutherford, et al.* [1971] shows that the rate coefficient for charge exchange with  $\text{NO}^+$  obtained is  $1(-9) \text{ cm}^3 \text{ sec}^{-1}$ , which is a full order of magnitude larger than that used in Model 2A-C. Also, *Anderson and Barth* [1971] have proposed that the rate constant for this reaction should be as high as  $9(-9) \text{ cm}^3 \text{ sec}^{-1}$  in order to explain observed  $\text{Mg}^+/\text{Mg}$  ratios. We choose to use a value of  $1(-9) \text{ cm}^3 \text{ sec}^{-1}$  for the reaction. These two changes, eliminating recycling of  $\text{MgO}_2^+$  and increasing the rate coefficient for charge exchange with  $\text{NO}^+$  constitute Model 2D, the profiles for which are shown in Figure 23. The nighttime version is shown in Figure 24.

## Magnesium Model 2C

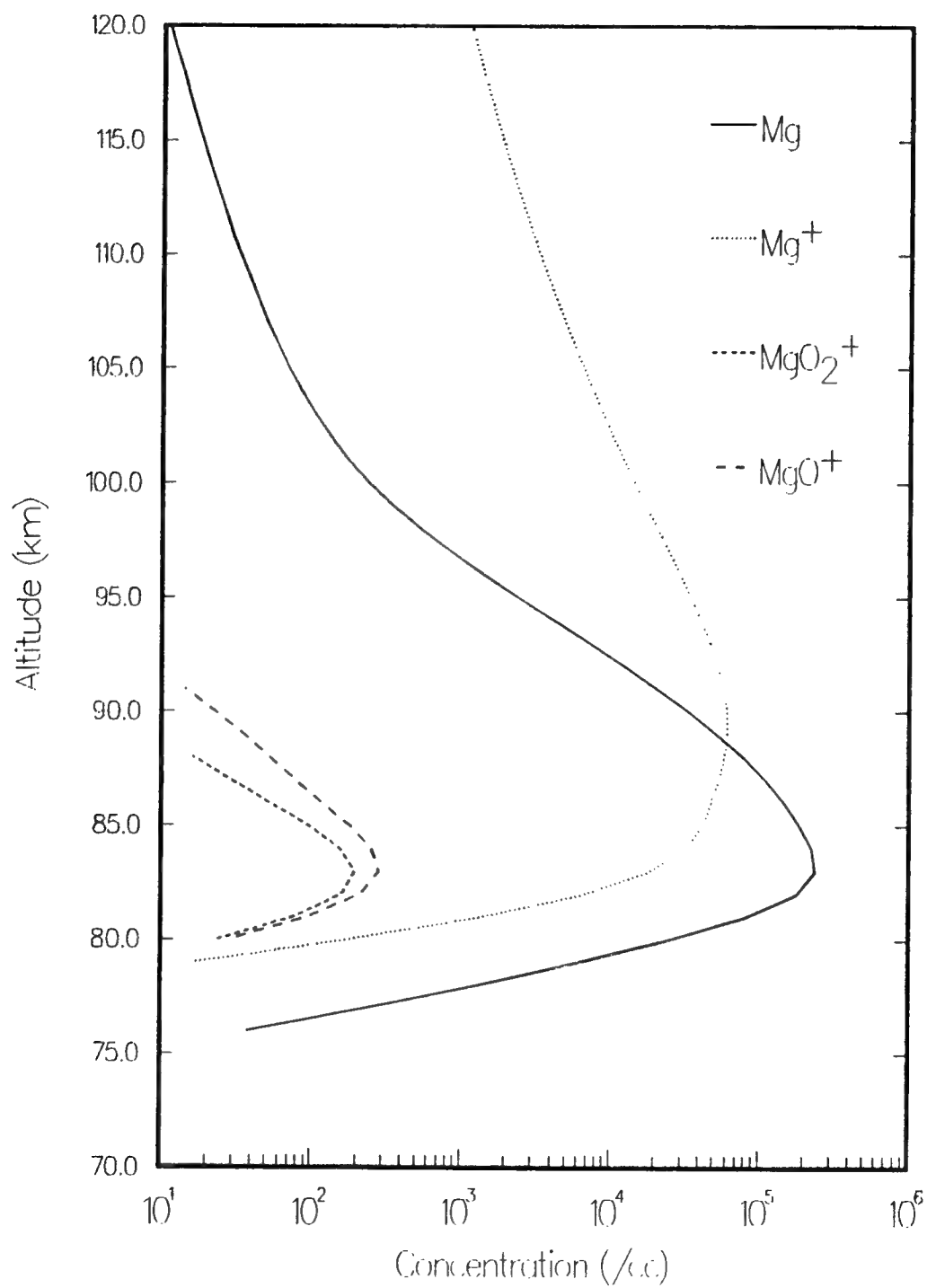


**Figure 22.** Daytime results for Mg<sup>+</sup> ion model 2c.

## Magnesium Model 2D

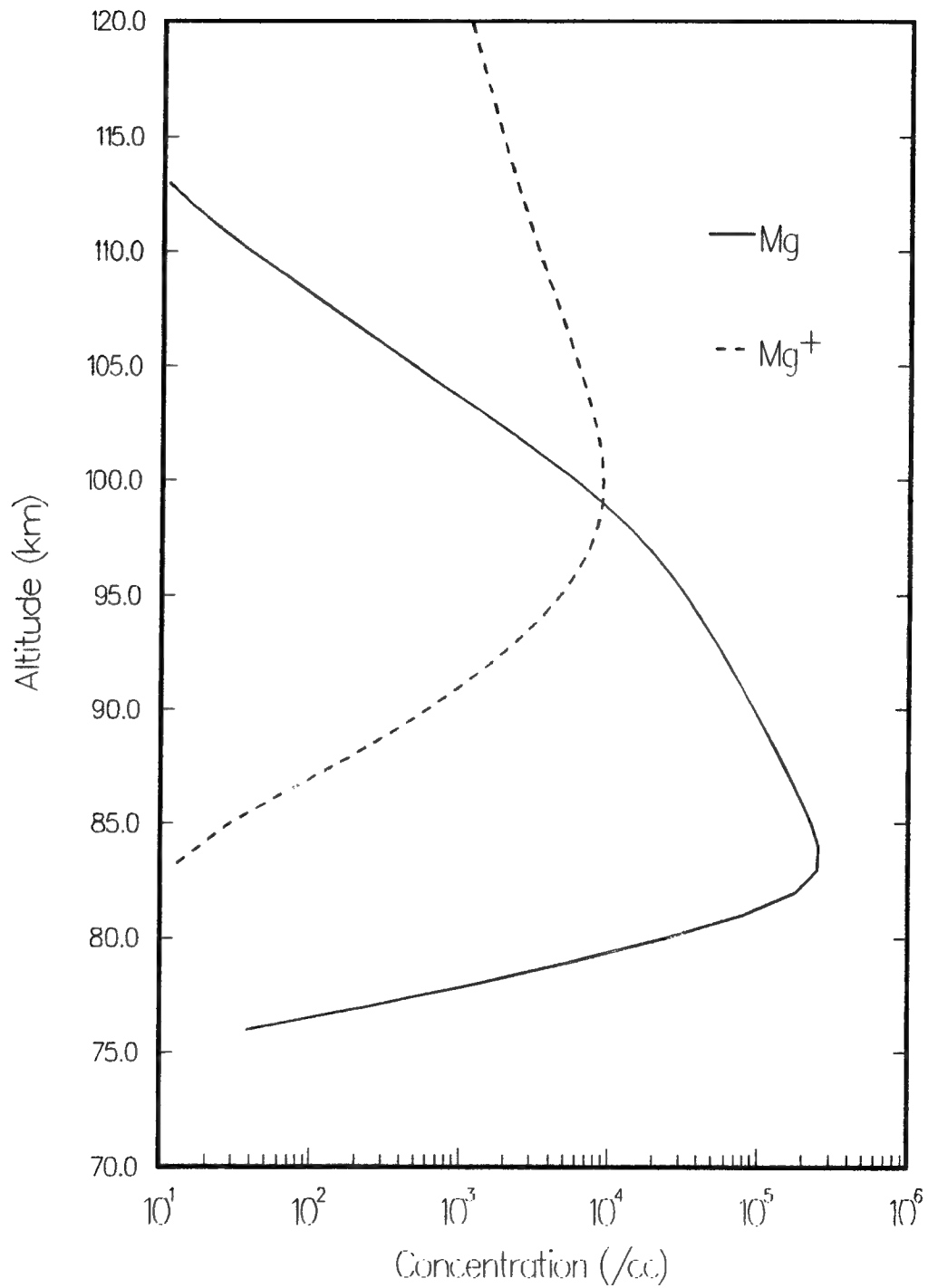


**Figure 23.** Daytime results for  $Mg^+$  ion model 2d.

## Magnesium Model 2D

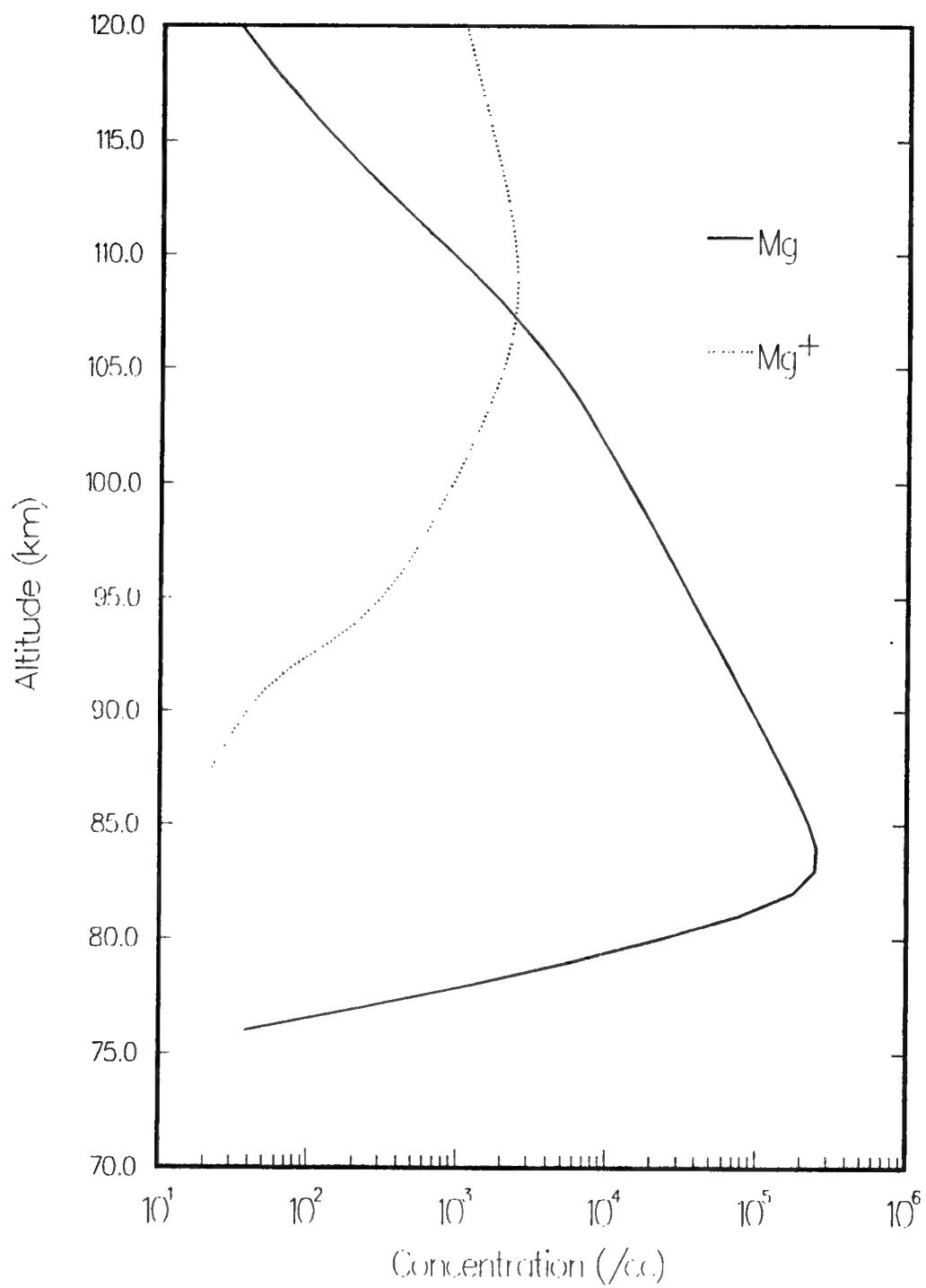


**Figure 24.** Nighttime results for Mg<sup>+</sup> ion model 2d.

For reference, we have tabulated the characteristics of all four ion models below. Noting that the peak densities are subject to scaling, the relative column densities and altitudes of the maxima are the important features.

**TABLE 2.** Characteristics of the Ion Models

Model	Peak Density	Peak Altitude	Column Density
2A	4,884	103	8(9)
2B	3,386	107	5(9)
2C	60,670	89	80(9)
2D	8,885	100	13(9)
	cm <sup>-3</sup>	km	cm <sup>-2</sup>

By increasing the rate coefficients for charge exchange even further, we could lower the peak altitude even more. The present state of Model 2D suffices for these models, however. In what follows, we will be most interested in what happens to the ions during transport to and from higher altitudes. We will find there that very little transport takes place from altitude below about 120 km. This being the case, we can see that the precise nature of the model below this altitude is relatively unimportant. What matters more is the amount of Mg<sup>+</sup> at 120 km and the scale height above this altitude. However, we see that the precise values adopted for charge exchange do impact the diurnal variations in the ion peak. In what follows, we will be interested in computing the total column density of Mg<sup>+</sup> along various lines of sight. For this, the densities below 120 km are important. Therefore, we will present results for both Models 2B and 2D, which differ only by the chosen magnitude for NO<sup>+</sup> and O<sup>+</sup> charge exchange rates. The true values for these rates are, as noted previously, somewhat speculative in any case. The complete kinetic model is given in Table 3.

In the next section, we will develop a time-dependent model for this system. This will be accomplished in a series of steps. First, we will make an approximate one-component neutral model from the results of the multi-component neutral model. Using this, we will solve the time dependent problem of deposition and removal of Mg. We will then add the ions, giving a two-component system. After examining the diurnal dependence, we will add a model for electric fields. The time-dependent solution is necessary for the incorporation of the electric fields. It is also valuable because it allows us to compare steady state and time dependent results, assessing the strengths and weaknesses of each.

**TABLE 3. Mg Ion Kinetic Model**

#	Reaction	Rate	Source
7	$\text{Mg} + h\nu = \text{Mg}^+$	4.0(-07)	<i>Swider [1969]</i>
8	$\text{Mg} + \text{O}_2^+ = \text{Mg}^+ + \text{O}_2$	1.0(-10)	<i>Aiken &amp; Goldberg [1973]</i>
9	$\text{Mg} + \text{NO}^+ = \text{Mg}^+ + \text{NO}$	1.0(-9,10)	<i>Ferguson [1972]</i>
10	$\text{Mg} + \text{O}^+ = \text{Mg}^+ + \text{O}$	1.0(-9,10)	<i>estimate</i>
11	$\text{Mg}^+ + e^- = \text{Mg} + h\nu$	4.0(-12)	<i>Swider [1969]</i>
12	$\text{Mg}^+ + \text{N}_2 + \text{O}_2 = \text{MgO}_2^+ + \text{N}_2$	2.5(-30)	<i>Ferguson &amp; Fehnsenfeld [1968]</i>
13	$\text{MgO}_2^+ + e^- = \text{Mg} + \text{O}_2$	3.0(-07)	<i>Swider [1969]</i>
14	$\text{Mg}^+ + \text{O}_3 = \text{MgO}^+ + \text{O}_2$	2.3(-10)	<i>Ferguson &amp; Fehnsenfeld [1968]</i>
15	$\text{MgO}^+ + e^- = \text{Mg} + \text{O}$	1.0(-07)	<i>Swider [1969]</i>
16	$\text{MgO}^+ + \text{O} = \text{Mg}^+ + \text{O}_2$	1.0(-10)	<i>Rowe, et al. [1981]</i>

## 4. THE TIME DEPENDENT MODELS

In this section, we explore the time dependence of magnesium neutrals and ions. The primary difference between these and the models in Section 2 is that the steady state models represented chemistry that had reached equilibrium conditions. Although we were able to represent day and night by choosing different models of the ionosphere, these models gave no information on the attainment of the equilibrium state. Also, diffusion was not coupled with chemistry. Rather, diffusion was introduced to calculate a profile of the hypothetical species MgX which represented the total concentration of all species containing the metal. A final limitation of the steady state models is that it not possible to introduce external forces which move ions or neutrals. For this we must turn to fully time dependent modeling.

### 4.1 THE ONE COMPONENT MODEL

We have seen in Section 3 that the neutrals and ions form separate layers, with neutral species primarily below about 90 km and ions primarily above. Thus, it makes some sense to begin the investigation of time dependent models by looking at a one-component model consisting only of

neutral Mg. The model will not be correct above 90 km. However, the behavior below 90 km will be uncoupled from the behavior of the ions. Ions are created mainly above this altitude and are, for the most part, destroyed before diffusing down below this altitude.

To begin, we need to create a one-component kinetic model based on the neutral chemistry given in Table 1. At each altitude, the creation of Mg is given by  $q(h)$ , or something proportional to it at least. For the destruction rate, we note that Mg is changed to  $MgO_2$  by reaction 1 and to  $MgO$  by reaction 4. Further, we note that  $MgO_2$  is changed to  $MgO$  by reaction 2, albeit at a relatively slow rate. The rate of this transformation will not matter, since the purpose is to represent the destruction of Mg only. Next, we note that  $MgO$  is transformed into  $MgCO_3$  through the reaction with atomic oxygen. Although it was necessary in the steady state model to introduce a "closure" reaction transforming  $MgCO_3$  back to Mg, since otherwise we would have had completely  $MgCO_3$  at all altitudes, it is likely that the rate of this reaction is so slow that it does not appreciably effect the Mg concentration. Therefore, we assume that once reaction 1 or reaction 4 has taken place, the Mg is gone for good. We must make one exception to this. Reaction 3 also regenerates Mg directly from  $MgO$ . The rate for this reaction is not slow. This is included by assuming that only a fraction of the  $MgO$  goes on to become  $MgCO_3$ . The rest is recycled into Mg. The fraction, or branching ratio, depends on the relative rates of the two reactions (R.3) and (R.4) and is thus altitude dependent. The expression for the altitude dependent destruction rate of Mg based on these assumptions is

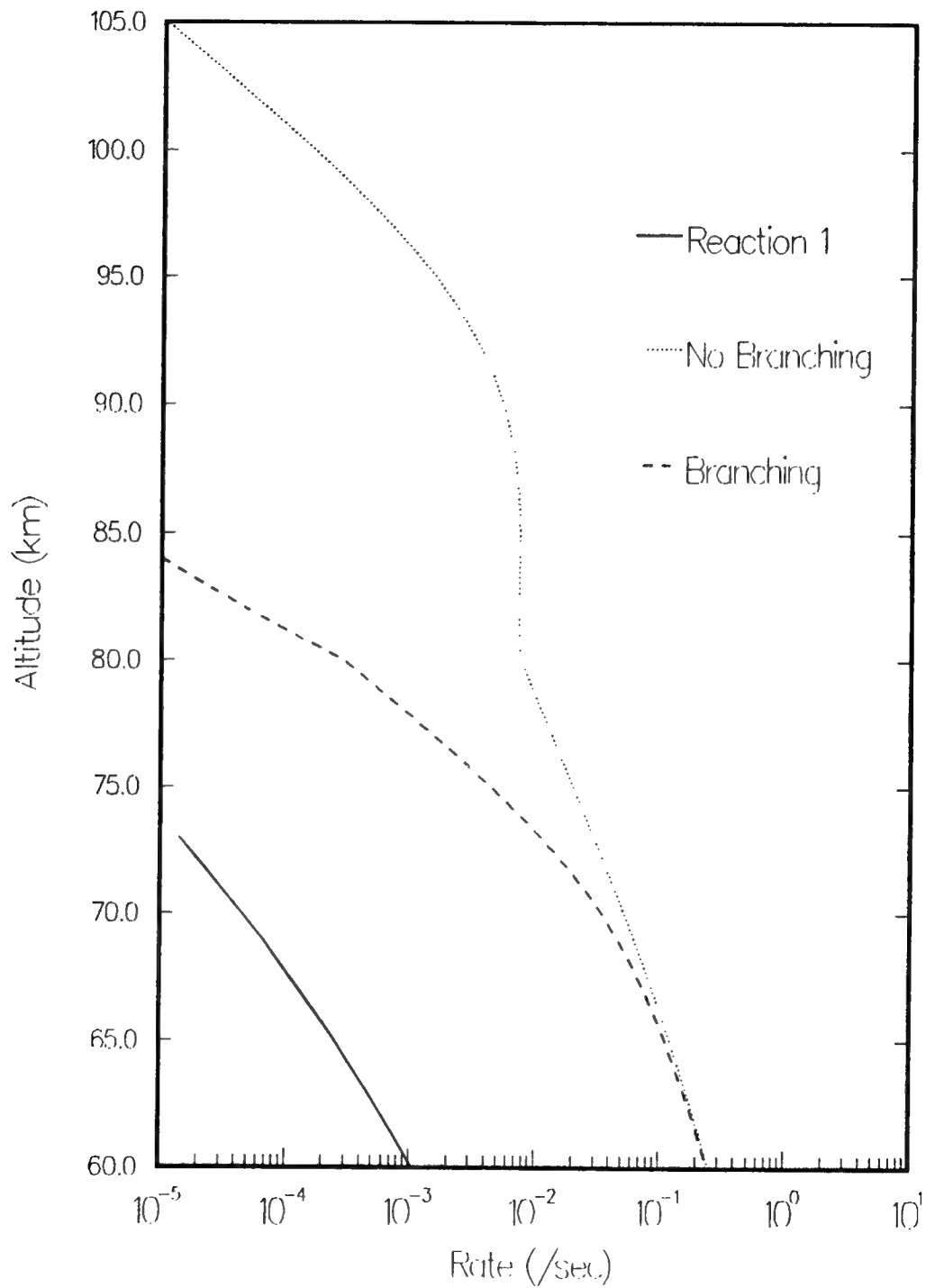
$$r_d = k_1 [O_2][N_2] + k_4 [O_3] \frac{k_5 [CO_2][N_2]}{k_5 [CO_2][N_2] + k_3 [O]} \quad (8)$$

Figure 25 shows the destruction rate as a function of altitude. Also plotted there are the destruction by reaction 1 alone and the destruction rate in the absence of branching through reaction 3. Figure 25 shows two important features. First, the destruction by reaction 1 is insignificant when compared to destruction through reaction with ozone. Second, we see that the rate including branching is significantly less than that with branching excluded, especially at high altitudes. Furthermore, it is significantly different below 80 km, where as noted before, the atomic oxygen density falls off dramatically at night. In order to include this effect, we will define a daytime and a nighttime destruction rate. The first of these will use a daytime profile where atomic oxygen is set to  $1(10) \text{ cm}^{-3}$  below 80 km and the second will use a nighttime profile for atomic oxygen where, below 80 km, O falls off exponentially with a scale height of 1 km. This is somewhat artificial, but it reproduces quite well the modeling results of Allen, *et al.* [1984] for day to night variation of atomic oxygen. The model used here approximates the day to night behavior of oxygen adequately for our purposes. Figure 26 shows the day and night destruction rates of Mg used in the time dependent model.

Turning to the solution of the diffusion portion of the problem, the atomic Mg profile is represented on a grid with spacing of 1 km. At each step and at each altitude, the time derivative of the density of Mg is given by two terms, one representing the kinetics and the second the diffusion. The kinetic portion is comprised of the source term  $q(h_i)$  and the sink term



## Mg One Component Destruction Rate



Radex, Inc. 15-SEP-94 14:25:04

**Figure 25. Daytime one-component model Mg destruction rates.**

## Day and Night Mg Destruction Rates

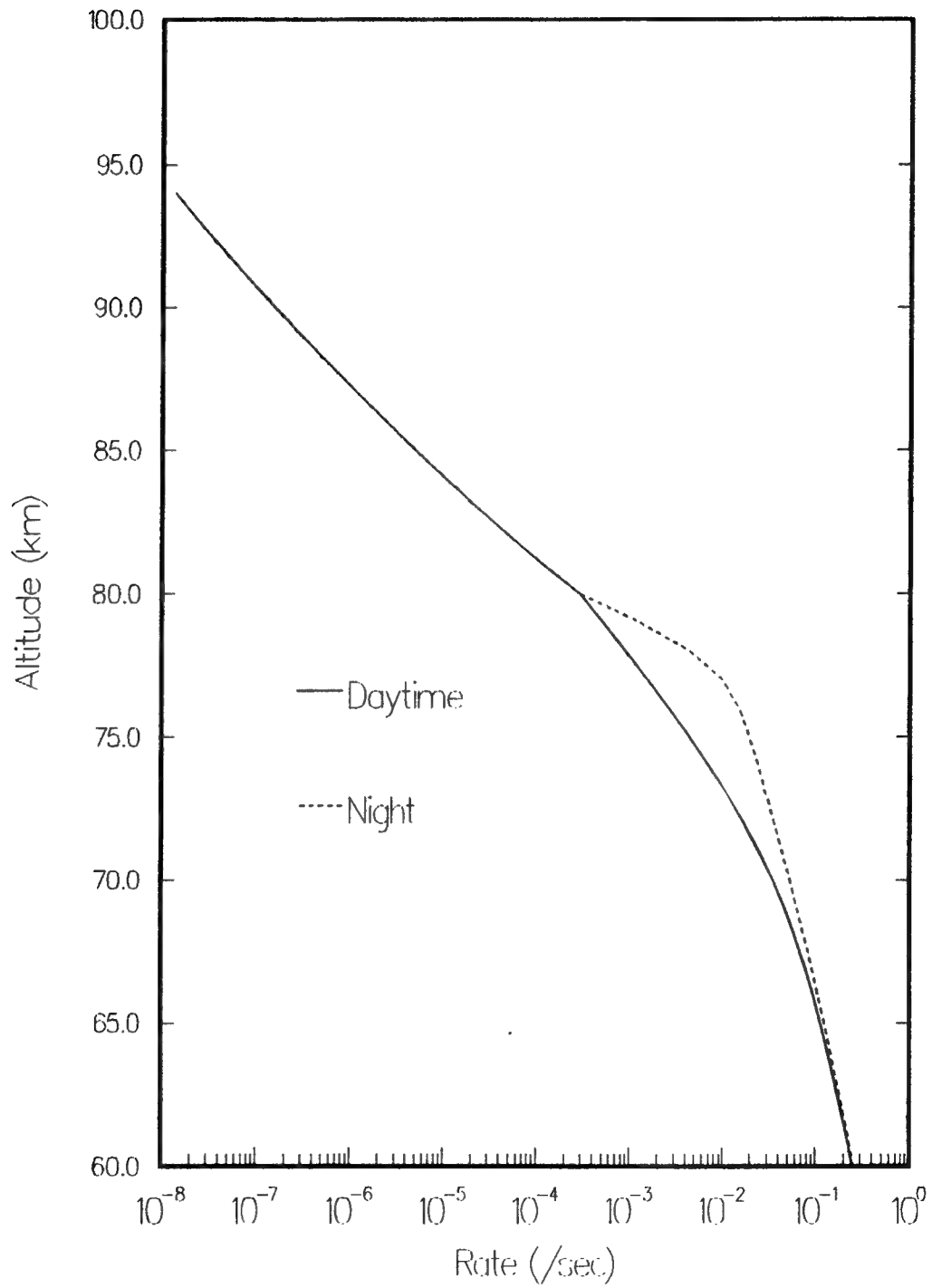


**Figure 26.** Day and night Mg destruction rates.

$r_d(h_i)$ . The diffusion portion [Banks and Kockarts, 1973] is spacial derivative of the flux, given in Eq(3).

$$\frac{\partial n_1}{\partial t} = q - r_d n_1 - \frac{\partial}{\partial z} (n_1 w) \quad (9)$$

We solve Eq(9) by first calculating  $n_1 w$  at each grid point then forming the finite difference term

$$\frac{\partial}{\partial z} (n_1 w) \equiv \frac{(n_1 w)_{i+1} - (n_1 w)_{i-1}}{\Delta x} \quad (10)$$

With this, Eq(9) is used to march ahead in time. There is one further complication in our formulation. Using Eq(9) and Eq(10) implicitly requires very small timesteps to maintain stability. We find that the same result can be obtained using steps of one second if we first step ahead one second using only the kinetics, *i.e.*,

$$\hat{n}_{i+1}(h_j) = n_i(h_j) + D_k(r_c(h_j), q(h_j)) \Delta t \quad (11)$$

then follow this with a step for the diffusion, *i.e.*,

$$n_{i+1}(h_j) = \hat{n}_{i+1}(h_j) + D_d(\hat{n}_{i+1}(h_{j-1}), \hat{n}_{i+1}(h_{j+1}), D_{12}, K, H_1, H) \Delta t \quad (12)$$

where  $D_k$  represents the kinetic portions of Eq(9) and  $D_d$  the diffusion portions. In practice, we use a fourth order Runge-Kutta integration scheme. Eq(11) and Eq(12) have been written instead as simple finite differences for simplicity.

All other quantities needed for solving Eq(9) have already been given. We need only boundary conditions to continue. Assuming that the depletion of Mg is sufficient at 60 km to remove all of the Mg at this altitude leads to the lower boundary condition of  $Mg_{60} = 0$ . From Figure 25, the lifetime of an Mg atom at 60 km is around 4 seconds, so it seems a valid assumption to take the density at zero. This is also equivalent to assuming kinetic control of the system at the lower boundary. We take the upper boundary at 350 km. There, we assume that the system is entirely under the control of diffusion and that a steady state situation exists. Then, the density at 350 km is related to that in the next bin down by

$$Mg_{350} = Mg_{349} e^{-\frac{1}{H_1}} \quad (13)$$

To implement this, we set  $Mg_{350}$  at the beginning of each timestep according to the latest value of  $Mg_{349}$ . We perform the first simulation using full strength deposition and set the maximum of the eddy diffusion coefficient at 100 km. We begin the simulation with no Mg at all at any

altitude. In this sort of problem, one can never say for certain that the final result does not depend on the initial choice for a profile. However, we have found the result to be insensitive and running the simulations for a timespan of about two weeks gives a stable result.

The resulting Mg profile is shown in Figure 27. The peak value is about  $290,000 \text{ cm}^{-3}$  at an altitude of 86 km, which compares to a peak value of  $250,000 \text{ cm}^{-3}$  at an altitude of 84 km for the steady state model in Figure 15. This difference is remarkable but not altogether unexpected. The steady state model neglects the time it takes for Mg to diffuse from approximately 75 km where it is deposited to the 85 km, where it becomes the dominant species. If Mg is lost in this time period, it will not be reflected in the steady state model.

We can also see from Figure 27 that the change in the removal rate from night to day does not greatly change the overall profile, except in a region between 70 and 80 km. The peak density remains the same as does the density at all heights above the peak. Also, the fact that there is virtually no Mg until about 70 km argues for the validity of assuming that there is also none at 60 km. Referring to Figure 7, we recall that the steady state diffusion solution jumped up immediately from its lower boundary value when this value is small. The long time limit of the time dependent solution, on the other hand, remains small until the kinetics allows for some Mg to form. Assuming that the kinetic model for removal is reasonable, the lower boundary condition is also reasonable.

We can take advantage of the relative simplicity of this system to perform another parametric study. We should investigate the prior decision to shut off ablation above 140 km. *Love and Brownlee* [1990] have recently performed computations of the entry behavior of meteoric particles which include temperature effects. Although their results are limited to micrometeoroid particles and, even then, do not lend themselves easily to the determination of a cutoff altitude for ablation, they do conclude that "it is better to assume that evaporation does not begin at some well-defined temperature". We believe it suffices for the present to investigate the end result of variation in the upper cutoff, although the problem is an interesting one for further investigation. Figure 28 shows the result of reducing  $q_{\text{max}}$  to 100 km. Below 100 km, the reduction in Mg is negligible. Above, there is a mild reduction of about 20% in the Mg density. We will leave  $q_{\text{max}}$  set to 140 km for the remainder of this study.

#### 4.2 THE TWO COMPONENT MODEL

In this section, we will create a two component model, consisting of Mg and  $\text{Mg}^+$ , analogous to the one component model described previously. To do so, we must make an approximate kinetic model that describes the generation of  $\text{Mg}^+$  from Mg and the regeneration of Mg from  $\text{Mg}^+$ . We will assume that there is no absolute sink for  $\text{Mg}^+$  but that its fate is only to be recycled to atomic form. It is possible that ions such as  $\text{MgO}^+$  could form clusters. However, it seems likely that these clusters would once again become separated through molecular dissociative recombination to form atomic or molecular neutrals. Should they form atoms, the result of the model used here would not change. However, the formation of a cluster followed

## Mg One-Component Model Results

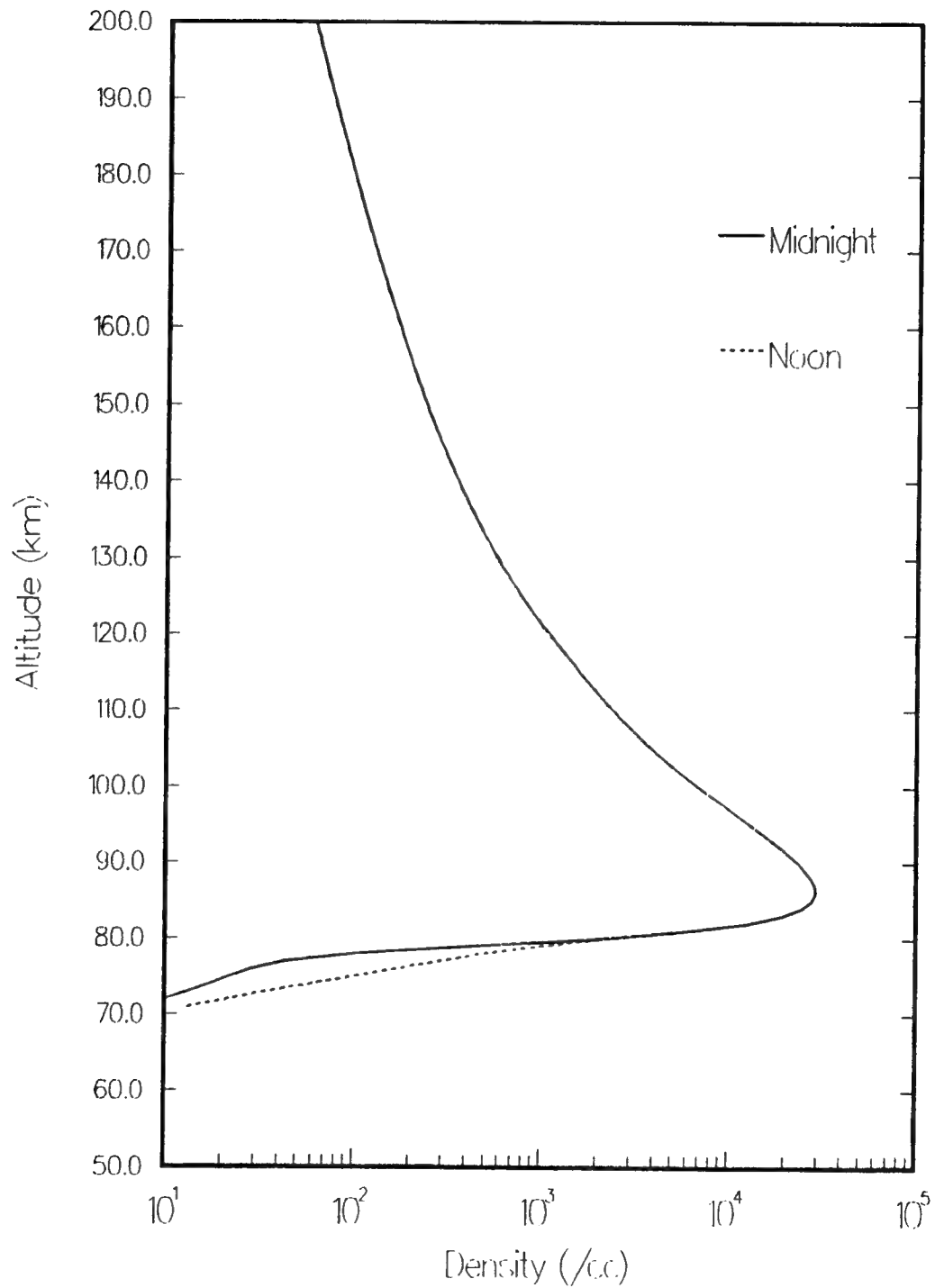


**Figure 27.** Day and night solutions for Mg atom in the one-component model.

Mg variation w/  $q_{\text{max}}$

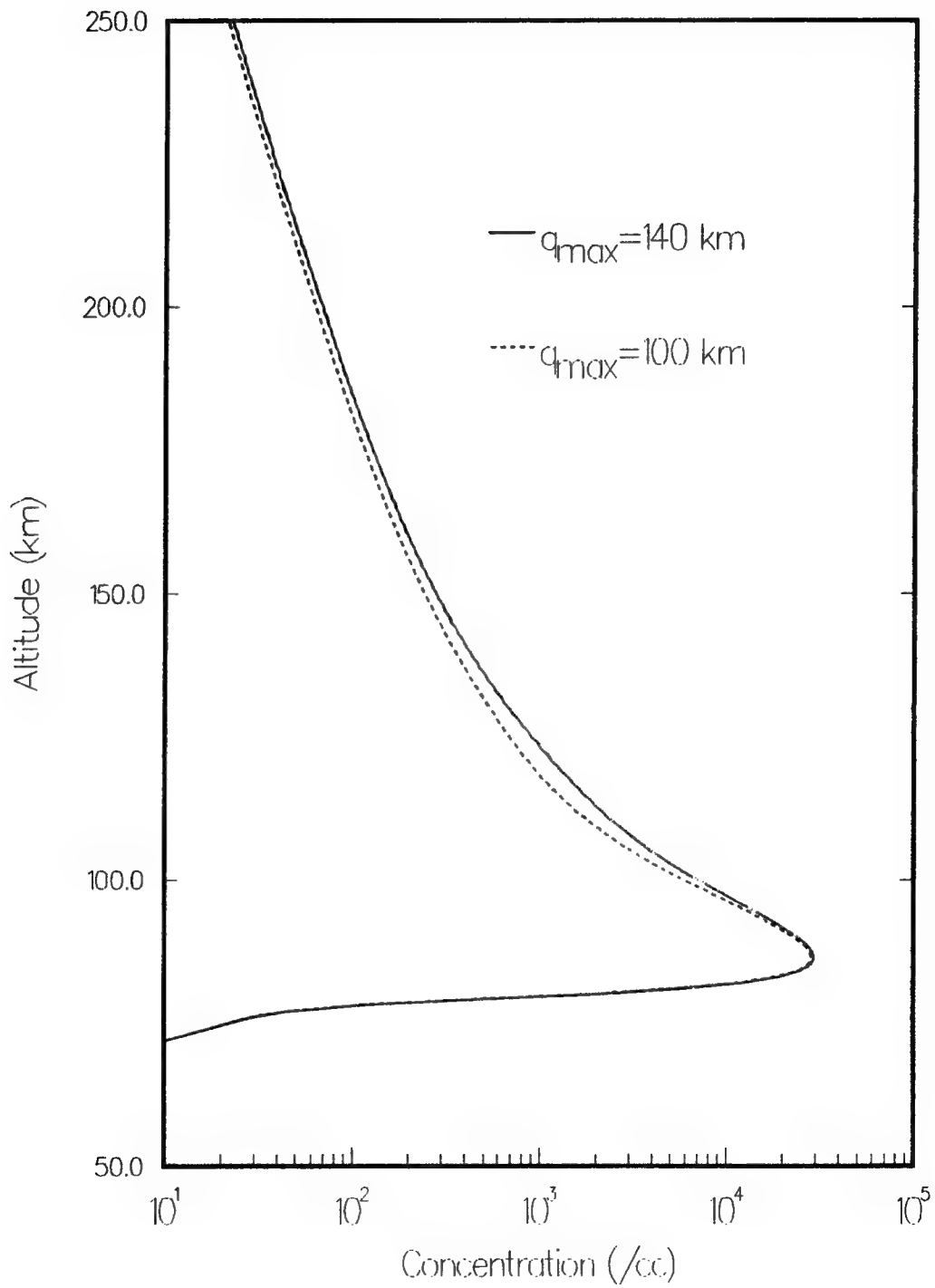


**Figure 28.** Test of the sensitivity of Mg to ablation cutoff altitude.

by the production of some neutral molecule which was not transformed back to atomic Mg would constitute an absolute sink for the  $\text{Mg}^+$  ion. We neglect this possibility.

To get to a two component model from the multicomponent ion chemistry in Table 3 we note first that  $\text{Mg}^+$  is created only through photoionization (in the daytime) or through charge exchange. The rate  $r_c$  for  $\text{Mg}^+$  production is then quite simply given by

$$r_c = r_7 + r_8[\text{O}_2^+] + r_9[\text{NO}^+] + r_{10}[\text{O}^+] \quad (14)$$

According to our kinetic model, the formation of  $\text{MgO}_2^+$  is followed by destruction through MDR and is therefore a complete sink. The formation of  $\text{MgO}^+$  on the other hand, can be followed by MDR to give the neutral or by a reaction with O to give back the ion. As before, this rate should be multiplied by the branching ratio. The radiative recombination reaction is a complete sink as well. The rate expression for the neutralization of  $\text{Mg}^+$  is then

$$r_n = k_{11}[e^-] + k_{12}[\text{N}_2][\text{O}_2] + k_{14}[\text{O}_3] \frac{k_{15}[e^-]}{k_{15}[e^-] + k_{16}[\text{O}]} \quad (15)$$

In fact, it turns out that the first and third terms in Eq(15) are virtually negligible at altitudes above 80 km, where the ions are found. The three-body reaction is the dominant form of  $\text{Mg}^+$  neutralization above 80 km. The daytime and nighttime curves for creation and destruction are shown in Figures 29 and 30. Also shown for reference in those figures is the destruction rate of neutral Mg,  $r_d$ . Below about 100 km, destruction overwhelms production of the ion. The creation and neutralization curves meet at about 100 km in the daytime and at about 110 km at night. This corresponds to the peaks in the ion profiles in Figures 19 and 20. Above about 140 km, the three-body reaction is no longer prevalent and the kinetics are controlled by charge exchange and by radiative recombination alone. In this case, the curves are parallel since both creation and neutralization of Mg are proportional to the ionospheric density. In this case, we see from the rate coefficients that the kinetic steady state ratio of  $\text{Mg}^+$  to Mg would be 250, which derives from the magnitude of  $k_{10}/k_{11}$ . We will examine this ratio in what is to come.

The two component time dependent model is solved in the same way as the one component one, with appropriate modifications for the chemistry between the atomic neutral  $n_1$  and the atomic ion  $n_2$ . The equations are

$$\frac{\partial n_1}{\partial t} = q - r_d n_1 - r_c n_1 + r_n n_2 - \frac{\partial}{\partial z}(n_1 w) \quad (16)$$

and

## Two Component Model Daytime Rates

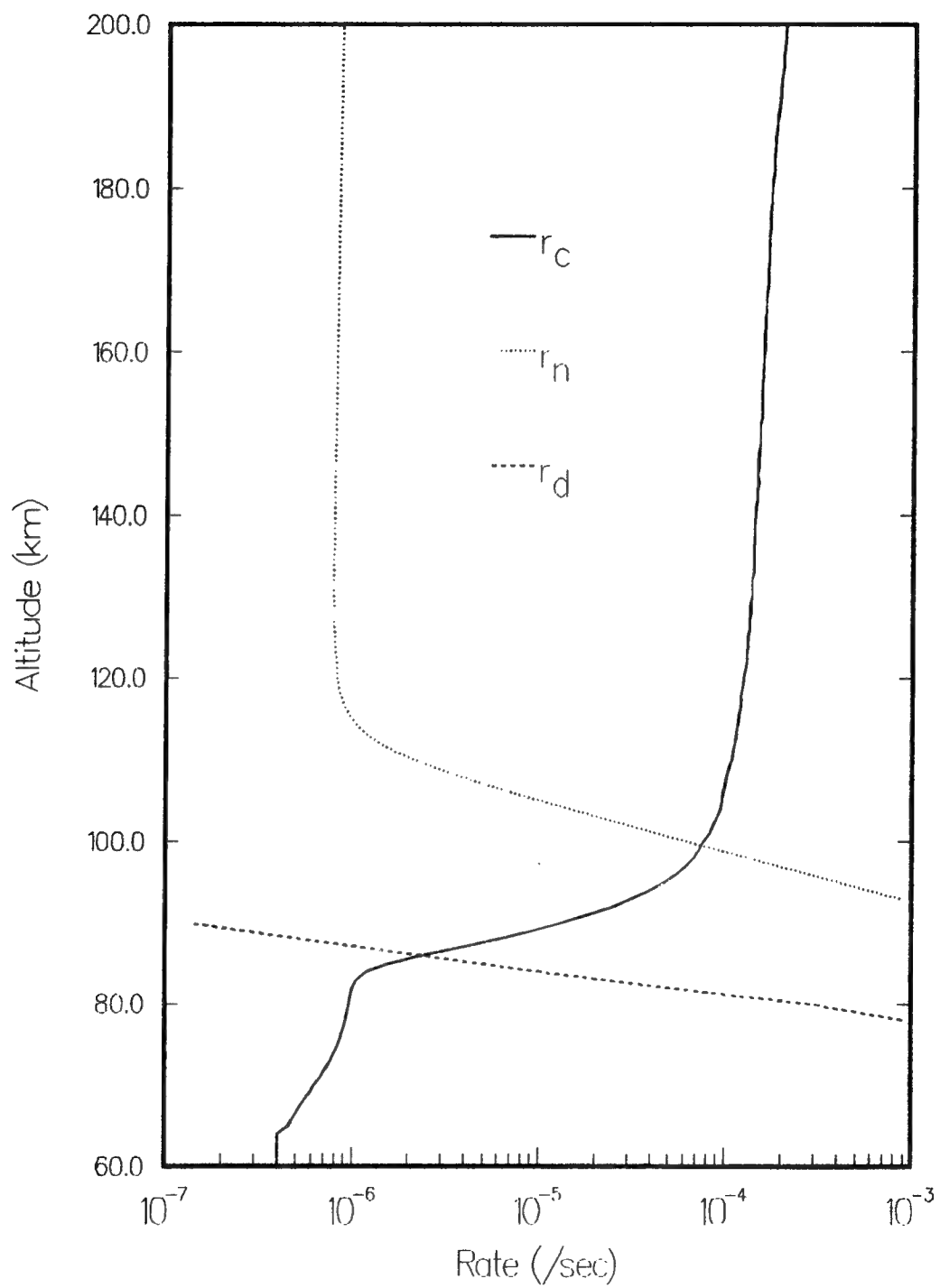


**Figure 29.** Daytime rates for the Two Component Model.



## Two Component Model Nighttime Rates

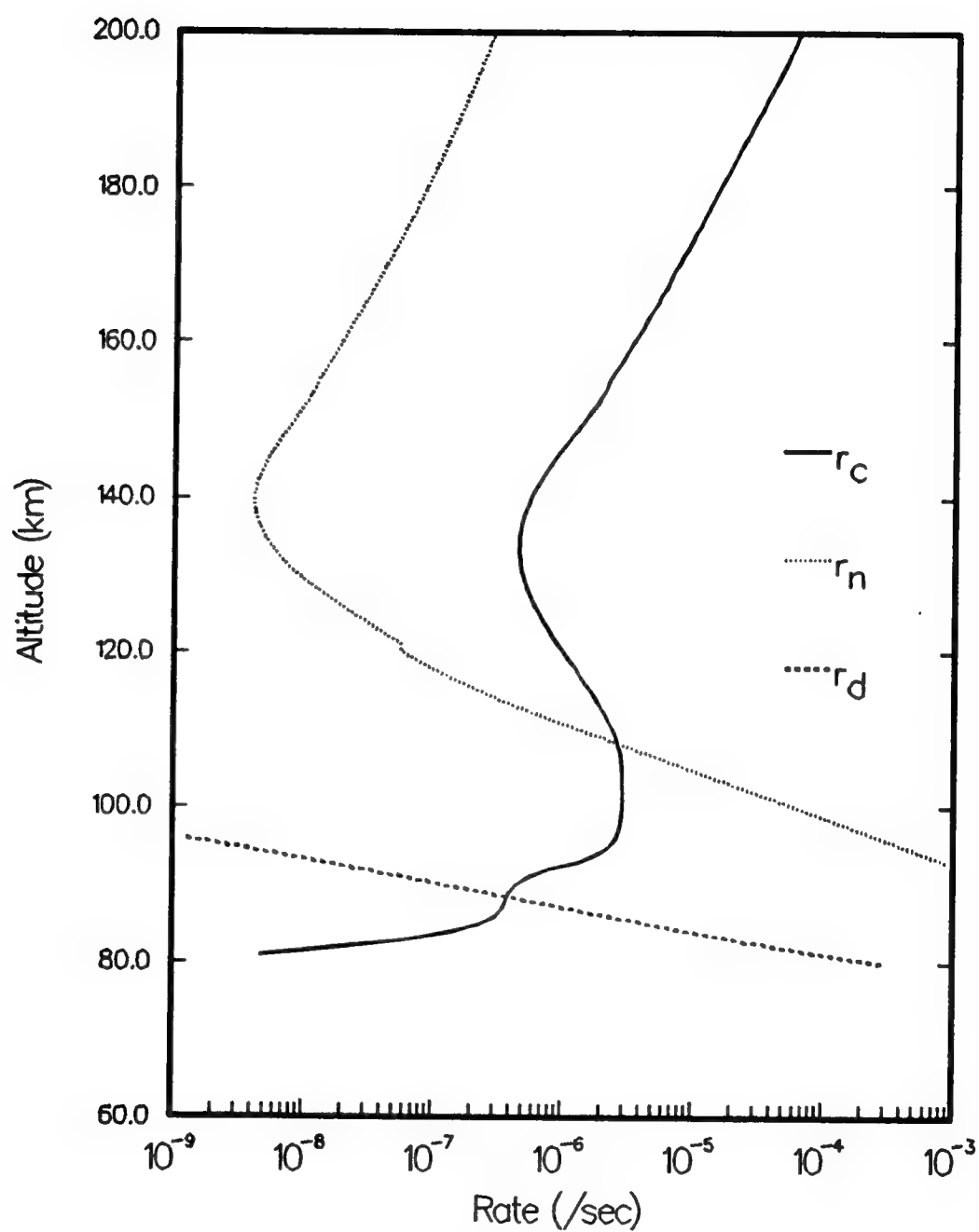


**Figure 30.** Nighttime rates for the Two Component Model.

$$\frac{\partial n_2}{\partial t} = r_c n_1 - r_n n_2 - \frac{\partial}{\partial z}(n_2 w) \quad (17)$$

In these calculations the same diffusion coefficients  $D_{12}$  and  $K$  were used for ions and neutrals. In fact, the diffusion coefficient for an ion is somewhat different from that for a neutral [Banks and Kockarts, 1973]. However, in our region of interest, the difference is no more than a factor of two or so and we have ignored the complication. We will, however, treat ion/ion and ion/neutral collisions more precisely in the context of calculation of the transport velocities arising from electric fields.

Solving the two component model including only chemistry and diffusion gives profiles for  $Mg^+$  like those shown in Figure 31. Presented there are the noon and midnight solutions. The noon solution shows a peak at about 100 km of some 4,000 /cm<sup>3</sup>. This drops to about 1,000 /cm<sup>3</sup> at night, when the peak also rises to about 110 km altitude. As mentioned previously, these numbers are probably somewhat too high. Typical daytime maxima are closer to perhaps 1,000 /cm<sup>3</sup>. However, the altitude predictions of the model seem to be in good agreement. Above about 120 km, we see no difference between day and night solutions. It is clear from this behavior that the behavior of  $Mg^+$  is dominated by chemistry and, as noted, there is not a great deal of difference between day and night chemistry at high altitude.

The ratio  $Mg^+/Mg$  is shown in Figure 32. Below about 100 km, there is no  $Mg^+$ .  $Mg^+$  dominates completely above 150 km as predicted by the examination of the creation and destruction rate coefficients. A typical value for the ratio is around 200 above 150 km. In Figure 33 we examine the diurnal dependence of the  $Mg^+$  column density. We see that there is a sharp increase at sunrise and a rapid attainment of a steady state by noon. After sunset, there is a corresponding drop but a more gradual decrease over the course of the night. The daytime replenishment through charge exchange is therefore seen to be more efficient than the nighttime depletion through  $MgO_2^+$  formation. Going back to the measured column densities of  $Mg^+$  quoted in 3.2 we see that we are perhaps two or three times larger than the minimum reported density of 2(9) /cm<sup>2</sup>. With reported column densities as high as 9(9) /cm<sup>2</sup>, however, these results do not seem far off. Again, we can scale the result by lowering the deposition rate  $q(h)$  by a constant. We will hold off on this, however, until we compare with GLO results.

Returning to the GLO results summarized in the introduction, we can imagine that the results of the steady state model at this point would not mimic those measurements well. This is primarily because Figure 31 predicts virtually a constant density of  $Mg^+$  above about 120 km altitude while the GLO results indicate a strong diurnal dependent at high tangent altitudes. To take a closer look at the model at this point, we show in Figure 34 a contour plot of the diurnal behavior. As can be seen, the model predicts a virtually constant  $Mg^+$  density above 125 km. We believe that electric fields are a major contributor to the motion and hence the variability of metal ions above the stratosphere. These are introduced into the model next.

## Mg<sup>+</sup> Time Dependent Profiles

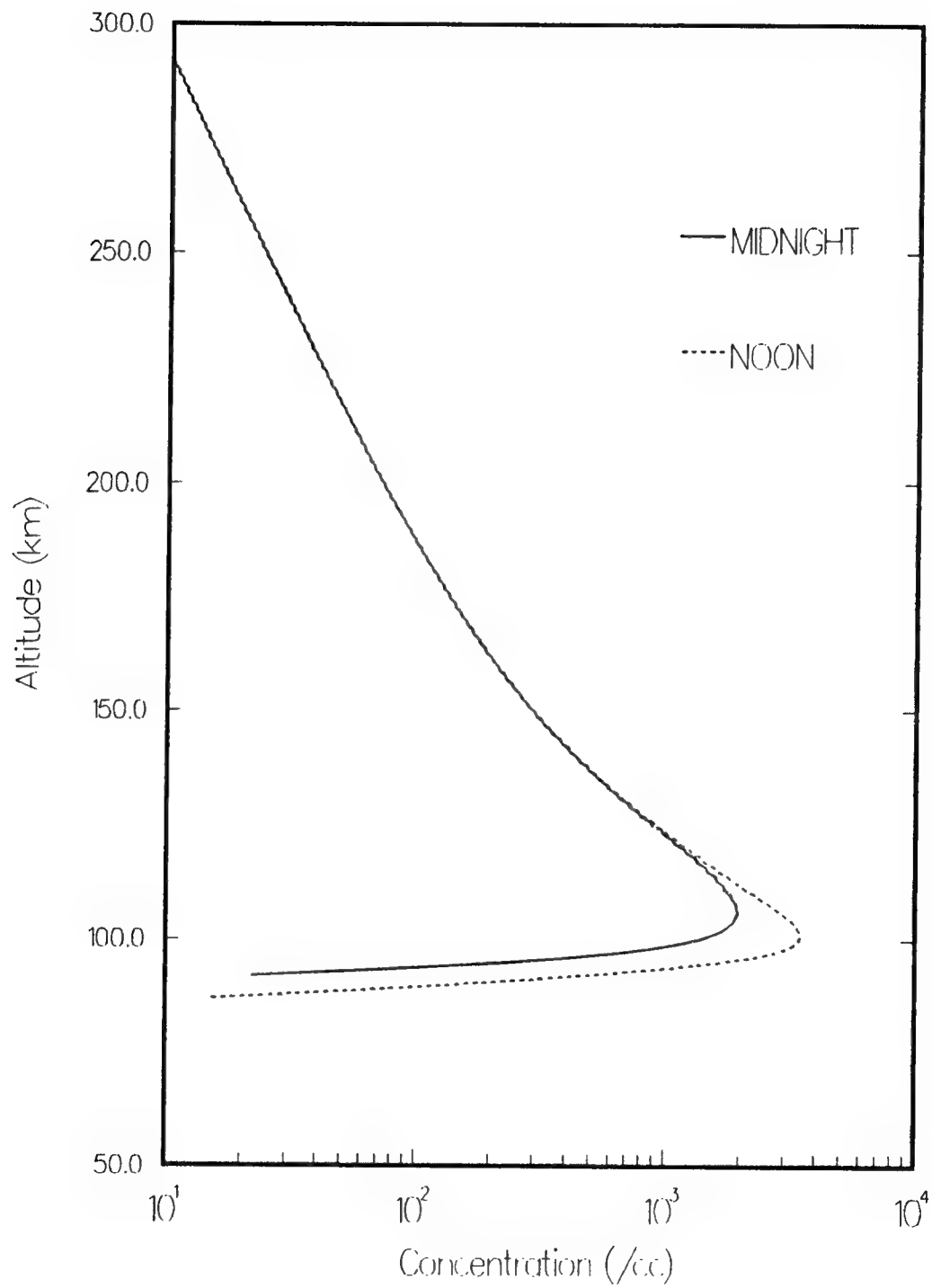


**Figure 31.** Mg<sup>+</sup> Profiles from the Time Dependent Model.

# Ratio of Mg Ions to Mg Neutrals

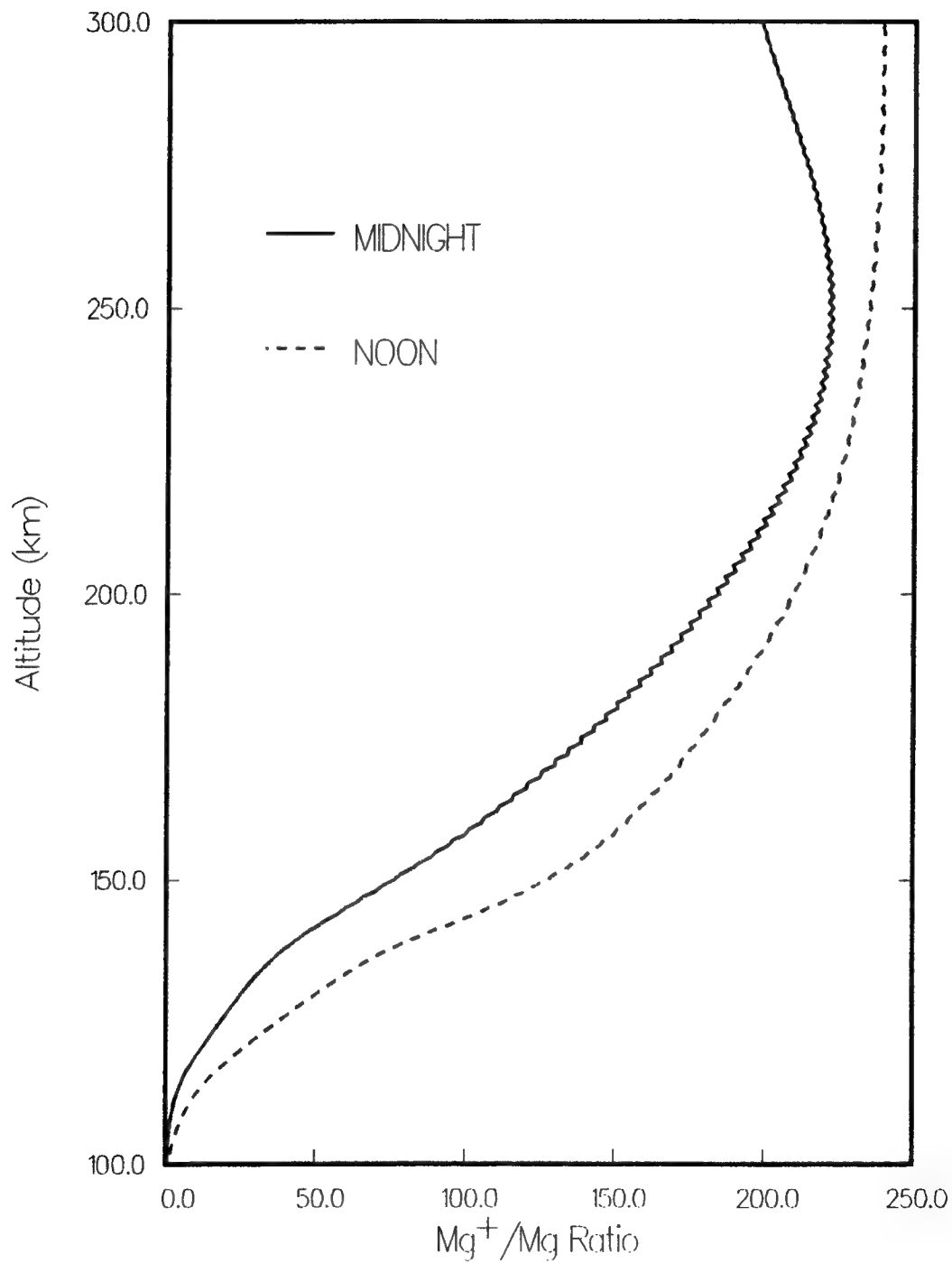


**Figure 32.** Profile of the ratio of  $Mg^+/Mg$ .

# Mg<sup>+</sup> Column Density

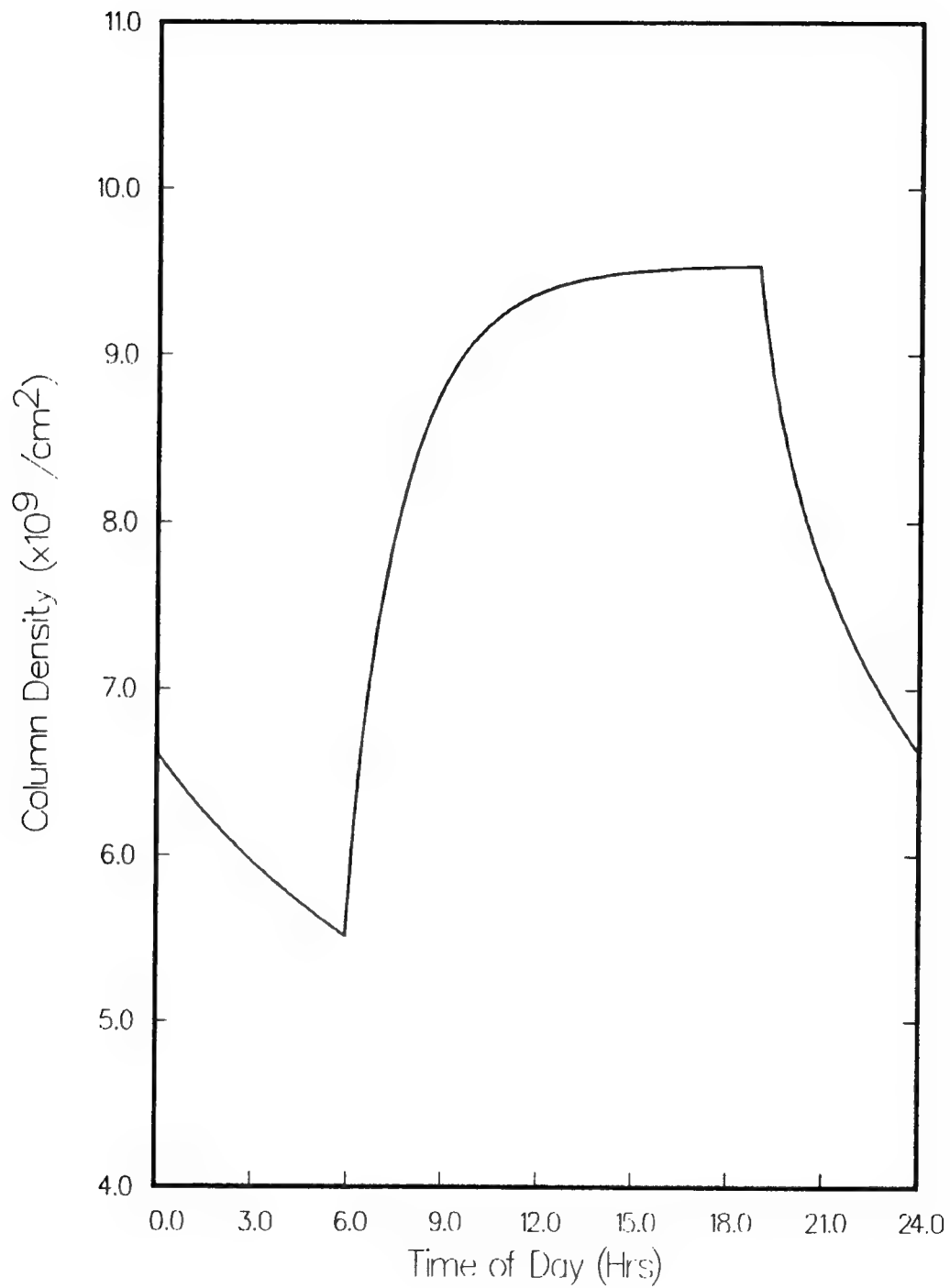


**Figure 33.** The Mg<sup>+</sup> Column Density Diurnal Variation.

# $Mg^+$ Density (/cc) without Electric Fields

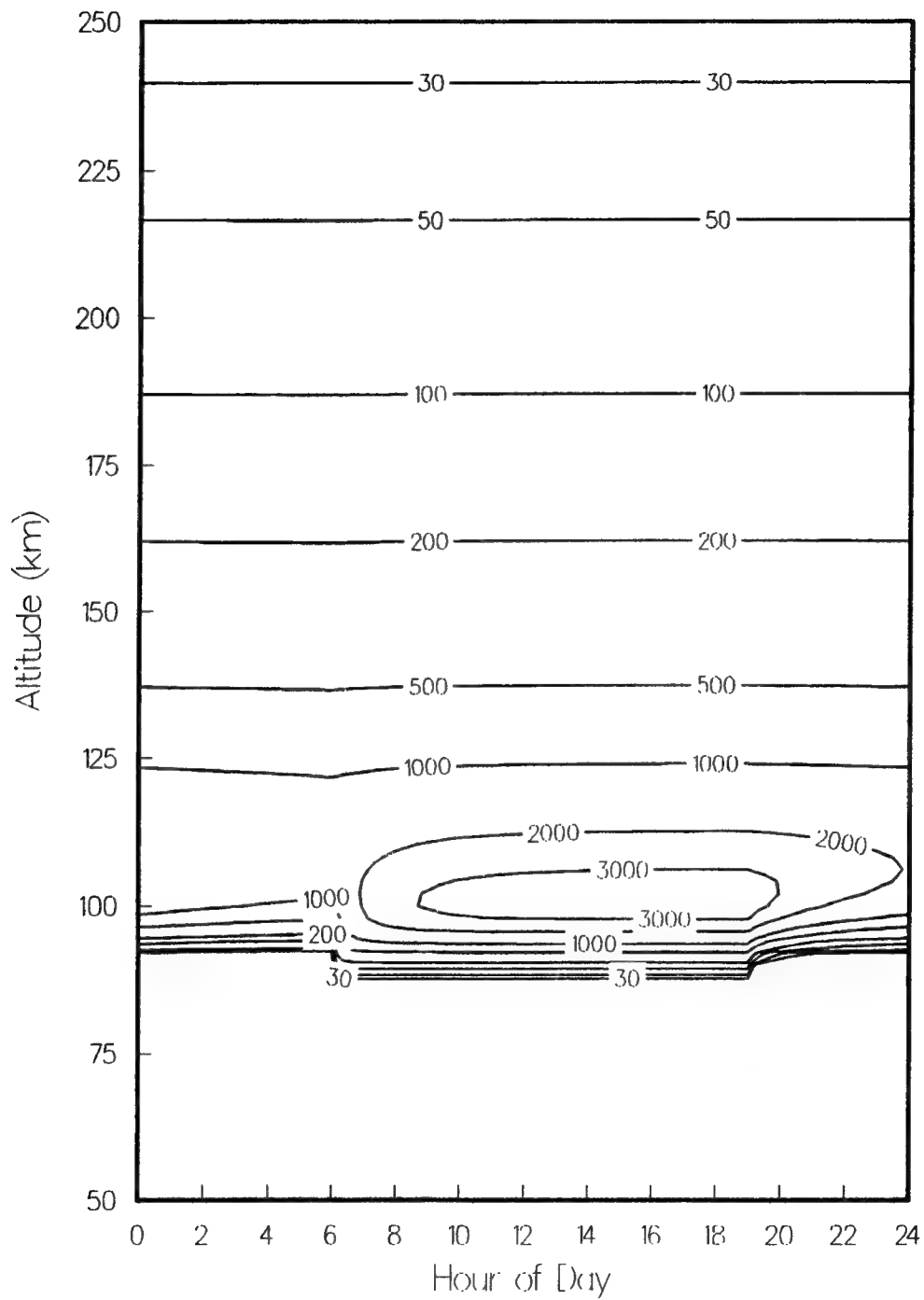


**Figure 34.** The  $Mg^+$  Density Diurnal Variation.

### 4.3 ELECTRIC FIELDS

In the ionosphere and magnetosphere, it is generally assumed that electric fields do not exist parallel to the magnetic field  $B$ . This is because the plasma will rapidly adjust to large scale fields by distributing itself along the field line in such a way as to cancel the charge imbalance. However, permanent electric fields can exist in directions perpendicular to the magnetic field. At the magnetic equator, the impact of the solar wind plasma upon Earth's magnetic field causes a separation of charge with ions drifting duskward and electrons drifting dawnward [Kelley, 1989].

An empirical model of this field at several geomagnetic latitudes has been generated by *Richmond, et al.* [1980] and is sufficient for our purposes here. This model includes data from four stations, one of which is Jicamarca, Peru. This station is nearly on the geomagnetic equator and, for simplicity, we will limit the model to the equator as well. The analytical form of the model was not immediately available, but the electric fields could be obtained approximately from plots reproduced by *Kelley* [1989]. At the magnetic equator, the magnetic field is entirely horizontal. Therefore, the east/west electric field will produce up and down ion motion and the upward electric field will cause motion in the east/west direction. It is only the east/west electric field that is of concern to us here. The field, as abstracted from *Richmond, et al.* [1980] is shown in Figure 35. We note that the maximum in eastward field is just pre-noon, as predicted. The minimum, however, is somewhat post-midnight. This field model should be considered representative of the general behavior of the e-field at the equator. It should be noted, still, that there are seasonal and day-to-day dependencies that should be considered in a more comprehensive model. Our purpose here is to show that the electric fields are capable of producing the behavior seen in the GLO experiment.

To include these fields in the present model, we follow the development of *MacLeod, et al.* [1974]. To begin, the electric field  $\mathcal{E}$  is defined in an easterly direction  $\mathcal{E}_x$ , a direction up,  $\mathcal{E}_z$  and the third direction north,  $\mathcal{E}_y$ . "East" here is taken to be geomagnetic east, so that the magnetic field vector is in the coordinate y-z plane. Following *MacLeod, et al.* [1975] the averaged equation of motion for the ions is given by

$$\rho_i (u - v_i) + E + v_i \times \Gamma = 0 \quad (18)$$

where  $\rho_i$  is the ratio of ion collision frequency to gyrofrequency,  $\Gamma$  is the normalized magnetic field and  $E \equiv \mathcal{E}/B_0$  is the normalized electric field. In our units,  $E$  is obtained by dividing  $\mathcal{E}$  by the magnetic field magnitude, which we take to be 0.27 G, and then multiplying by ten to convert to units of meters per second.

Now, under the assumption that  $B \cdot E$  is zero, Eq(18) can be solved for the drift velocity in the upward direction as follows.

# Eastward Field at Jicamarca

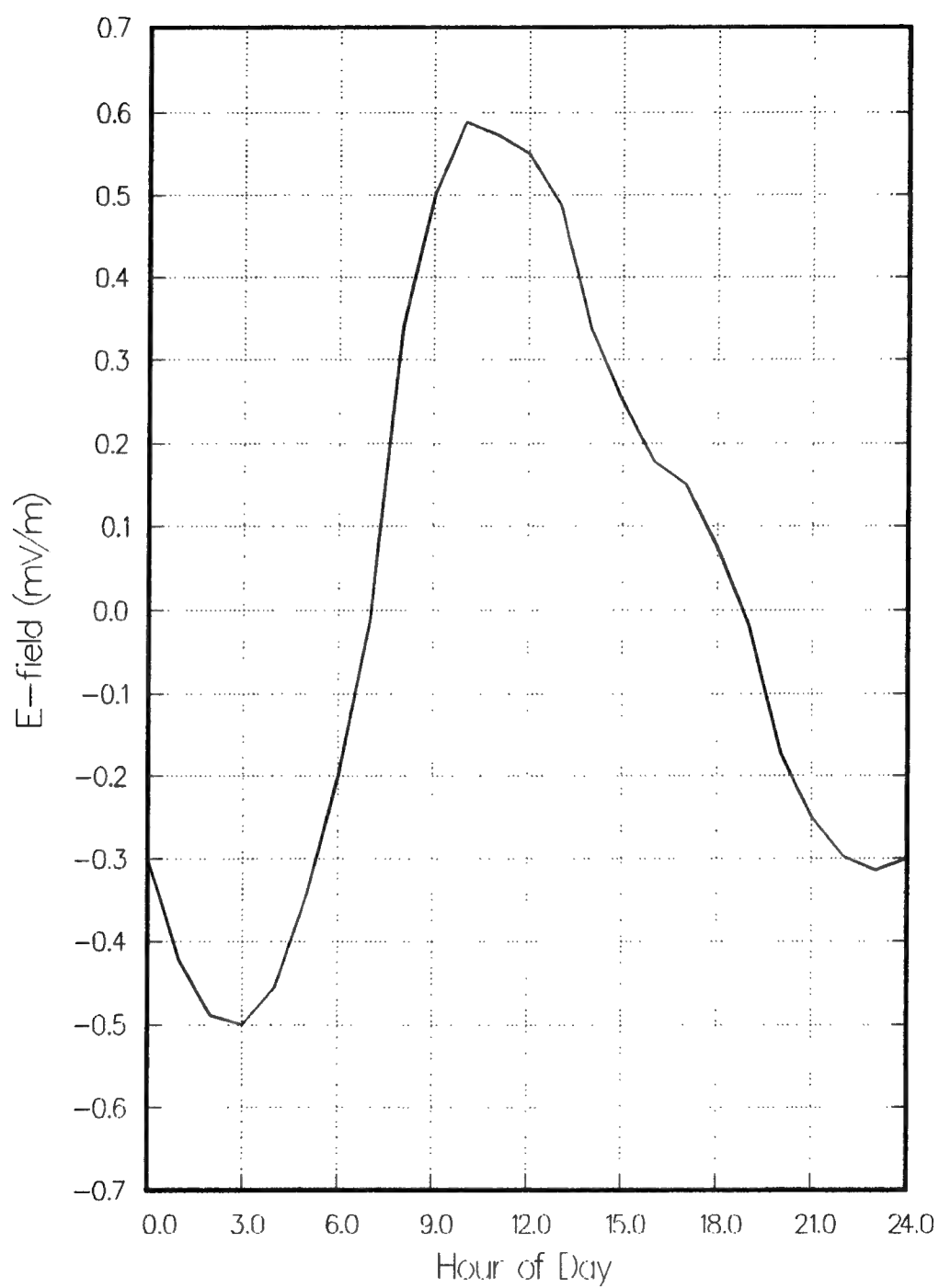


**Figure 35.** Model eastward electric field at Jicamarca.



$$v_z = \frac{\Gamma_y}{(1 + \rho_i^2)} \left[ -\frac{\rho_i}{\Gamma_z} E_y + E_x \right] \quad (19)$$

On the equator,  $E_y$  is zero and  $\Gamma_y$  is unity, simplifying Eq(18) to a form involving only the eastward electric field  $E_x$ , the component shown in Figure 35. All that remains is to calculate the altitude dependant collision frequency ratio  $\rho_i$ .

*Banks and Kockarts* [1973] give convenient expressions for the frequency of ion/ion and ion/neutral collisions, which were employed for this work. For ion/neutral collisions, the collision rate is given by

$$\nu_{in} = 2.6(-9)n_n(\alpha_0/\mu)^{1/2} \quad \text{sec}^{-1}$$

where  $\alpha_0$  is the polarizability of the ion, taken to be 1.75 in this model.  $\mu$  is the ion/neutral reduced mass, which was calculated from the altitude dependent atmospheric mass tabulated by *Kelley* [1989]. The atmospheric number density  $n_n$  was also derived from that source. The ion/ion collision frequency was calculated from the formula

$$\nu_{ii} = 1.3 n_i \frac{\mu^{1/2}}{T_i^{3/2}} \quad \text{sec}^{-1} \quad (21)$$

where  $\mu_i$  is the  $\text{Mg}^+$  ion to atmospheric ion reduced mass and  $T_i$  is the ion temperature.  $n_i$  was derived from the IRI results of Figures 17 and 18, as was the average reduced mass. Ion temperature was kept constant at 800 °K. Finally, the ion cyclotron frequency was taken to be

$$\Omega_i = \frac{1505}{2\pi} \frac{B}{M} \quad \text{sec}^{-1} \quad (22)$$

with B in Gauss and M in AMU. The resulting curve for  $\rho_i$  is shown in Figure 36. This curve actually shows  $(1 + \rho_i^2)^{-1}$ , since this quantity indicates directly the relation between electric field magnitude and corresponding ion motion as a function of altitude. We see that below about 120 km, the drift caused by the electric field is negligible. Also, above about 160 km it is approximately constant. This is because at low altitude, collisions destroy the collective motion of the ions. The fields that are obtained from the use of this  $\rho_i$  function and the eastward field in Figure 35 are shown in Figure 37.

## Ion Collision Frequency Ratio

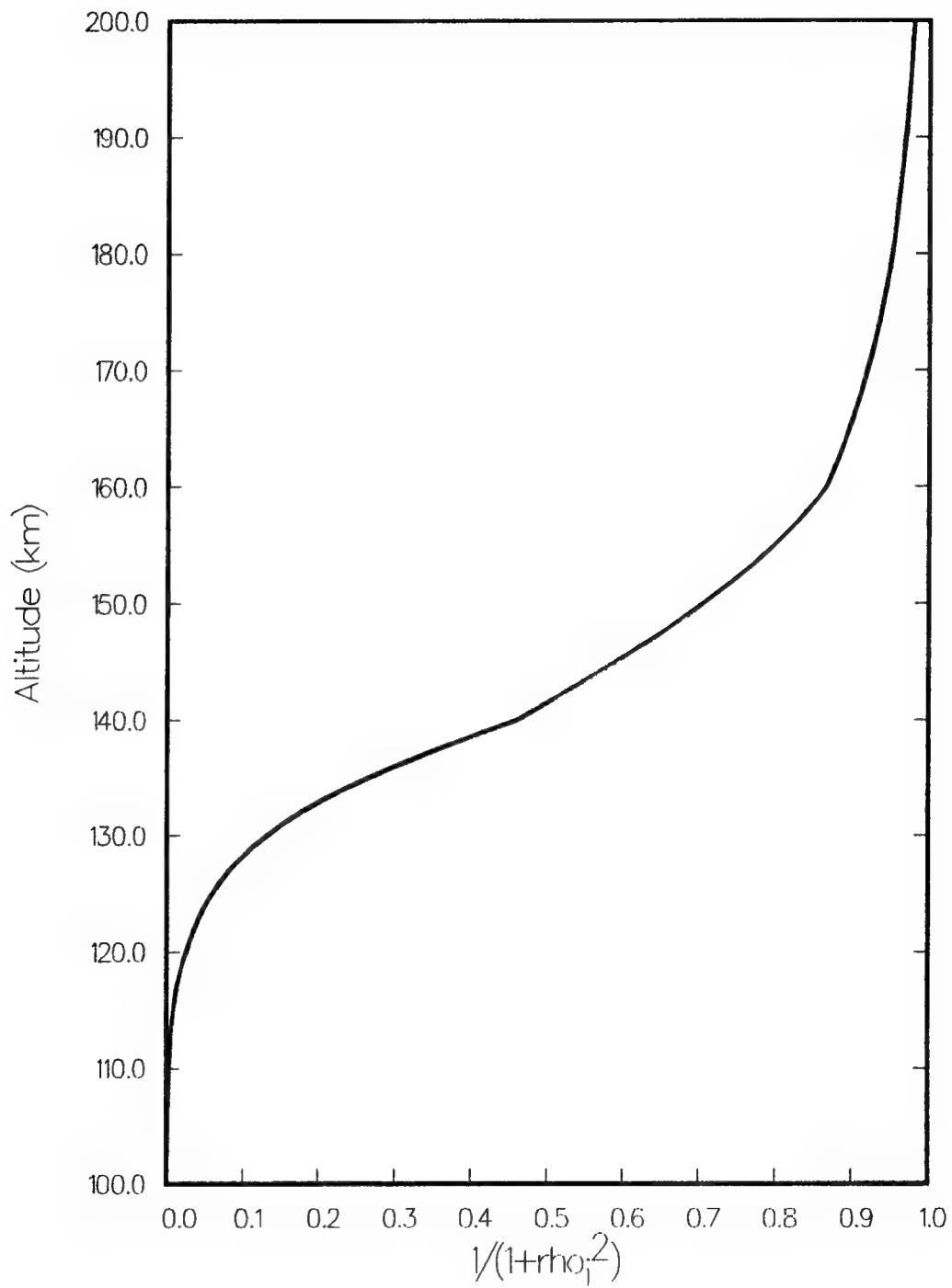


**Figure 36.** The influence of eastward electric fields on ion motion.

# Ion Drift Velocities (meters/sec)

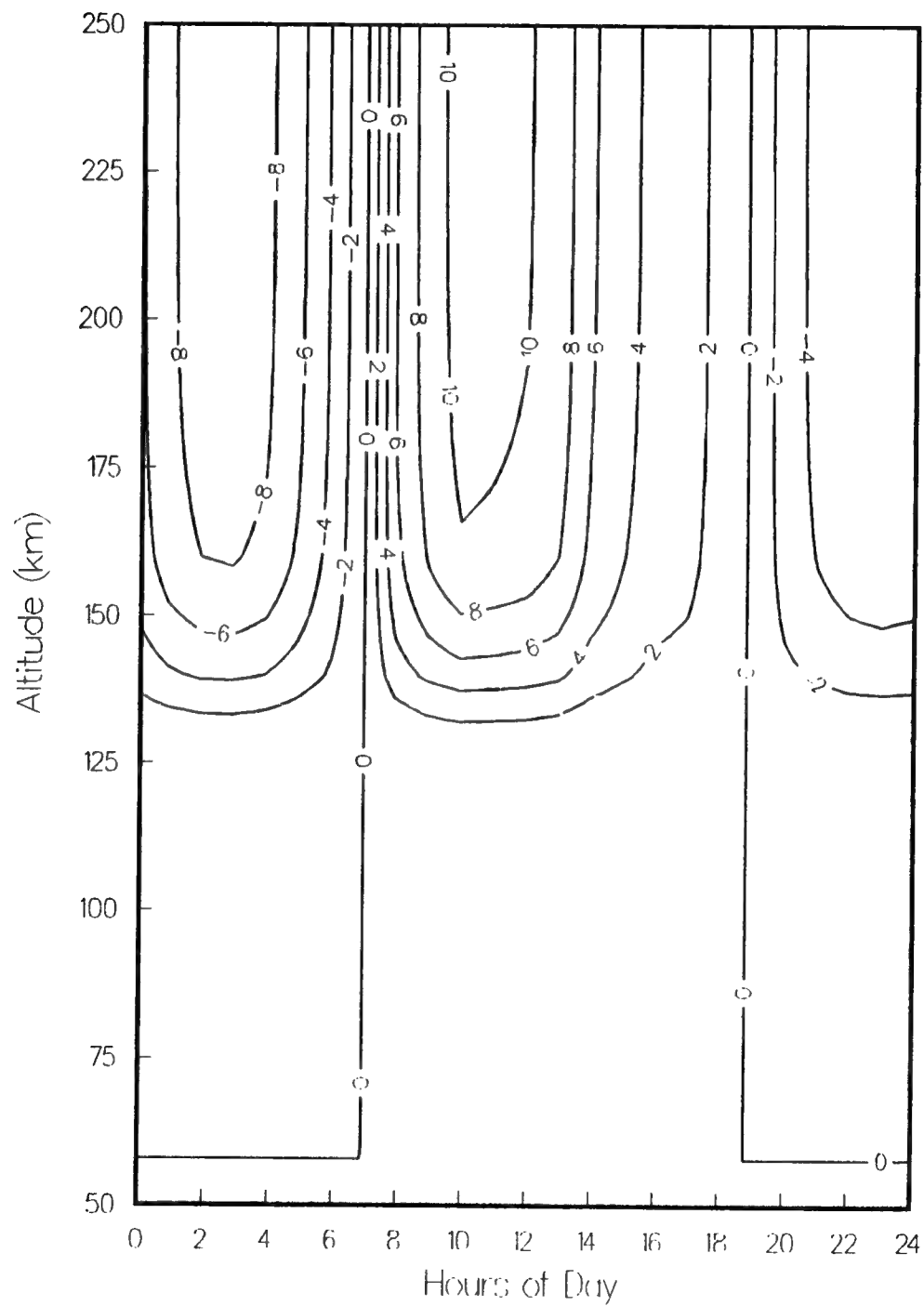


**Figure 37.** Calculated upward ion drift velocities.

The electric fields are introduced into the computation as an extra velocity imparted to the ions, *i.e.*,

$$w' = w_D + v_z \quad (23)$$

where  $w_D$  is the diffusional transport velocity given in Eq(3). The solution is then identical to that of the two-component model without electric fields. Figure 38 shows a contour plot of the densities that results from solution of this model. Below about 125 km, the solution is more or less identical to that of the previous two component model. Above 125 km, however, we see that there is a blossoming of  $Mg^+$  in the afternoon and an almost complete suppression in the early morning. We will discuss these results more extensively in the next section, when we turn to comparisons of the model with experiments.

## 5. COMPARISON WITH MEASUREMENTS

In this section, we will compare predictions of the model with observations made in the GLO experiment. After a brief discussion of those measurements, we will describe the approach taken to calculate radiance levels from the model densities, then compare these levels to those measured in GLO. Since GLO is a relatively limited data set consisting only of measurements taken near the terminator, and also since we have restricted the present modeling to the geomagnetic equator, we will compare model and measurements only under these conditions.

### 5.1. GLO MEASUREMENTS

In the experiment, the quantity measured was the radiance level of  $Mg^+$  at 2795 Å along the instrument line of sight. It was found [Gardner, *et al.*, 1994] that  $Mg^+$  radiances reached intensities of up to about 1,000 Rayleighs. These were most prevalent at the geomagnetic equator and in the geomagnetic polar region. The polar glow was attributed to auroral activity and, limiting our modeling to the equator, will not be addressed here. The equatorial glow was very pronounced at the dusk terminator but not so on the dawn side. Additionally, data was presented as a function of tangent point altitude. It was found that on the dawn side, emissions were confined to tangent point altitudes below about 150 km. On the dusk side, the strongest emissions were actually observed *above* 200 km tangent point altitude. This striking difference indicates that there is little  $Mg^+$  above 150 km at dawn but a great deal at dusk. Overall, radiance levels peaked on average at a few hundred Rayleighs.

### 5.2. RADIANCE CALCULATIONS

In order to present the results of this model in a form most suitable for comparison with experiment, we now transform them from density into intensity levels. For the GLO experiment

# Magnesium Model w/ Equatorial Fields Full Rate of Mg Deposition

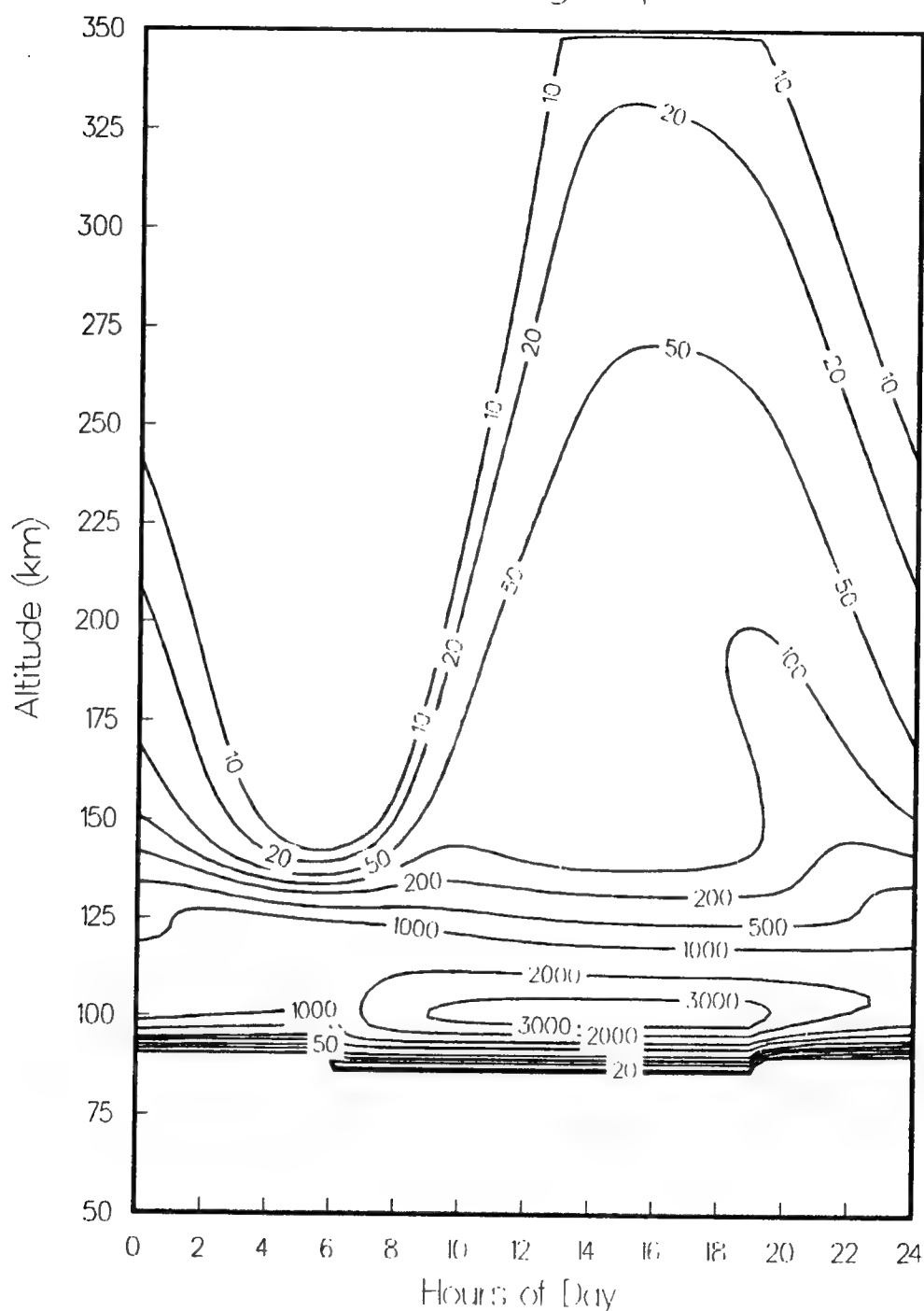


**Figure 38.** Calculated density of  $Mg^+$  with diurnal dependence.

under consideration here, the shuttle was near the terminator at all times. The line of sight of the instrument was directed at an angle away from the sun at a chosen tangent height  $H_t$  to the surface of Earth. The radiation detected arose from direct photo-excitation of the  $Mg^+$  by the sun. Therefore, as one travels along the line of sight, one eventually reaches a point where the shadow of Earth no longer allows for illumination. Also, as one travels along the line of sight, the local time of the volume element of  $Mg^+$  at that particular point changes. All these features were taken into account in the modeling of the  $Mg^+$  intensity. The geometry chosen for the model is shown in Figure 39.

We begin at the shuttle, with an altitude  $H_s$  taken to be 326 km. For a particular tangent height chosen for calculation, the vectors from Earth to the shuttle and to the line of sight at the tangent point are, respectively,

$$r_s = H_s + r_e \quad r_t = H_t + r_e$$

with  $r_e$  the Earth radius. The angle between the line of sight and the nadir vector is then given by

$$\sin \Theta = \frac{r_t}{r_s} \quad (25)$$

We can simplify the calculation if we restrict the line of sight and the shuttle to lie in the equatorial plane. This is about the best we can do for an average calculation of the radiance in any case, since we are restricting the model to the equator and more detailed study would require a case by case analysis of the shuttle attitude. With this approximation, each point along the line of sight can be calculated from

$$x_n = n \Delta_x \quad y_n = y_0 - n \Delta_y \quad (26)$$

where the components are given in a coordinate system in which the shuttle is initially along the y-axis so that  $y_0$  equals  $r_s$ . The altitude of the  $n$ 'th point is then given simply by

$$H_n = \sqrt{x_n^2 + y_n^2} - r_e \quad (27)$$

We can easily check to see if the point is illuminated from whether  $y_n$  is greater than  $r_e$ . If so, we count point in the calculation. Finally, we obtain the local time of each point can be calculated from

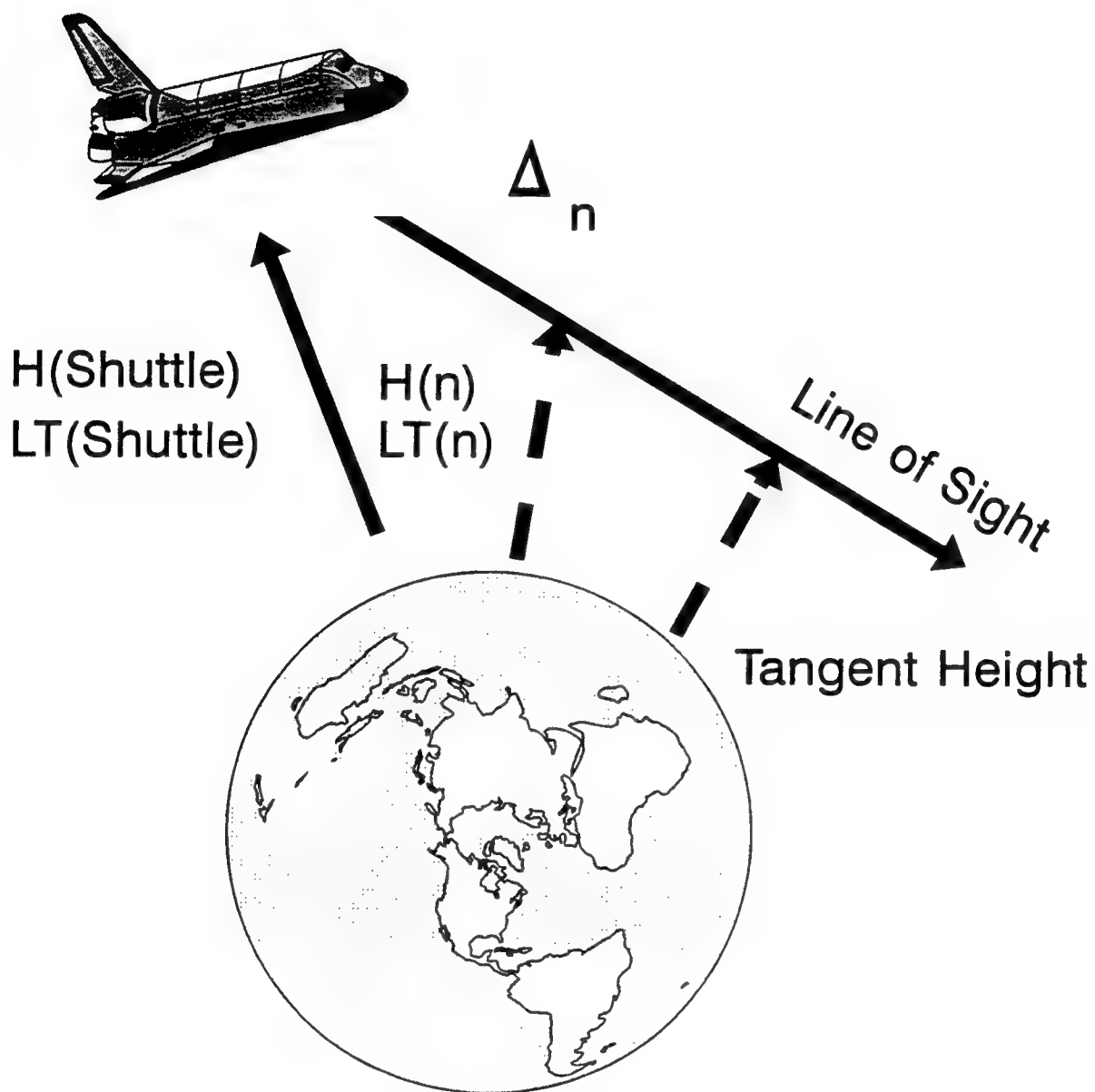


**Figure 39.** Geometry of the  $\text{Mg}^+$  Radiance Calculation.

$$\phi_n = \phi_s \pm \tan^{-1} \frac{x_n}{y_n} \quad (28)$$

where the negative will obtain if the shuttle is on the morning side and the positive if on the morning side.  $\phi_n$  in Eq(28) is the local time of the n'th step along the line of sight and  $\phi_s$  is the local time of the shuttle.

Summing these densities along the line of sight and multiplying by the step size gives the column density of *illuminated*  $\text{Mg}^+$  ions along the line of sight. This is then multiplied by the g-factor for the appropriate transition, which in this case is the transition at 2803 Å. This was calculated by *Anderson and Barth* [1971] to be 0.091 photons/second. Finally, we divide by 1(6) to obtain the Rayleighs. We present results of this calculation only for the shuttle at local dawn and local dusk. These are the positions for which data was most prevalent in the experiment, due to the dawn-dusk orbit of the shuttle.

### 5.3. MODEL RESULTS

We now examine the predicted radiance levels of the model. We begin with the full deposition rate and kinetic model 2D, the diurnal profile of which was shown in Figure 38. The corresponding radiance for dawn and dusk is shown in Figure 40 as a function of tangent point altitude. It is quite striking that the radiance on the dusk side extends to very high altitudes, showing a secondary maximum at about 200 km. The curve at dawn, on the other hand, falls off rapidly as the tangent height altitude increases and shows virtually no radiance above about 125 km. This is simply because there is little  $\text{Mg}^+$  above this point. We see, too, that the radiance predictions of this model are overall too high. While the GLO experiment showed radiances of at most 1,000 Rayleighs, this model predicts a maximum of some 5,000 Rayleighs. It should be noted that there are many complications in adopting any single result as "truth", especially in light of the variability of intensity with geometry, location, and time of day. However, gathering all the information from experiments presented here so far, it becomes clear that the model predictions are somewhat too high, both in terms of radiance and of peak ion densities.

One possible reason, which we have already noted, is that the deposition rate chosen is too large. Various models constructed by others have included fractional deposition rates [*Carter and Forbes*, 1993] intended to represent the fraction of metal that is deposited in atomic form. Others [*e.g. Plane*, 1991] simply scale the deposition rate to achieve better agreement with observations. In light of the uncertainty, it seems reasonable to assume that the deposition rate is a good candidate for variation. This we do by decreasing the deposition rate of Mg to 25% the value calculated in Section 2 at all altitudes. The resulting diurnal profiles from this calculation, again for Model 2D, are shown in Figure 41. The profiles are basically the same in shape as those in Figure 38 but the overall magnitude is reduced by about a factor of four, as expected. The radiance curves from this model are shown in Figure 42. As with the



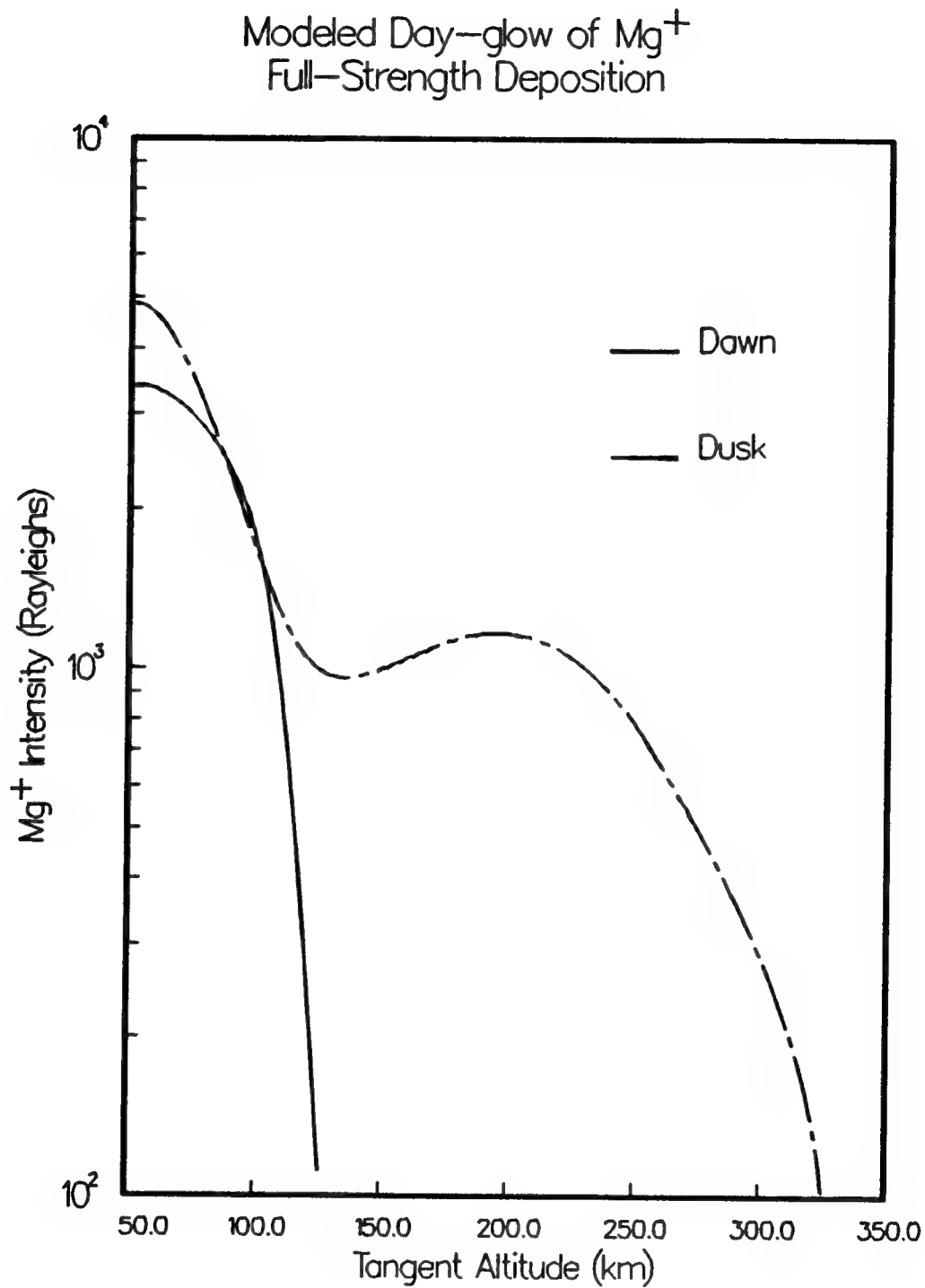


Figure 40. Radiance computed from the  $\text{Mg}^+$  model with full deposition.

Magnesium Model w/ Equatorial Fields  
25% of Total Deposition

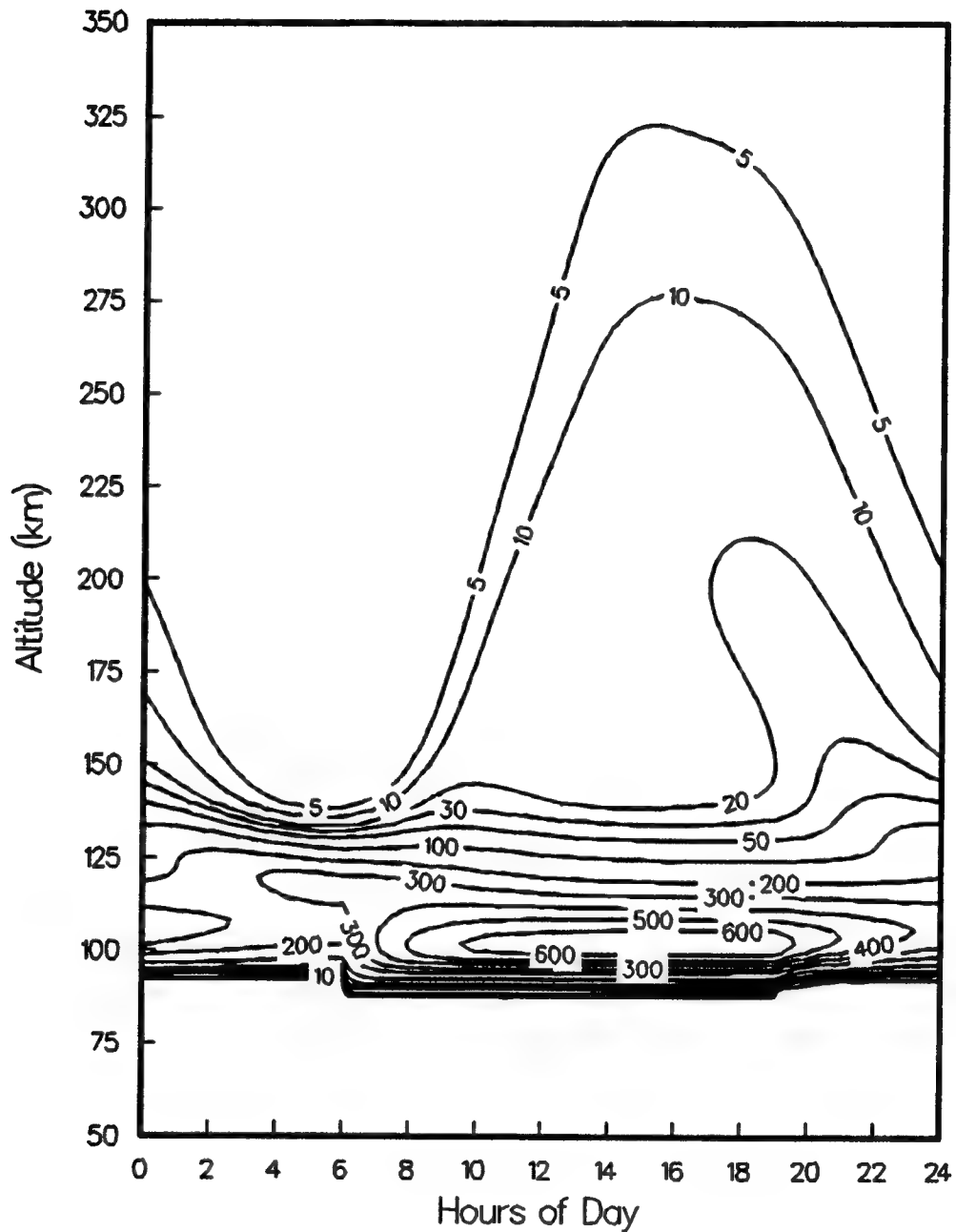
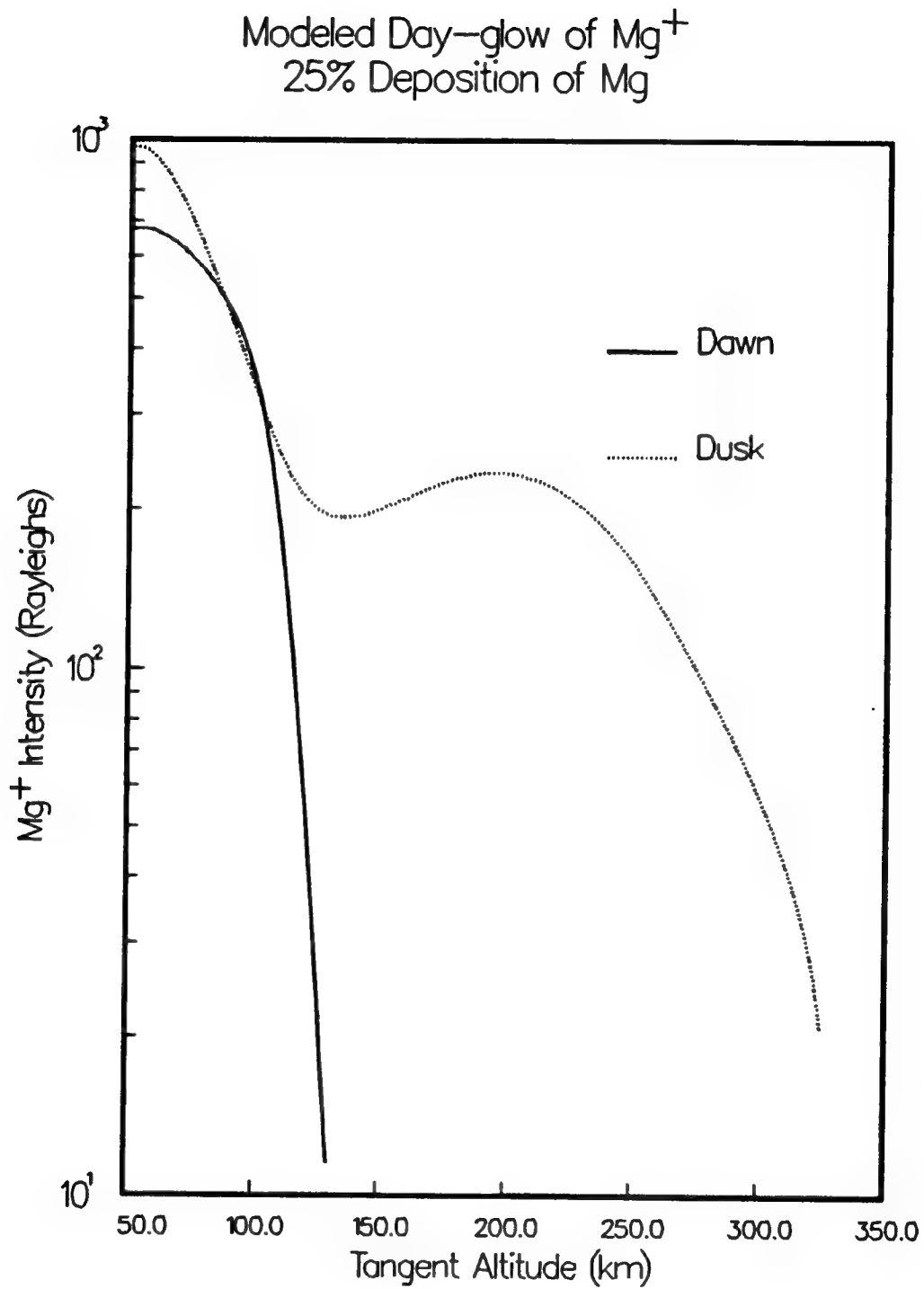


Figure 41. Calculated  $Mg^+$  density with 25% Mg deposition.



**Figure 42.** Radiance computed from the  $\text{Mg}^+$  model with 25% deposition.

profiles, there is an approximately linear reduction in the intensity, which peaks at about 1 KR and shows the secondary maximum at dusk of some 250 Rayleighs at about 200 km tangent point altitude. The predictions of this model are well within the bounds of the GLO measurements.

For comparison, it is instructive to return to kinetic model 2B at this point. Figure 43 shows the diurnal profiles and Figure 44 the radiance results from this model. Interestingly, the profiles differ from those of model 2D in that the maximum comes approximately at dawn. This maximum is not caused by kinetics but rather by the ions being pushed down by the electric field during the night. Even though the velocities at 125 km are not sufficient to transport the ions, downward diffusion does take place in this altitude range. This sort of behavior, with a maximum in  $Mg^+$  taking place during the night was found in the rocket measurements of *Aikin and Goldberg* [1973]. These authors conclude that downward drift during the night is responsible for the maximum. It is interesting that this model also reflects this case. The radiance profiles are quite similar to those of Model 2D, except that the peak of the dusk radiance curve between 50 and 100 km has been reduced somewhat. The secondary maximum of around 250 Rayleighs at 200 km is still present.

Finally, in Figure 45 we show the ratio of  $Mg^+$  to  $Mg$  as predicted by Model 2b. This ratio is of interest since it is frequently measured, or at given a lower limit in cases where radiance from neutral  $Mg$  cannot be seen. An interesting thing to note in Figure 45 is that the ratio at high altitudes is very dependent on the time of day. As ions are swept down by the fields, the neutrals with which they were in kinetic equilibrium remain behind for a relatively long time. This causes the ratio to drop below unity at dawn above 150 km. Also, ratios can be below twenty up to 150 km in the afternoon. The fact that the ratio has such a strong diurnal dependence is significant and should be considered in the interpretation of conclusions drawn from these type of measurements. In Figure 46 we show the concentration of neutral  $Mg$  at high altitudes. This shows a small but significant high altitude component in the afternoon, which results from electron induced neutralization of  $Mg^+$ .

## 6. CONCLUSION

We have constructed a model of the diurnal behavior of  $Mg$  ion at the geomagnetic equator. The model includes diffusion, kinetics and transport of the ions by electric fields. The model predicts a strong enhancement of  $Mg^+$  emission at dusk. Significant emissions can persist to very high tangent point altitudes. The predictions of the model compare favorably to observations made in the GLO experiment, where those observations are compatible. It is likely that the model would also predict relatively weak emissions above magnetic latitudes of ten degrees or so, since the influence of electric fields rapidly falls off with increasing magnetic latitude. The variation of the model with varying magnetic latitude should certainly be addressed in the future.

Densities for Magnesium Model  
w/ 25% Deposition Rate

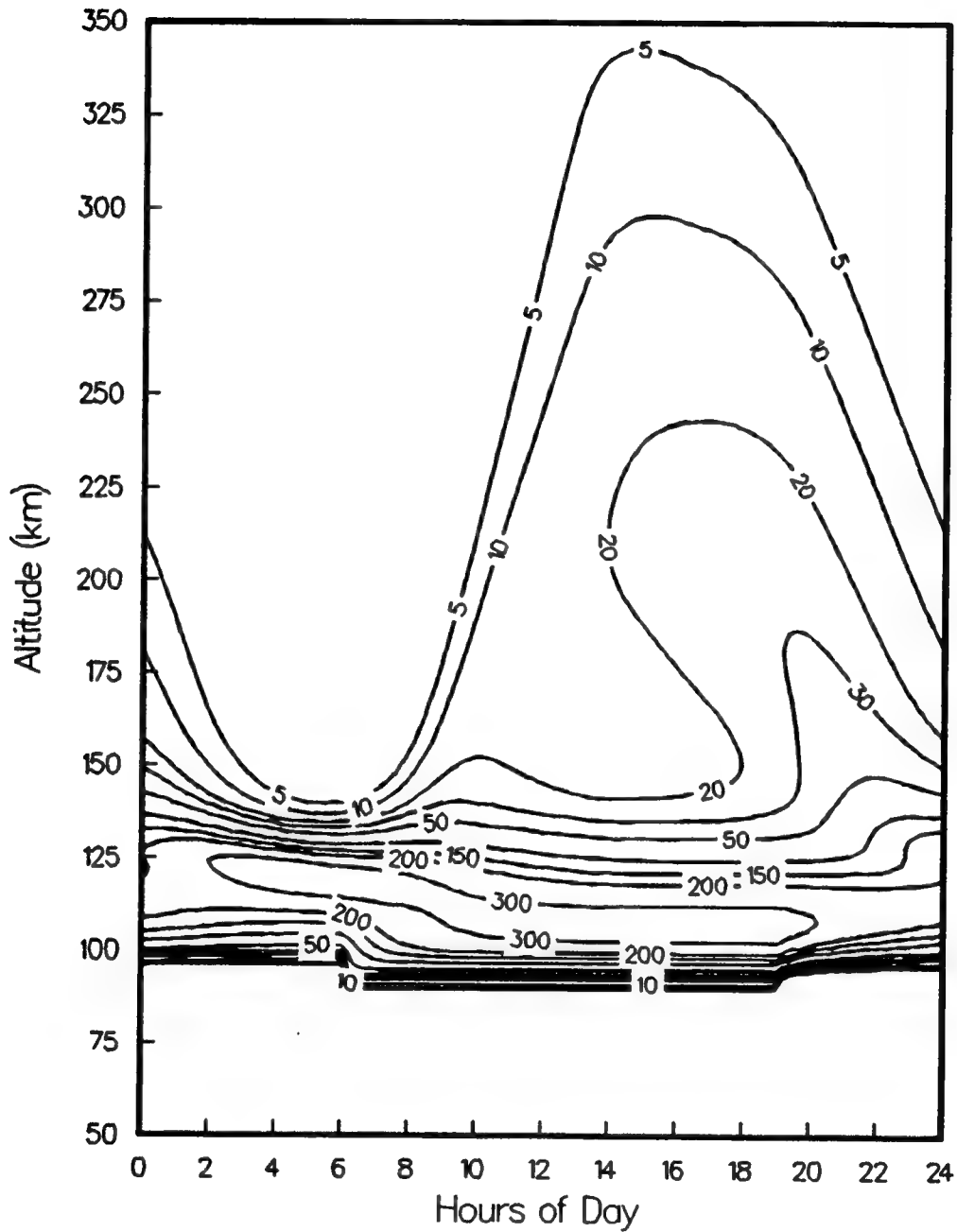


Figure 43. Computed 25% deposition profile with Model 2b.

### Modeled Day-glow of $\text{Mg}^+$

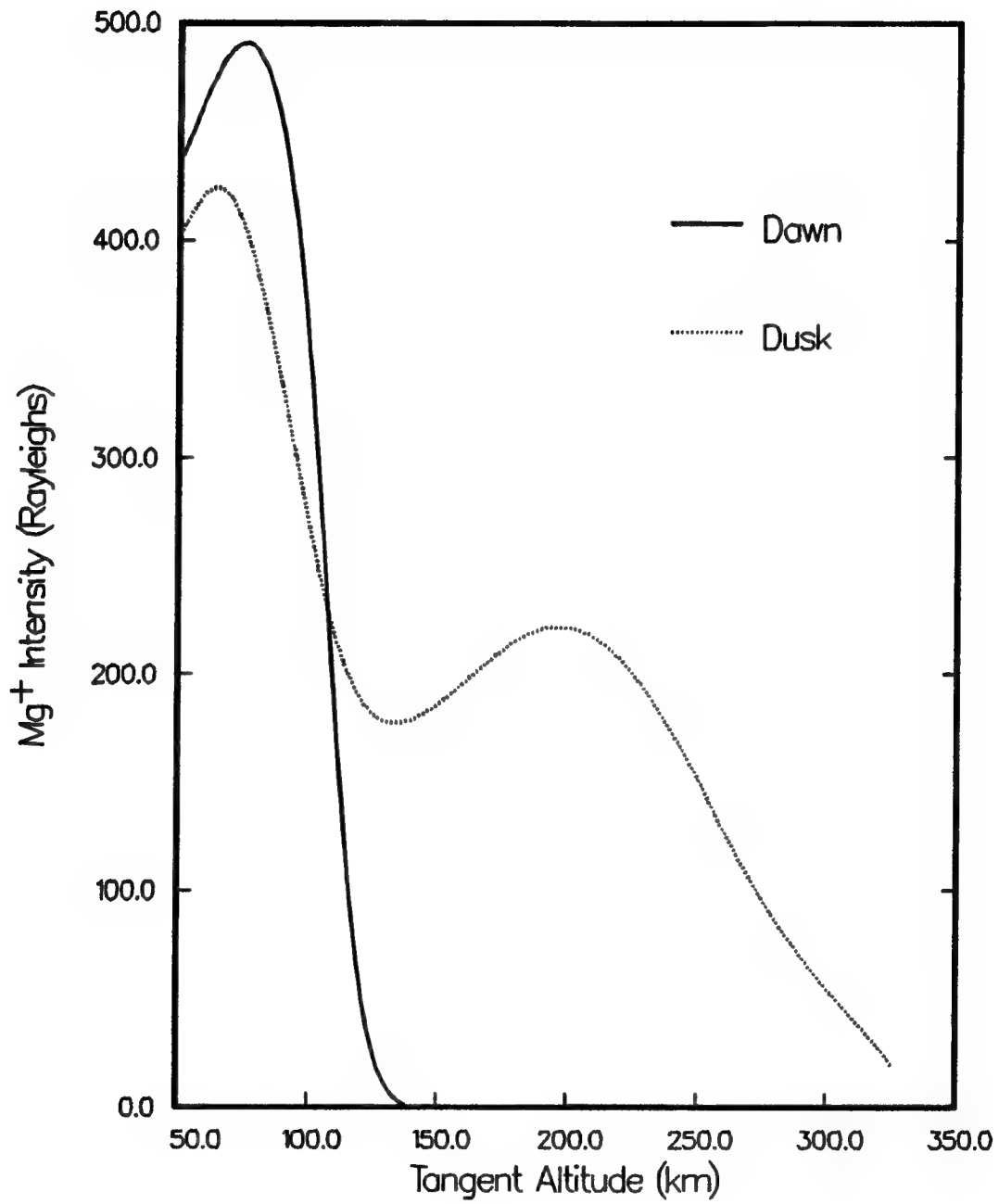


Figure 44. Radiance computed from 25% deposition and kinetic model 2b.

# Magnesium Model Ion/Neutral Ratio Kinetic Model 2B

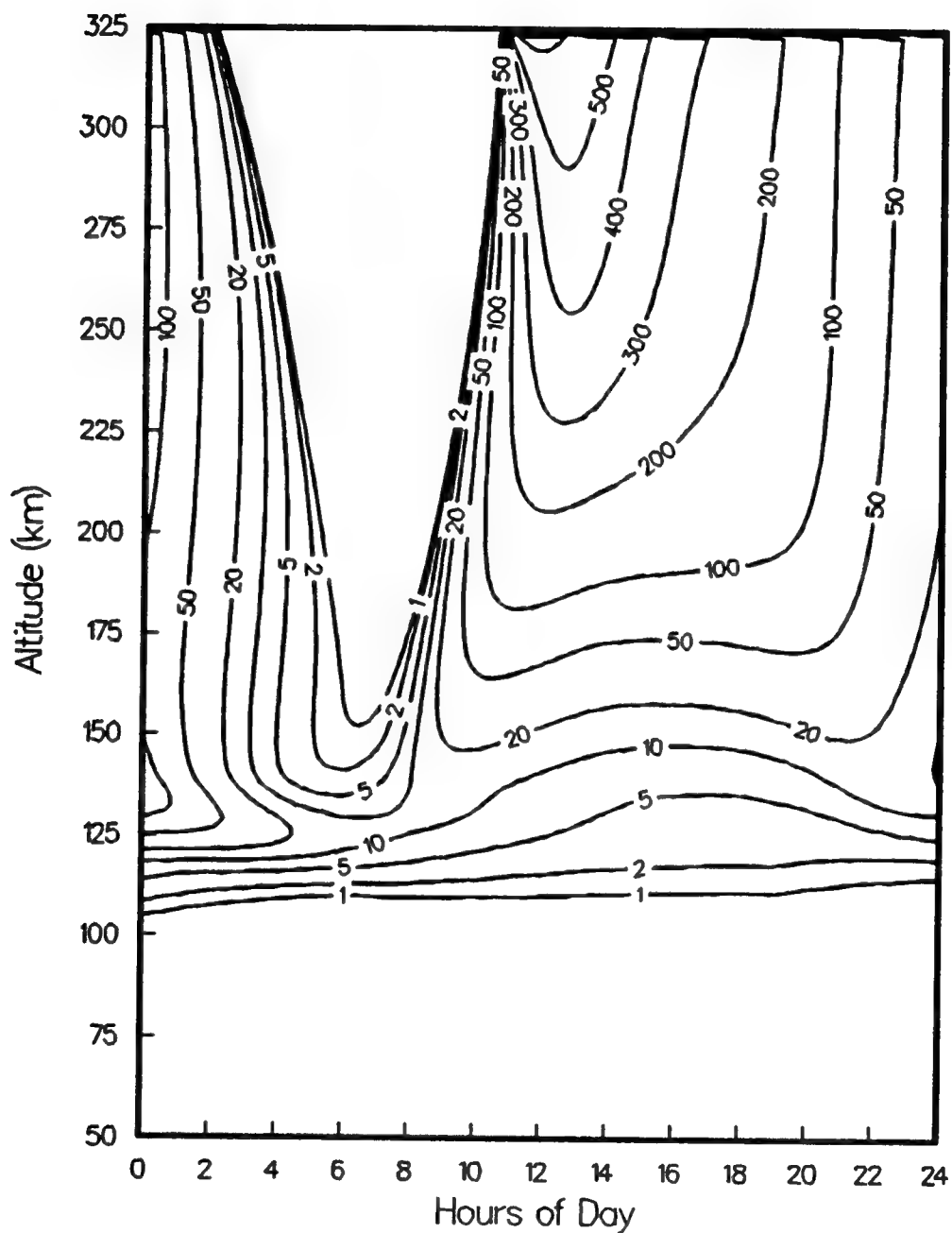


Figure 45. Ratio of  $Mg^+$  to  $Mg$  as predicted by Model 2B.

## Densities for Magnesium Model with Electric Fields

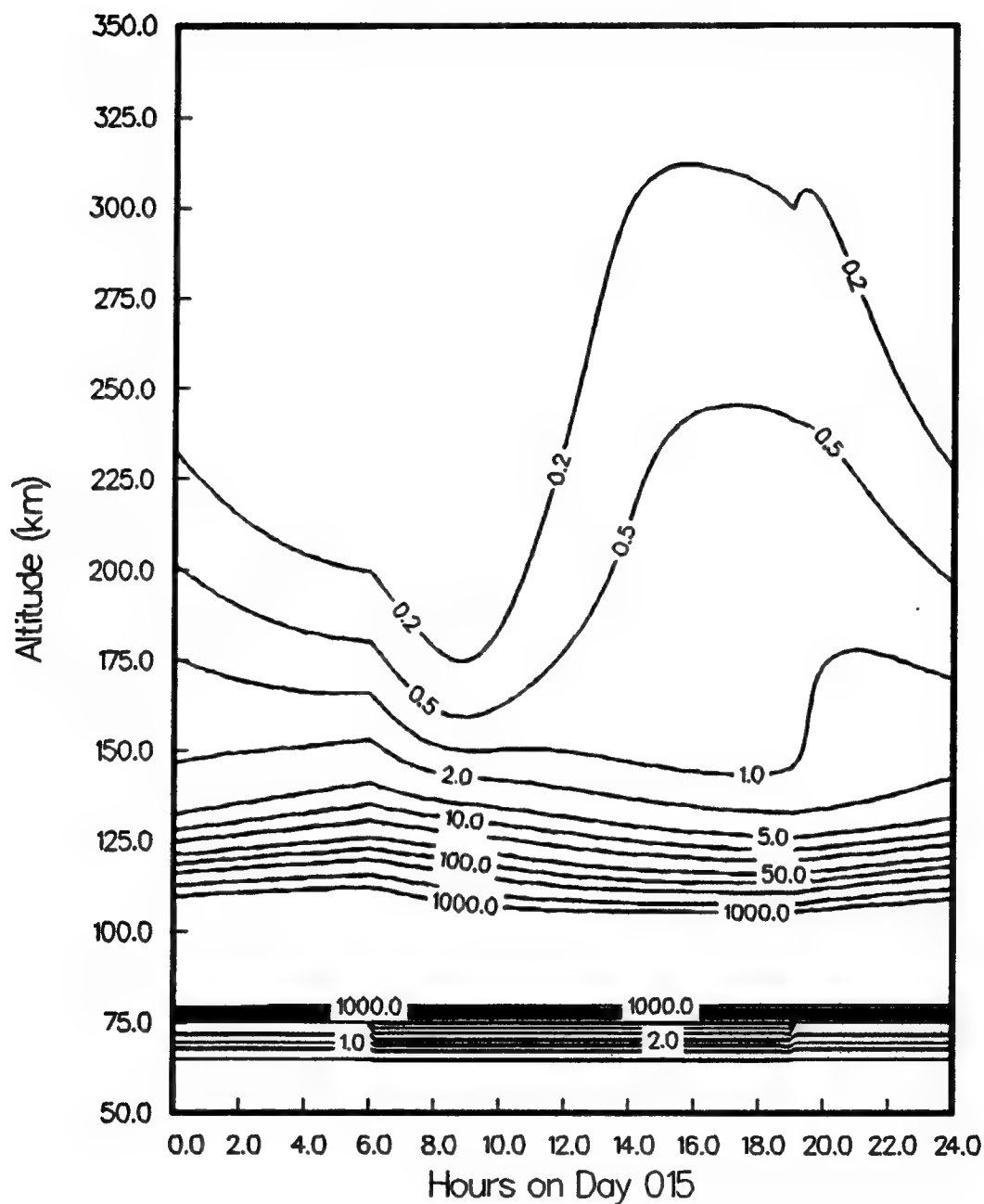


Figure 46. Concentration of neutral Mg from Model 2B.



## 7. REFERENCES

- Ager, J. W. and C. J. Howard, "Kinetics and diffusion of gas phase sodium species, Ph.D. thesis, University of Colorado, 1986.
- Aikin, A. C. and R. A. Goldberg, Metallic ions in the equatorial ionosphere, *J. Geophys. Res.*, **78**, 734, 1973.
- Allen, M., J. I. Lunine, and Y. L. Yung, "The vertical distribution of ozone in the mesosphere and lower thermosphere", *J. Geophys. Res.*, **89**, 4841, 1984.
- Anderson, J. G. and C. A. Barth, Rocket investigation of the Mg I and Mg II dayglow, *J. Geophys. Res.*, **76**, 3723, 1971.
- Banks, P. M. and G. Kockarts, "Aeronomy", Academic Press, Inc., New York (1973).
- Bates, D. R. and A. Dalgarno, Electric recombination, in *Atomic and Molecular Processes*, edited by D.R. Bates, p. 245, Academic Press, New York, 1962.
- Carter, L. N., Jr. and J. M. Forbes, A numerical simulation of mid-latitude ion layering, *J. Geophys. Res.*, *preprint*, 1993.
- Ferguson, E. E. and F. C. Fehsenfeld, Some aspects of the metal ion chemistry of the earth's atmosphere, *J. Geophys. Res.*, **73**, 6215, 1968.
- Ferguson, E. E., Atmospheric metal ion chemistry, *Radio Sci.*, **7**, 397, 1972.
- Gardner, J., R. Viereck, E. Murad, S. Lai, D. Knecht, C. Pike, L. Broadfoot, E. Anderson, B. Sandel, and B. McNeil, Mg<sup>+</sup> and other metallic emissions observed in the thermosphere, submitted for publication to SPIE for the Applications of Digital Image Processing XVII Conference, San Diego, CA, July 1994.
- Gérard, J. C. and A. Monfils, The Mg II equatorial airglow altitude distribution, *J. Geophys. Res.*, **83**, 4389, 1978.
- Helmer, M., J. M. C. Plane, and M. R. Allen, A kinetic investigation of the reaction of Ca + O<sub>3</sub> over the temperature range 213-383 K, *Chem. Soc. Faraday Trans.* **89**, 763 (1993).
- Hughes, D. W., Cosmic dust influx to the earth, *Space Research XV*. Akademie-Verlag, Berlin, 1975.
- Istomin, V. G., Ions of extra-terrestrial origin in the earth's ionosphere, *Space Res.*, **3**, 209 (1963).

- Johnson, F. S., ed. "Satellite Environment Handbook", Stanford University Press, Stanford, California, 1961.
- Johnson, F. S., and B. Gottlieb, Eddy mixing and circulation at ionospheric levels, *Planet. Space Sci.*, **18**, 1707 (1970).
- Kelley, M. C., "The earth's ionosphere", *International Geophysics Series, Vol. 43*, Academic Press, Inc., New York, 1989.
- Keneshea, T. J., S. P. Zimmerman and C. R. Philbrick, "A dynamic model of the mesosphere and lower thermosphere", *Planet. Space Sci.*, **27**, 385, 1979.
- Kopp, E., and U. Herrmann, Ion composition in the lower ionosphere, *Annales Geophysicae*, **2**, 83, 1983.
- Love, S. G. and D. E. Brownlee, Heating and thermal transformation of micrometeroids entering the earth's atmosphere, *ICARUS*, **89**, 26, 1990.
- MacLeod, M. A., T. J. Keneshea, and R. S. Narcisi, Numerical modeling of a metallic ion sporadic-E layer, *Radio Science*, **10**, 371, 1975.
- McNeil, W. J., A model of the atmospheric metal deposition by cosmic dust particles, Radex, Inc., PL-TR-93-2231, 17 November 1993, ADA278561.
- Murad, E., R. A. Viereck, D. J. Knecht and C. P. Pike, Thermospheric metals observed from space: Optical measurements of  $Mg^+$ ,  $Ca^+$  and  $Na$  viewed on the limb, presented at AGU 1994 Spring Meeting, Baltimore, Maryland (1994).
- Nien, Chia-Fu, B. Rajasekhar and J. M. C. Plane, Unusual kinetic behavior of the reactions  $Mg + O_2 + M$  and  $Ca + O_2 + M$  ( $M = N_2, He$ ) over extended temperature ranges, *J. Phys. Chem.*, **97**, 6449 (1993).
- NOAA, NASA, and USAF, "U.S. Standard Atmosphere, 1976", U.S. Government Printing Office, Washington, D.C., 1976.
- Plane, J. M. C., The chemistry of meteoric metals in the Earth's upper atmosphere", *International Reviews of Physical Chemistry*, **10**, 55 (1991).
- Plane, J. M. C. and D. Husain, Determination of the absolute rate constant for the reaction  $O + NaO = Na + O_2$  by time resolved atomic chemiluminescence at 589 nm., *J. Chem. Soc. Faraday Trans.*, **82**, 2047 (1986).

- Richmond, A. D., M. Blanc, B. A. Emery, R. H. Wand, B. G. Fejer, R. F. Woodman, S. Ganguly, P. Amayenc, R. A. Behnke, C. Calderon, and J. V. Evens, An empirical model of quiet-day ionospheric electric fields at middle and low latitudes, *J. Geophys. Res.*, **85**, 4658, 1980.
- Rowe, Fahey, E. E. Ferguson, and F. C. Fehsenfeld, Gas phase magnesium ion chemistry, *J. Chem. Phys.*, **75**, 3325, 1981.
- Rutherford, J. A., R. G. Mathis, B. R. Turner, and D. A. Vroom, Formation of magnesium ion by charge transfer, *J. Chem. Phys.*, **55**, 3785, 1971.
- Swider, W., Jr., Processes for meteoric elements in the E region, *Planet. Space Sci.*, **17**, 1233, 1969.
- Thomas, L., M. C. Isherwood, and M. R. Bowman, A theoretical study of the distribution of sodium in the mesosphere, *J. Atmos. Terres. Phys.*, **45**, 587, 1983.
- Vallance-Jones, A., Calcium and oxygen in the twilight airglow, *Ann. Geophys.*, **14**, 179 (1958).
- Whipple, F. L., The zodiacal light and interplanetary medium, NASA SP 150, 409 (1967).

## **APPENDIX A.**

This appendix gives the complete kinetic models as run. The files were used as input to the KINO kinetic equation program described elsewhere [McNeil, 1993].

# MAGNESIUM NEUTRAL MODEL 1

01)	$\text{Mg} + \text{O}_2 + \text{N}_2 = \text{MgO}_2 + \text{N}_2$	\$	4.3e-36
02)	$\text{MgO}_2 + \text{O} = \text{MgO} + \text{O}_2$	\$	2.0e-14
03)	$\text{MgO} + \text{O} = \text{Mg} + \text{O}_2$	\$	1.0e-10
04)	$\text{Mg} + \text{O}_3 = \text{MgO} + \text{O}_2$	\$	2.0e-10
05)	$\text{MgO} + \text{CO}_2 + \text{N}_2 = \text{MgCO}_3 + \text{N}_2$	\$	2.0e-27
06)	$\text{MgCO}_3 + \text{O} = \text{MgO}_2 + \text{CO}_2$	\$	1.0e-13

# MAGNESIUM ION MODEL 2A

01)	$\text{Mg} + \text{O}_2 + \text{N}_2 = \text{MgO}_2 + \text{N}_2$	\$	4.3e-36
02)	$\text{MgO}_2 + \text{O} = \text{MgO} + \text{O}_2$	\$	2.0e-14
03)	$\text{MgO} + \text{O} = \text{Mg} + \text{O}_2$	\$	1.0e-10
04)	$\text{Mg} + \text{O}_3 = \text{MgO} + \text{O}_2$	\$	2.0e-10
05)	$\text{MgO} + \text{CO}_2 + \text{N}_2 = \text{MgCO}_3 + \text{N}_2$	\$	2.0e-27
06)	$\text{MgCO}_3 + \text{O} = \text{MgO}_2 + \text{CO}_2$	\$	1.0e-13
07)	$\text{Mg} = \text{Mg}^+ + \text{e}^-$	\$	4.0e-07
08)	$\text{Mg} + \text{O}_2^+ = \text{Mg}^+ + \text{O}_2$	\$	1.0e-10
09)	$\text{Mg} + \text{NO}^+ = \text{Mg}^+ + \text{NO}$	\$	1.0e-10
10)	$\text{Mg} + \text{O}^+ = \text{Mg}^+ + \text{O}$	\$	1.0e-10
11)	$\text{Mg}^+ + \text{e}^- = \text{Mg}$	\$	1.0e-12
12)	$\text{Mg}^+ + \text{N}_2 + \text{O}_2 = \text{MgO}_2^+ + \text{N}_2$	\$	2.5e-30
13)	$\text{MgO}_2^+ + \text{e}^- = \text{Mg} + \text{O}_2$	\$	3.0e-07

# MAGNESIUM ION MODEL 2A

01)	$\text{Mg} + \text{O}_2 + \text{N}_2 = \text{MgO}_2 + \text{N}_2$	\$	4.3e-36
02)	$\text{MgO}_2 + \text{O} = \text{MgO} + \text{O}_2$	\$	2.0e-14
03)	$\text{MgO} + \text{O} = \text{Mg} + \text{O}_2$	\$	1.0e-10
04)	$\text{Mg} + \text{O}_3 = \text{MgO} + \text{O}_2$	\$	2.0e-10
05)	$\text{MgO} + \text{CO}_2 + \text{N}_2 = \text{MgCO}_3 + \text{N}_2$	\$	2.0e-27
06)	$\text{MgCO}_3 + \text{O} = \text{MgO}_2 + \text{CO}_2$	\$	1.0e-13
07)	$\text{Mg} = \text{Mg}^+ + \text{e}^-$	\$	4.0e-07
08)	$\text{Mg} + \text{O}_2^+ = \text{Mg}^+ + \text{O}_2$	\$	1.0e-10
09)	$\text{Mg} + \text{NO}^+ = \text{Mg}^+ + \text{NO}$	\$	1.0e-10
10)	$\text{Mg} + \text{O}^+ = \text{Mg}^+ + \text{O}$	\$	1.0e-10
11)	$\text{Mg}^+ + \text{e}^- = \text{Mg}$	\$	1.0e-12
12)	$\text{Mg}^+ + \text{N}_2 + \text{O}_2 = \text{MgO}_2^+ + \text{N}_2$	\$	2.5e-30
13)	$\text{MgO}_2^+ + \text{e}^- = \text{Mg} + \text{O}_2$	\$	3.0e-07
14)	$\text{Mg}^+ + \text{O}_3 = \text{MgO}^+ + \text{O}_2$	\$	2.3e-10
15)	$\text{MgO}^+ + \text{e}^- = \text{Mg} + \text{O}$	\$	1.0e-07

# MAGNESIUM ION MODEL 2C

01)	$\text{Mg} + \text{O}_2 + \text{N}_2 = \text{MgO}_2 + \text{N}_2$	\$	4.3e-36
02)	$\text{MgO}_2 + \text{O} = \text{MgO} + \text{O}_2$	\$	2.0e-14
03)	$\text{MgO} + \text{O} = \text{Mg} + \text{O}_2$	\$	1.0e-10
04)	$\text{Mg} + \text{O}_3 = \text{MgO} + \text{O}_2$	\$	2.0e-10
05)	$\text{MgO} + \text{CO}_2 + \text{N}_2 = \text{MgCO}_3 + \text{N}_2$	\$	2.0e-27
06)	$\text{MgCO}_3 + \text{O} = \text{MgO}_2 + \text{CO}_2$	\$	1.0e-13
07)	$\text{Mg} = \text{Mg}^+ + \text{e}^-$	\$	4.0e-07
08)	$\text{Mg} + \text{O}_2^+ = \text{Mg}^+ + \text{O}_2$	\$	1.0e-10
09)	$\text{Mg} + \text{NO}^+ = \text{Mg}^+ + \text{NO}$	\$	1.0e-10
10)	$\text{Mg} + \text{O}^+ = \text{Mg}^+ + \text{O}$	\$	1.0e-10
11)	$\text{Mg}^+ + \text{e}^- = \text{Mg}$	\$	1.0e-12
12)	$\text{Mg}^+ + \text{N}_2 + \text{O}_2 = \text{MgO}_2^+ + \text{N}_2$	\$	2.5e-30
13)	$\text{MgO}_2^+ + \text{e}^- = \text{Mg} + \text{O}_2$	\$	3.0e-07
14)	$\text{Mg}^+ + \text{O}_3 = \text{MgO}^+ + \text{O}_2$	\$	2.3e-10
15)	$\text{MgO}^+ + \text{e}^- = \text{Mg} + \text{O}$	\$	1.0e-07
16)	$\text{MgO}_2^+ + \text{O} = \text{MgO}^+ + \text{O}_2$	\$	1.0e-10
17)	$\text{MgO}^+ + \text{O} = \text{Mg}^+ + \text{O}_2$	\$	1.0e-10

# MAGNESIUM ION MODEL 2D

01)	$\text{Mg} + \text{O}_2 + \text{N}_2 = \text{MgO}_2 + \text{N}_2$	\$	4.3e-36
02)	$\text{MgO}_2 + \text{O} = \text{MgO} + \text{O}_2$	\$	2.0e-14
03)	$\text{MgO} + \text{O} = \text{Mg} + \text{O}_2$	\$	1.0e-10
04)	$\text{Mg} + \text{O}_3 = \text{MgO} + \text{O}_2$	\$	2.0e-10
05)	$\text{MgO} + \text{CO}_2 + \text{N}_2 = \text{MgCO}_3 + \text{N}_2$	\$	2.0e-27
06)	$\text{MgCO}_3 + \text{O} = \text{MgO}_2 + \text{CO}_2$	\$	1.0e-13
07)	$\text{Mg} = \text{Mg}^+ + \text{e}^-$	\$	4.0e-07
08)	$\text{Mg} + \text{O}_2^+ = \text{Mg}^+ + \text{O}_2$	\$	1.0e-10
09)	$\text{Mg} + \text{NO}^+ = \text{Mg}^+ + \text{NO}$	\$	1.0e-9
10)	$\text{Mg} + \text{O}^+ = \text{Mg}^+ + \text{O}$	\$	1.0e-9
11)	$\text{Mg}^+ + \text{e}^- = \text{Mg}$	\$	1.0e-12
12)	$\text{Mg}^+ + \text{N}_2 + \text{O}_2 = \text{MgO}_2^+ + \text{N}_2$	\$	2.5e-30
13)	$\text{MgO}_2^+ + \text{e}^- = \text{Mg} + \text{O}_2$	\$	3.0e-07
14)	$\text{Mg}^+ + \text{O}_3 = \text{MgO}^+ + \text{O}_2$	\$	2.3e-10
15)	$\text{MgO}^+ + \text{e}^- = \text{Mg} + \text{O}$	\$	1.0e-07
16)	$\text{MgO}^+ + \text{O} = \text{Mg}^+ + \text{O}_2$	\$	1.0e-10